Characterization and Permeation Studies on Oriented Single-Crystal Ferrierite Membranes

Thesis by

John Edwin Lewis, Jr.

In Partial Fulfillment of the Requirements

for the Degree of

Doctor of Philosophy

California Institute of Technology

Pasadena, California

1996

(Submitted May 14, 1996)

To Dina

Acknowledgments

As a scientist and a person, I feel very strongly that we are a product of our interactions with people as much as our formal education. Thus, it is very important for me to recognize all the individuals who have made this endeavor possible.

I am deeply indebted to my advisor Prof. Mark E. Davis for his guidance, support and unfailing confidence in my ability to succeed. During the difficult and frustrating moments of my graduate school career, Mark was a constant source of inspiration and encouragement. I would also like to thank Prof. George R. Gavalas for his interest in my project and enlightening discussions.

I want to thank all the members of the Davis research group, both past and present, for providing a stimulating and enjoyable work environment. In particular, there are certain people who require special acknowledgment. My classmates Chris Dartt and John Nagel are excellent friends and together we have overcome many challenges. H.X. Li and C.Y. Chen were instrumental in teaching me the fundamentals of zeolite synthesis and characterization. Clemens Freyhardt is responsible for teaching me most of what I know about crystallography. Although a recent acquaintance, his contributions have been immense and his high standards provided me with a new level of appreciation for consistently doing quality work.

The contents of this thesis are not only the result of my five years at Caltech, but also a lifetime of support and love from my family and friends. Most importantly, I wish to thank Mom, Dad and Jill for all their nurturing love and support. Early on, they instilled in me a solid work ethic and taught me the value of education. All of my achievements are a testimony to their love and sacrifices.

The people most responsible for who I am are the Magnificent Seven. Stephen, Shaun, Bobby, Bernard, Brent and Daryush have made the difficult years at Caltech

bearable. Although the clan has been scattered to all corners of the earth, a word of encouragement or amusing story has always been only a phone call away.

And finally, I wish to acknowledge the great love of my life, Dina. She is the one who provided the motivation and strength to bring this project to fruition. Without her immense understanding and encouragement, this thesis would not be possible.

Barter

by Sara Teasdale (1884-1933)

Life has loveliness to sell,
All beatiful and splendid things,
Blue waves whitened on a cliff,
Soaring fire that sways and sings,
And children's faces looking up,
Holding wonder like a cup.

Life has loveliness to sell,
Music like a curve of gold,
Scent of pine trees in the rain,
Eyes that love you, arms that hold,
And for your spirit's still delight,
Holy thoughts that star the night.

Spend all you have for loveliness,
Buy it and never count the cost;
For one white singing hour of peace
Count many a year of strife well lost,
And for a breath of ecstacy
Give all you have been, or could be.

Abstract

Single-crystals (up to 650 x 550 x 20 μm) of highly silicious ferrierite (Si-FER, **1**), suitable for single-crystal X-ray investigations, are synthesized under organothermal conditions. The structures of the as-synthesized (**1a**) and the calcined (**1b**) Si-FER are determined at room temperature. Both structures are refined in the orthorhombic space group Pnnm (No.58, standard setting) with a = 743.0(1), b = 1409.2(2), c = 1882.0(2) pm, V = 1970.5(4)·10^6 pm^3, Z = 1, R = 0.041 (**1a**) and a = 741.8(1), b = 1407.0(2), c = 1871.3(2) pm, V = 1953.1(5)·10^6 pm^3, Z = 1, R = 0.037 (**1b**). The structure solution when combined with chemical analysis and ^1H and ^{13}C MAS NMR, give a unit cell content of $[Si_{36}O_{72}]\{py_{(4-x)}\ ap_x\}$ (x = 0 - 1, py = pyridine, ap = 1-amino-n-propane) and $[Si_{36}O_{72}]$ for **1a** and **1b**, respectively. The structure of **1a** shows only weak host-guest interactions between the $\{^3_\infty\}[SiO_{4/2}]$ framework and the occluded, orientationally disordered pyridine molecules by means of relatively long organic-to-framework distances, $d(C_{py}\cdots O) \geq 354(2)$ pm. ^{29}Si MAS NMR spectra from the organic-containing Si-FER **1a** and the organic-free form **1b** are in good agreement with the crystallographic results in that they conform to the well-known linear relationship between the cosine expression of the T-O-T angles and the chemical shift of the respective tetrahedral sites (T-sites). A new modification of this relationship is presented here and offers an improved linear correlation between the X-ray and NMR data for **1a** and **1b**, as well as for other high-silica microporous materials. Application of this new correlation to denser SiO_2 compounds is discussed.

Selected individual crystals of the calcined Si-FER are mounted in a membrane configuration so that only the 10-membered ring channels (5.4 Å x 5.4 Å x 4.2 Å) or the 8-membered ring channels (4.6 Å x 3.7 Å x 3.0 Å) are accessible for gas molecule permeation. The first examples of transport exclusively through 8- or 10-membered ring

channel systems are reported and obtained through crystal orientation in the membrane. A series of adsorption experiments are conducted in order to assist the selection of suitable probe molecules and evaluate the role of adsorption in the permeation process for the single-crystal membranes. Methane, n-butane, isobutane and nitrogen probe molecules are used to study intracrystalline sorption and transport effects for different crystal orientations, pressures and temperatures. Both pure gas selectivities and mixed gas separation factors are reported. A mixed gas separation factor of n-butane/isobutane = 116 for the 10-membered ring orientation of the crystal at 383 K and a transmembrane pressure difference of 1.01 x 10^5 Pa is found using this technique. In addition, molecular sieving is observed for the 8-membered ring orientation of the crystal since methane, but not butane, transport is observed for this crystal orientation.

Table of Contents

List of Tables

Chapter 2

Appendix

List of Figures

Chapter 2

Chapter 1

Introduction

1.1 Motivation

Gas phase separations comprise a large and critical component of the chemical process industry. Typical examples of required separations include removal of contaminants from raw materials (removal of CO_2, N_2 and H_2S from natural gas), recovery and purification of primary products (separation of air into its primary components of oxygen and nitrogen) and elimination of contaminants from effluent streams (removal of volatile organic compounds from exhaust streams). In addition to purifying products and removing wastes, gas separation processes must be cost effective. Over the years, several different separation processes have developed to meet the needs of the chemical process industry. These processes can generally be grouped into the following categories: distillation, extraction, adsorption and membranes. Each of these processes has advantages and disadvantages based upon its intrinsic separation mechanism, economics and the constraints imposed by the desired application. However, membranes occupy a special niche in the realm of separations in that they combine thermodynamically based partitioning with kinetically based mobility discrimination in an integrated separation unit. Thus, the importance of gas phase separations and the unique properties of membranes establish the motivation to study membrane-based separations.

1.2 Definitions and Background

The flux of a permeating gas, J, is defined as the amount of permeate passing through a surface area, S, of a given membrane in a length of time, t. The parameters that characterize

the quality of a membrane are permeance and selectivity. Permeance, K, is the flux of the permeating gas, J, normalized by the driving force, ΔP, across the membrane.

$$K = J/(\Delta P)$$

When the permeance is multiplied by the thickness, L, of the separating layer in the membrane, a quantity known as permeability, A, is defined.

$$A = K \cdot L$$

Thus, membranes with a thin separating layer are desired to maximize throughput and productivity. Selectivity is defined as the permeance ratio of two gases and describes the ability of the membrane to separate a feed stream into its corresponding components. The successful membrane must also possess thermal and mechanical stability in addition to chemical inertness to allow for operation in chemically corrosive environments.

One developing area of gas phase separation that has recently drawn a great deal of interest is inorganic membranes. Inorganic membranes have the potential for high separation selectivity and the capacity to operate at temperatures and pressures well in excess of the limitations of the polymer based membranes currently used commercially[1]. Some previous work on inorganic membranes[2] employed mesoporous materials, primarily, Vycor glass with pore sizes ranging from 30 Å to 70 Å. However, in this pore size range diffusion is limited to the Knudsen regime which is insufficient for most applications of interest. In contrast, metal membranes, dense amorphous oxide membranes, carbon membranes, and zeolite membranes have dense or microporous structures and can give higher separation factors. Nonporous palladium membranes have good permeability and selectivity to hydrogen and have been used in some small scale specialized applications[3]. The application of palladium membranes to large scale processes is limited by the cost of the metal, and by material property problems such as embrittlement and loss of adhesion to the substrate. Nonporous amorphous oxides such as SiO_2 and B_2O_3 are also highly selective to hydrogen permeation. It has been shown that a H_2:N_2 permeation ratio of

2000-5000 at 450-600°C for SiO_2 films deposited within the walls of porous substrate tubes can be achieved[4]. These dense amorphous oxide membranes are suitable for hydrogen separation from other gases but are unsuitable for other separations (e.g. O_2 - N_2) because of the negligible permeation rates of these molecules through the oxide. Amorphous oxide membranes are also unsuitable for ambient temperatures, again because of very low permeation rates. Recent advances in the fabrication of high-quality perovskite-type oxide membranes demonstrate that the mixed (electronic/ionic) conductivity of these materials is promising for oxygen-permeating membranes that can operate without an externally applied electrical driving force[5].

Zeolites are crystalline, three dimensional, inorganic framework structures generally composed of tetrahedral atoms which connect together via bridging oxygens to form channels and cages. These materials are classified as molecular sieves due to their ability to separate molecules based on size and shape. Such intricate separations are possible due to the regular and precise channel systems formed by the frameworks of these crystals. In zeolites, the tetrahedral atom sites are occupied by aluminum and silicon atoms. An important subset of zeolites are zeosils, where the tetrahedral atom sites are occupied exclusively by silicon atoms. The Si/Al ratio in the framework of the zeolite is an important factor in determining the types of molecules that will adsorb in the channels of the zeolite. A high Si/Al ratio creates a hydrophobic environment that preferentially adsorbs non-polar molecules such as hydrocarbons. A low Si/Al ratio creates a hydrophilic environment that strongly adsorbs polar molecules such as water. Such considerations are important when designing the membrane process.

Since zeolites are commonly used in granular form for gas separations via pressure and temperature swing adsorption, there is a great economic incentive to convert this transient operation to a steady-state process. Thus, it is necessary to prepare the zeolite as a continuous film supported on a porous support element. Several research groups have been working on the synthesis of zeolite membranes. Zeolite layers supported on porous tubes

have been synthesized by Suzuki[6]. Layers of different zeolite phases were prepared by coating a porous Vycor tube with a gel precursor and subsequently subjecting it to hydrothermal treatment. Membranes prepared in this manner crack upon heating, thus destroying their gas separation abilities. Composite membranes consisting of zeolite crystallites imbedded in a nonporous silica matrix have also been studied[7]. The permeability of this coating is controlled by the degree of connectivity between the crystals to form continuous paths for diffusion. Similar membranes were prepared by imbedding the zeolite crystallites in a silicon rubber matrix[8]. In this composite membrane, the zeolite crystallites need not be connected because the rubber itself has some permeability to all molecules. Separation selectivity is enhanced by virtue of the different solubility and diffusivity of different molecules in the zeolite. Because of the methods of preparation, it is not clear whether these composite membranes can show reproducible results. In another method, porous Vycor tubes were dipped in suitable solutions of silica and alumina and subsequently subjected to hydrothermal treatment[9]. Membranes made by this method showed high separation factors (larger than 200) between water and ethanol at 80°C. The selective layer was claimed to be zeolitic but no evidence to that effect was provided. Amorphous hydrous aluminosilicate gel may provide high permeation of water versus ethanol because of its strongly hydrophilic character. Continuous polycrystalline films of ZSM-5 grown on porous ceramic (clay) supports have also been reported[10]. However, the permeation rates for these membranes were very low. These low permeation rates were attributed to the lack of zeolite channel connectivity between the crystallites and thickness of the polycrystalline layer. These initial attempts, starting almost a decade ago, to produce a zeolitic membrane with satisfactory permeation and separation ratios illustrate some of the trials and challenges which needed to be overcome.

During the past few years, significant improvements have been achieved in the fabrication of zeolitic membranes[11]. One of the most promising ZSM-5 membranes

constructed to date is by Yan[12]. In this work, ZSM-5 was grown on porous α-Al_2O_3 disks by in-situ hydrothermal synthesis. Pure gas permeation mesurements of the most successful preparation yielded hydrogen:isobutane and n-butane:isobutane ratios of 151 and 18 at room temperature and 54 and 31 at 185°C, respectively. Ferrierite membranes have been synthesized by Matsukata et al.[13] and zeolite A membranes have been reported by Masuda et al.[14] which demonstrate the ability to form zeolite membranes with other phases than the traditionally studied ZSM-5 membranes.

Zeolite membranes stand out among other inorganic membranes because of high selectivity, ability to function over a wide temperature range, and imperviousness to traditionally corrosive environments. The wide choice of zeolite structures and the ability to modulate the pore opening by exchanging with different cations makes the zeolite membranes potentially applicable to a wide variety of gas mixtures. In addition to bulk separations, zeolite membranes can be advantageously integrated into catalytic reactor systems to improve yield or selectivity[15].

Despite these great advances, molecular transport in zeolites is still a poorly understood area[16]. In every application of zeolites, the molecules and ions all enter and exit the molecular sieve crystal through windows circumscribed by the tetrahedral atoms of the framework and then diffuse along the channels in the crystal. Therefore the interpretation and correlation of mass transport, i.e. diffusion, in molecular sieves is a topic of great interest in a wide variety of chemical processes. However, obtaining accurate data for this transport phenomena has proven to be a difficult task. A variety of different methods have been developed for the measurement of intracrystalline diffusion. These approaches can be divided into microscopic methods such as pulsed field gradient NMR techniques[17] and macroscopic methods such as gravimetric uptake rate methods[18], embedded crystal method[19] and single-crystal membranes[20]. This wide variety of techniques for studying the

transport of molecules through the channels of zeolites has resulted in diffusivity data reported in the literature differing by several orders of magnitude. Re-examination of the experimental conditions of the earlier uptake rate methods has led to the conclusion that the impact of heat effects and entrance effects at the surface of zeolite crystals is much more significant than originally assumed[21]. These discrepancies stimulated the development of more sophisticated macroscopic methods aimed at rectifying the differences between these different methods by minimizing extraneous effects[22]. The single-crystal membrane technique is one such method.

1.3 Objectives and Outline

The purpose of this thesis is to experimentally address the issue of defining maximum obtainable separation factors for zeolitic membranes. As outlined in the introduction, the preparation techniques, and correspondingly the achievable separation selectivities, have dramatically improved over the past decade. However, to date no one has been able to define upper bounds for zeolite membrane separation factors. This issue will be approached in this work via permeation studies on large, oriented single-crystals of ferrierite. Provided the transport mechanisms remain the same for polycrystalline and single-crystal membranes, the intrinsic single-crystal selectivity sets an upper bound for the selectivity of polycrystalline membranes and shows to what extent polycrystalline membrane selectivities can be improved by eliminating nonzeolitic pores. Due to the convenient morphology and relative channel orientation of the ferrierite crystals, membranes can be constructed so only the 10-membered ring channels or the 8-membered ring channels are accessible for gas molecule permeation. This will make possible for the first time the study of transport

exclusively through well defined 8- and 10-membered ring channel systems in a molecular sieve.

This study is organized and results reported in the following manner. Chapter 2 details the synthesis and extensive characterization of the pure-silica ferrerite crystals. The single-crystal structure solution for the calcined ferrierite defines the 8- and 10-membered ring channel systems through which the probe molecule permeation will occur. Chapter 3 discusses the construction of the single-crystal membranes and permeation studies using single gas and mixed gas hydrocarbons. A series of physical adsorption experiments are also conducted to study the influence of adsorption on the permeation process in single crystal membranes. Chapter 4 summarizes the findings of this dissertation and proposes the extension of the oriented single-crystal ferrierite membrane technique to probe molecules other than hydrocarbons. The appendix contains listings of anisotropic displacement parameters for all refined atoms and structure factor amplitudes for the as-synthesized and calcined ferrierite resulting from the single-crystal structure solution.

Literature Cited

[1] Matson, S. L.; Lopez, J.; Quinn, J. A. *Chem. Eng. Sci.* **1983**, *38*, 503.

[2] Hsieh, H.P. *Inorganic Membranes*; AIChE Symposium Series, **1988**; Vol. 84, pp 1-18.

[3] Shekekhin, A. B.; Grosgogeat, E. J.; Hwang S. T. *J. Membrane Sci.* **1991**,*66*, 129.

[4] Gavalas, G. R.; Megiris, C.; Nam S. W. *Chem. Eng. Sci.* **1989**, *44*, 1829.

[5] Balachandran, U.; Dusek, J. T.; Mieville, R. L.; Poeppeel, R. B.; Kleefisch, M. S.; Pei, S.; Kobylinski, T. P.; Udovich, C. A.; Bose, A. C. *Appl. Catal. A.* **1995**, *133*, 19.

[6] Suzuki, H. U.S. Patent 4 699 892, 1987.

[7] Bein, T.; Brown, K.; Brinker, C. J. In *Zeolites: Facts, Figures, Future*; Jacobs, P. A.; van Santen, R. A., Eds.; Elsevier: Amsterdam, 1989; p. 887-896.

[8] te Hennepe, H. J. C.; Bargeman, D.; Mulder, M.H.V.; Smolders, C. A. *J. Membr. Sci.* **1987**, *35*, 39.

[9] Ishikawa, A.; Chiang, T. H.; Toda, F. *J. Chem. Soc., Chem. Commun.* **1989**, *1989*, 764.

[10] Geus, E. R.; den Exter, M. J.; van Bekkum, H. *J. Chem. Soc. Faraday Trans.* **1992**, *88*, 3101.

[11] Jansen, K. C.; Coker, E. N. *Current Opinions in Solid State & Materials Science*, **1996**, *1*, 65.

[12] Yan, Y.; Davis, M. E.; Gavalas, G. R. *Ind. Eng. Res.*, **1995**, *34*, 1652.

[13] Matsukata, M.; Nishiyama, N.; Ueyama, K. In *Studies in Surface Science and Catalysis*; J. Weitkamp, H. G. Karge, H. Pfeifer and W. Hölderich, Eds.; Elsevier: Amsterdam, 1995; pp. 1183-1190.

[14] Masuda, T.; Hara, H.; Kuono, M.; Kinoshita, H.; Hashimoto, K. *Microporous Materials* **1995**, *3*, 565.

[15] Amor, J. N. *Appl. Catal.* **1989**, *49*, 1.

[16] Chen, N. Y.; Degnan, Jr., T. F.; Smith, C. M. *Molecular Transport and Reaction in Zeolites*, VCH: New York, 1994, p 7.

[17] Kärger, J.; Heink, W. *Exp. Tech. Phys.* **1971**, *19*, 453.

[18] Caro, J.; Noack, M.; Richter-Mendau, J.; Marlow, F.; Petersohn, D.; Griepenstrog, M.; Kornatowski, J. *J. Phys. Chem.* **1993**, *97*, 13685.

[19] Kölsch, P.; Venzke, D.; Noack, M.; Toussaint, P.; Caro, J. *J. Chem. Soc., Chem. Commun.* **1994**, *1994*, 2491.

[20] Paravar, A. R.; Hayhurst, D. T. In *Proceedings of the 6th International Zeolite Conference*; Olson, D.; Bisio, A., Eds.; Butterworths: New York, 1984, p.217.

[21] Bülow, M.; Struve, P. *J. Chem. Soc. Faraday Trans. I* **1984**, *80*, 813.

[22] Ruthven, D. M. In *Zeolites: A Refined Tool for Designing Catalytic Sites*, Bonnevoit, L.; Kaliaguine, S., Eds.; Elsevier: Amsterdam, 1995, p. 223-234.

Chapter 2

Location of Pyridine Guest Molecules in an Electroneutral $\{^3_\infty\}[SiO_{4/2}]$ Host Framework: Single-Crystal Structures of the As-Synthesized and Calcined Forms of High-Silica Ferrierite

---

Reprinted with permission from

J. Phys. Chem. **1996**, *100*, 5039-5049

Location of Pyridine Guest Molecules in an Electroneutral $\{^3_\infty\}[SiO_{4/2}]$ Host Framework: Single-Crystal Structures of the As-Synthesized and Calcined Forms of High-Silica Ferrierite

John E. Lewis Jr., Clemens C. Freyhardt and Mark E. Davis

Chemical Engineering, California Institute of Technology

Pasadena, CA 91125

Abstract

Single-crystals (up to 650 x 550 x 20 μm) of highly silicious ferrierite (Si-FER, **1**), suitable for single-crystal X-ray investigations, are synthesized under organothermal conditions. The structures of the as-synthesized (**1a**) and the calcined (**1b**) Si-FER are determined at room temperature. Both structures are refined in the orthorhombic space group Pnnm (No.58, standard setting) with a = 743.0(1), b = 1409.2(2), c = 1882.0(2) pm, V = 1970.5(4)·10^6 pm^3, Z = 1, R = 0.041 (**1a**) and a = 741.8(1), b = 1407.0(2), c = 1871.3(2) pm, V = 1953.1(5)·10^6 pm^3, Z = 1, R = 0.037 (**1b**). The structure solution when combined with chemical analysis and ^1H and ^{13}C MAS NMR, give a unit cell content of $[Si_{36}O_{72}]\{py_{(4-x)}\ ap_x\}$ (x = 0 - 1, py = pyridine, ap = 1-amino-n-propane) and $[Si_{36}O_{72}]$ for **1a** and **1b**, respectively. The structure of **1a** shows only weak host-guest interactions between the $\{^3_\infty\}[SiO_{4/2}]$ framework and the occluded, orientationally disordered pyridine molecules by means of relatively long organic-to-framework distances, $d(C_{py}\cdots O) \geq 354(2)$ pm. ^{29}Si MAS NMR spectra from the organic-containing Si-FER **1a**

and the organic-free form **1b** are in good agreement with the crystallographic results in that they conform to the well-known linear relationship between the cosine expression of the T-O-T angles and the chemical shift of the respective tetrahedral sites (T-sites). A new modification of this relationship is presented here and offers an improved linear correlation between the X-ray and NMR data for **1a** and **1b**, as well as for other high-silica microporous materials. Application of this new correlation to denser SiO_2 compounds is discussed.

2.1 Introduction

Highly-silicious microporous materials (tectosils) in general and high-silica zeolites (zeosils) in particular, have attracted attention in the past few years due to their unique catalytic and physicochemical properties[1]. Since these properties are closely related to the structures of the respective materials, it is of great interest to obtain highly accurate information about their specific structural features. Additionally, the use of organic or organometallic molecules as so-called structure-directing agents in the synthesis of microporous solids clearly illustrates the importance of understanding the interactions between the inorganic host framework and the organic guest species in the final products[2-5]. One of the most straight forward approaches enabling the elucidation of more general conclusions about the influences of these host-guest interactions is a direct comparison of precisely determined structures for the organic-containing and the organic-free form of the same zeotype material. In the present work, we report the single-crystal X-ray structures of as-synthesized and calcined high-silica ferrierite (Si-FER, **1a**, and Si-FER, **1b**, respectively) and compare the crystallographically obtained results with the data extracted from ^{29}Si MAS NMR.

Ferrierite (FER)[6] is known to be a natural as well as a synthetic zeolite with a framework structure of corner-sharing tetrahedral $TO_{4/2}$ units (T=Si^{IV}, Al^{III}) that give a fully condensed 3-dimensional framework that contains a system of intersecting channels that are circumscribed by 8 T-atoms and 10 T-atoms[7,8]. The ferrierite structure contains 36 T-atoms per unit cell giving a chemical formula of $[Al_{(5+y)}Si_{(31-y)}O_{72}]^{(5+y)-}$ for the framework; the natural material has a composition range of y = 0 - 3.5 and there are a variety of M^{+} and M^{2+} cations as extra-framework entities[9]. The structures of ZSM-35 and NU-23 are reported to be isotypic with the ferrierite structure and hence have the FER framework topology[6,10]. For these compounds, the formal negative charge of the $\{^3_\infty\}[TO_{4/2}]$ framework caused by the incorporation of trivalent Al-atoms at T-atom positions is charge-balanced by occluded alkaline and alkaline earth cations like Na^{+}, K^{+}, Mg^{2+} or Ca^{2+}. The expression $\{^3_\infty\}[TO_{4/2}]$ denotes a three-dimensional, infinite framework with 4-fold coordinated T-atoms that share each oxygen with an adjacent T-atom[11]. There exist numerous investigations concerning both the mineral as well as the synthetic Al-containing form of ferrierite, including single crystal structures that ascribe the pore-filling species mainly to be aqua complexes of the above mentioned cations[6,9,12-15]. Moreover, one synthetic approach was reported for the isomorphous substitution of Al^{3+} at the T-atom sites in the FER framework by an other trivalent element, namely, Ga^{3+} [16]. Typically, these ferrierite syntheses were carried out under normal hydrothermal conditions in the presence of strong inorganic bases, like NaOH or $Ca(OH)_2$, i.e., OH^{-} as a mineralizer for silica. The structure of an aluminum-free ferrierite produced from a hydrothermal synthesis using a boron containing starting gel has been reported[17]. No boron was found in the zeosil framework, but was reported to reside as a boric acid - ethylene diamine complex within the micropores. More recently, an organothermal

synthesis of the high-silica form of ferrierite (Si-FER, **1**) with an electroneutral $\{^3_\infty\}[SiO_{4/2}]$ framework has been developed that uses pyridine as solvent and HF, i.e., fluoride as the mineralizing agent[18]. Since this method yields a highly crystalline material that consists of large crystals with dimensions up to several 100 μm, a more detailed structure investigation than was recently reported[19,20] seemed now to be possible. Such a study should lead to the determination and location of entrapped guest species in the ferrierite host framework, and thus provide a better understanding of the role of these species as structure-directing agents in the synthesis of FER.

Until now, there has only been one published report on the structure of the organic free, high-silica ferrierite, Si-FER **1b**, that was from a Rietveld refinement of powder neutron diffraction data[20]. For the as-synthesized, organic-containing Si-FER **1a**, space group, cell parameters and unit cell content derived from single-crystal X-ray investigations have been reported, but neither atom positions or detailed description of the structure were given[18,19].

2.2 Experimental

Synthesis. The as-synthesized Si-FER **1a** was prepared under organothermal conditions in sealed Teflon-lined stainless steel autoclaves (Parr, 23 ml) according to the method developed by Kuperman et al.[18]. A mixture of fumed-silica (Cab-O-Sil M-5, Cabot Corp., 99.8%), HF/pyridine (Aldrich, ~70wt% HF), 1-amino-n-propane (ap) (Aldrich, 98%), distilled water and pyridine (py) (Aldrich, 99%) in a molar ratio of SiO_2 : HF/py : ap : H_2O : py = 1.5 : 2 : 4 : 8 : 16 was allowed to react in autoclaves at 448 K for 1-9 days under autogenous pressure and static conditions within a constant-temperature (± 2 K) convection oven. In a typical preparation, 12.7 g (0.16 mol) pyridine and 2.37 g (0.04

mol) 1-amino-n-propane were combined in a 40 ml polyethylene (PE) bottle. Next, 0.57 g (0.02 mol) HF/pyridine were added dropwise using a 10 ml PE syringe under continuous stirring at room temperature to give a white slurry. Addition of 0.91g (0.015 mol) SiO_2 resulted in a highly viscous, white suspension, that became clear immediately upon adding 1.45 g (0.08 mol) H_2O to give 18 g of a clear colorless solution. After stirring for 20 min in the closed PE bottle, the mixture was placed in a Teflon liner (exp. determined volume 21 ± 1 ml) with a filling of 80-90 vol%. At the end of a given reaction time, the formed solid was separated from the mother liquor by filtration, subsequently washed with water, rinsed with acetone and dried in air at room temperature. A reaction time of 8 d at 448 K led to a yield of 0.92 - 0.98 g (90 - 95% based on silica) of pure and highly crystalline compound **1a** (by powder X-ray analysis) that was uniformly-sized, plate-like crystals of size up to 650 x 550 x 20 μm. The organic-free Si-FER **1b** was obtained by careful calcination of the as-synthesized material **1a** under controlled conditions to avoid damage of the single-crystals. The calcination process was carried out in a temperature-controlled tube furnace equipped with a valve-regulated T-shaped gas inlet connected to air and N_2. The following heating program with the given atmosphere was used in the present work, leaving clear, colorless crystals of **1b** without any obvious cracking observable under an optical microscope: heat from 298 K to 973 K within 9 h (N_2), hold isothermal at 973 K for 10 h (N_2); heat from 973 K to 1173 K within 4 h (air), hold isothermal at 1173 K for 24 h (air).

Elemental analysis. C,H,N analysis and Si, Al, B and F analyses were all performed by Galbraith Laboratories, Inc. (Knoxville, TN). Trace Al and B in the samples are due to impurities from the chemicals used in the synthesis. Anal. found (theor. calc. x = 0.4, as inferred from X-ray structure determination (Table 1), and x = 1 as upper bound for ap content) for $[Si_{36}O_{72}]\{py_{(4-x)}\ ap_x\}$, **1a**: C 8.51 (9.33, 8.79), H 0.95 (0.89, 0.99), N 2.22 (2.27; 2.28), Si 38.0 (40.8, 41.0), Al < 0.05 (0, 0), B < 0.03 (0, 0), F < 0.05 (0, 0) %;

anal. found (theor. calc.) for $[Si_{36}O_{72}]$, **1b**: Si 44.2 (46.6), Al < 0.05 (0), B < 0.03 (0), F < 0.05 (0) %.

Thermogravimetric analysis (TGA). Standard TGA measurements were carried out on a Du Pont 951 thermogravimetric analyzer in air using a constant heating rate of 5 K/min from 298 K to 1173 K and subsequent isothermal treatment at 1173 K for 5 h. The resulting samples appeared as white powders with no visible impurities of remaining organic decomposition products. Exp. found (theor. calc. x = 0.4, x = 1) weight loss for **1a**: 11.8 (12.5, 12.1) wt%; anal. found (theor. calc.) for **1b**: 0.4 (0.0) wt%.

N_2 adsorption. Nitrogen adsorption isotherms were collected on a Omnisorp 100 analyzer at 77 K with a flow rate (F) to sample weight (W) ratio of F / W = 0.67 g·min·cm^{-3} at STP (standard temperature and pressure)[21].

Scanning electron microscopy (SEM). SEM images were recorded on a Camscan 2-LV scanning electron microscope using an acceleration voltage of 15 kV.

Powder X-ray diffraction analysis. Room temperature powder XRD patterns were recorded on a Scintag XDS 2000 diffractometer (graphite monochromator, $CuK_{<\alpha>}$ radiation, λ = 154.184 pm) with a Bragg-Brentano geometry. Approximate, average crystallinity of the recovered solids was determined by comparing the intensity of the (015) reflection in the respective powder X-ray diffractograms (PXRD) with the same reflection of a highly-crystalline ferrierite sample.

MAS NMR. All NMR spectra were collected at room temperature on a Bruker AM 300 spectrometer using 4 mm and 7 mm ZrO_2 rotors as sample holders. The magic angle spinning (MAS) technique was used for ^{29}Si (59.63 MHz), ^{13}C (75.47 MHz) and ^{1}H (300.13 MHz) NMR spectra; for ^{29}Si and ^{13}C spectra cross-polarization (CP) was applied also. The ^{29}Si (without CP) and ^{1}H spectra were recorded with the respective rotor spinning speeds (3.5, 10 kHz), pulse lengths (4, 6 μs) and delay times (20, 5 s) between

single pulses. For the ^{29}Si and ^{13}C CP/MAS NMR experiments (spinning speeds 3 and 5 kHz), pulse lengths and delay times for protons were used with contact times of 10 and 5 ms, respectively. Reference materials for chemical shift determination were $Si(SiMe_3)_4$ (^{29}Si) and adamantane (^{13}C, ^1H), and all chemical shifts are reported in [ppm] relative to the external standard $SiMe_4$ (TMS).

Single-crystal X-ray structure analysis. Crystal quality and relation of the crystallographically determined cell parameters to the overall morphology of the obtained crystals were checked on a Supper Weissenberg camera ($CuK_{<\alpha>}$ radiation, λ = 154.184 pm) using an optical two-circle goniometer for the pre-alignment. Suitable crystals of **1a** and **1b** were selected using a polarizing microscope and fixed with 5 minute hardening epoxy on the tip of a glass fiber. The fiber was mounted on a Rigaku AFC5-R four-circle diffractometer, that was equipped with a rotating X-ray Cu anode (Power = 9 kW, graphite monochromator, $\lambda(CuK_{<\alpha>})$ = 154.184 pm). Screening of several crystals showed that the large-sized crystals with the maximum dimensions mentioned above tended to have more twinned parts or stacking faults than smaller crystals with dimensions around 250 x 200 x 10 μm. Thus, crystals in the latter size range were selected for data collection. The cell parameters were refined from the angular positions of 25 reflections in the range of 22° < θ < 36°. Intensities of the collected data sets were measured by a variable ω/2θ-scan technique using an attenuator for very intense reflections (for details of crystallographic data and intensity measurements of **1a** and **1b**, see Table 1). Due to the strongly anisotropic crystal morphology, an empirical absorption correction was carried out on the basis of 360°-psi-scans for three reflections with c-values close to 90°. The structures were solved by direct methods using the SHELXS-86 program system[22]. Structure refinements based on F^2 (SHELXL-93)[23] included all unique reflections that were weighted according to the scheme $w = [\sigma^2(F_o^2) + (a \cdot P)^2]^{-1}$ with $P = 1/3\ [\max(F_o^2, 0) + 2\ F_c^2]$ (**1a**: a = 0.08,

1b: a = 0.065). Neutral atom scattering factors from the International Tables of Crystallography, Volume C were used[24]. All framework atoms of **1a** and **1b** and the pyridine molecules of **1a** were refined anisotropically, while the atom positions for the statistically underoccupied 1-amino-n-propane were fixed isotropically (U_{iso} = 0.10·10^4 pm^2). All atoms of the organic molecules were treated as carbon atoms and no hydrogen atoms were included in the final refinement cycles. For evaluating the guest-host distances d[(C)H···O], d[(C)H···Si] and angles ∠[C-H···O], the hydrogen atoms for the pyridine molecules were calculated at idealized positions around the respective carbon atoms without further refinement, using the typical aromatic C-H distance of 108 pm derived from averaged neutron data[25].

Structure calculations were performed on a Dell Dimension XPS/P60 personal computer (Pentium processor). Drawings were generated with the programs SCHAKAL (PC version)[26] and ORTEP (VMS version on a VAX3200 work station)[27].

2.3 Results and Discussion

Crystal growth and morphological aspects.

Investigation of the products obtained by the organothermal synthesis after heating for 1 to 9 d showed that after 24 h a few plate-like crystals of Si-FER **1a** had already formed with maximum dimensions of about 120 µm in length (l), 110 µm in width (w) and 10 µm thickness (t). Herein, l, w and t are defined as depicted in Figure 1d. After thermal treatment for 1 d, the low viscosity starting solution had transformed into a highly viscous gel, which, after drying, possessed an average crystallinity of about 5%. Within 6 d of heating, the crystal size increased from 120 x 110 x 10 µm to 580 x 480 x 20 µm, whereas

the average crystallinity of the solid in the same time increased up to ~ 95% (Figure 2). The formed crystals were now found to be on the bottom of the Teflon liner and the supernatant mother liquor had returned to a low viscosity, clear solution. It was also noted that the l : w ratio was almost independent of the crystal size and remained at a nearly constant value of 1.2 indicating a uniform growth rate parallel to the directions of the two long crystal edges, i.e., the crystallographic [010] and [100] directions (see below). Surprisingly, the morphology of the ferrierite crystals isolated from different batches, although prepared in the same way, varied (not within the same batch) from elongated octagon-shaped to almost rectangular plates (Figures 1a - c). In general, crystals of **1a** with a shape more similar to the plates shown in Figure 1a and 1b appeared in the products. This result differs remarkably from the previously described diamond-shaped morphology[18,19]. It was noted that the physical appearance, i.e., morphology, color, transparency and size of the crystals of as-synthesized Si-FER **1a** did not change after calcination to produce the organic-free Si-FER **1b**. Despite the differences in their plate shape, all ferrierite crystals obtained in the present work possess a mmm ($\equiv D_{2h}$) point group symmetry indicating an orthorhombic space group that belongs to the corresponding Laue class mmm. This symmetry assignment still holds upon closer inspection under the optical and the scanning electron microscope, which showed the crystal plates not to be perfectly flat, but to have an extremely flattened roof-shape on both sides of the plates (Figure 1d). Oscillation and zero-level Weissenberg photographs of optically aligned single-crystals with a well-defined morphology revealed, that the orientations of the above described dimensions l, w and t are parallel to the respective directions of the crystallographic b-, a- and c-axes. This indicates that the slowest growth rate for the ferrierite crystals occurs in the direction of the largest unit cell axis, i.e. the [001] direction, which is parallel to the smallest crystal dimension t. (Note: Here we use the standard setting of the space group Pnnm (No.58) with the order of increasing cell parameters being $a < b < c$. To compare the crystallographic directions

and atom positions with former descriptions of ferrierite structures, which mainly use c < b < a, the 3x3 transformation matrix (001)(0 $\bar{1}$0)(100) must be applied.)

X-ray Structure Determination

Transparent, colorless crystals of Si-FER **1a** and Si-FER **1b** with the morphology shown in Figure 1b and dimensions of 240 x 210 x 10 μm and 220 x 200 x 10 μm, respectively, were chosen for the single-crystal X-ray structure analysis. Details of crystallographic data, intensity measurements and structure refinements are summarized in Table 1 and described in the Experimental Section. Closer investigation of the systematic absences of the collected data sets revealed unambiguously the orthorhombic space group Pnnm (No.58) (see note above) for both structures at 298 K. No evidence for a higher symmetric, orthorhombic space group, e.g., Immm[17], or a monoclinic symmetry, e.g., $P2_1/n$, as reported for the natural, Al-containing ferrierite[13], was found. This result is in agreement with previously reported data[18,19]; however, in that work, the structure of the as-synthesized Si-FER is described to contain pyridine (py) and HF guest molecules as pore-filling species leading to a chemical formula $[Si_{36}O_{72}]\{py_2\ (HF)_8\}$ per unit cell. However, no proof for this chemical composition by other independent analytical methods was given. In contrast, the respective unit cell contents of $[Si_{36}O_{72}]\{py_{(4-x)}\ ap_x\}$ (x = 0 - 1; py = pyridine, NC_5H_5; ap = 1-amino-n-propane, $H_2N(C_3H_7)$) and $[Si_{36}O_{72}]$ for **1a** and **1b** obtained in the present work are confirmed by chemical as well as spectroscopic analyses (see below). Tables 2 and 3 contain the final atomic parameters for the structures of **1a** and **1b**. Important bond distances and angles of both structures are provided in Tables 4, 5 and 6.

Framework

The structure determinations of **1a** and **1b** led in both cases to the typical FER topology for the framework with 5 crystallographically non-equivalent T-atoms and 10 oxygens in

the asymmetric unit (36 TO_2 groups per unit cell). The individual [average] bond distances and angles in the frameworks are in the normal ranges for high-silica zeolites: d(T-O) = 158.0(2) - 160.2(2) [159.3] pm, ∠(O-T-O) = 107.1(2) - 111.0(1) [109.5]° and d(T-O) = 158.1(2) - 160.5(2) [159.5] pm, ∠(O-T-O) = 107.2(1) - 111.3(1) [109.5]°, for **1a** and **1b**, respectively. The ferrierite structure can be described as a completely condensed $\{^3_\infty\}[TO_{4/2}]$ network that contains a 3-dimensional framework comprised of intersecting one-dimensional 8 T-atom ring (8MR) and 10 T-atom ring (10MR) channels[6,7] (Figures 3a, 3b). For Si-FER **1**, more than 99% of the T-sites are occupied by Si-atoms and the Si : Al ratio is typically > 300 (from elemental analysis; Al and B arise from impurities in the starting materials). The channels that contain the 8MR run parallel to the crystallographic [010] direction, whereas the 10MR channels are parallel to the [100] direction and have a two-fold symmetry axis (2 ≡ C_2) as their central axis. Thus, in terms of macroscopic crystal morphology, the microscopic pores are extended parallel to the large, almost flat plate-like crystal surface, ending with openings in the narrow side faces of the crystal plates (see Figure 1d). The 8MR and 10MR channels cross each other at a 90° angle and the midpoints of their intersections are located on symmetry centers $\bar{1}$ at 0,0.5,0.5 and 0.5,0,0 (Wyckoff notation 2d in Pnnm). The pore sizes of the Si-FER framework in **1a** and **1b** with free diameters of d ≤ 463 pm and d ≤ 462 pm (8MR), d ≤ 545 pm and d ≤ 543 pm (10MR), respectively (Figure 4), are comparable to the values reported for the aluminum-containing FER framework [d(8MR) ≤ 480 pm, d(10MR) ≤ 540 pm][6,7]. The silica-walls between the larger channel pores consist of smaller 5MR and 6MR. Parallel to the a,b-plane, mainly 5MR-containing walls of slightly puckered $\{^2_\infty\}[SiO_{4/2}]$ layers occur that are connected only via 3 pairs of T-O-T bridges per unit cell. These connections cause the formation of nearly planar 6MR (point symmetry 2/m ≡ C_{2h}) parallel to the b,c-plane that

result in small 6MR 'channels' along the [100] direction that are colinear to the 10MR channels. In addition to the 6MR, the layer-connecting bridges are also part of the larger 8MR and 10MR indicating the key role of these bridges in determining the pore system of the ferrierite structure. By noting the existence of the above mentioned 6MR channels, another main feature of the ferrierite structure that occurs at the intersections of the 8MR and 6MR channels becomes evident. The increase of cross-section and ring size in both channel types at their intersection leads to a more cavity-like void, the so-called 'ferrierite cage' (see Ref. 14, p.251), namely a $[8^2 6^2 6^4 5^8]$ cage (see Figure 5a). There are two of these cages (point symmetry 2/m) per unit cell and they possess inversion centers $\bar{1}$ positioned on Wyckoff sites 2b at 0,0,0.5 and 0.5,0.5,0 that provide an I-centered lattice-type arrangement. The cages form parallel chains of 1-dimensional columns running down the [100] direction with two cages joined by one 6MR. The distance between two 6MR also represents the repeat unit along the a-axis and can be defined as cage height h = |**a**| = a. From a = 743.0 pm for the organic-containing Si-FER **1a** and a = 741.8 pm for the calcined form **1b**, an enlarging influence of the occluded organics (see below) on the ferrierite cage is observed. The overall expansion of the $\{^3_\infty\}[SiO_{4/2}]$ host framework due to the guest molecules can be expressed in terms of the unit cell volume difference with a value of $\Delta V = V_{uc}(\mathbf{1a}) - V_{uc}(\mathbf{1b}) = 17.4 \cdot 10^6$ pm^3. This expanding effect causes the framework of **1a** to be less distorted from a mmm pseudo-symmetry than the framework in **1b**, as can be seen from Figures 3a and 3b. Comparing the micropores of **1a** and **1b**, the differences of the 8MR and 10MR channels become more obvious in the shape of their cross-section than in their pore diameters (see Figures 4a, 4b). In terms of average bond parameters, the organic-containing Si-FER **1a** shows a general trend to shorter Si-O distances and larger Si-O-Si angles, compared to the organic-free material **1b** (Tables 4 and 5).

Guest molecules

From the location and values of the highest rest electron densities (see Table 1), no evidence for major extra-framework entities in the structure of Si-FER **1b** are found. In contrast, after refinement of all framework atoms in the as-synthesized Si-FER **1a**, the remaining 5 highest peaks in the difference electron map are interpreted and refined as two crystallographically different pyridine molecules. Molecule 1 (C1, C2; point symmetry 2/m) lies within the ferrierite cage, i.e., the intersection of the 6MR and 8MR channels, whereas the second molecule (C3, C4, C5; point symmetry 2/m) is located at the intersection of the 8MR and 10MR channels (Figure 3a). Therefore, the 8MR channels accomodate both types of pyridine in an alternating sequence with their 6-ring planes perpendicular to each other while the 10MR channels contain only one type of parallel orientated pyridine (molecule 1). The geometry of a non-disordered pyridine molecule would not include an inversion center $\bar{1}$, as do both of the presently found 6-rings. This fact, together with the observation of relatively sharp signals in the aromatic region of the ^{13}C and ^{1}H MAS NMR spectra (see Figure 6), indicates orientational and/or rotational disordering of the pyridines within the framework of **1a**. The disorder of the pyridine guest molecules makes it impossible to distinguish between nitrogen and carbon atoms or to determine hydrogen positions. The three highest rest electron densities, that appear after including the pyridines in the structure refinement are located close to pyridine molecule 2 at the intersection of the 8MR and 10MR channels. These electron densities are assigned to statistically underoccupied, positionally disordered 1-amino-n-propane molecules (Figure 5b), with a fixed site occupation factor (sof) of 0.05 for C6, C7 and C8. This interpretation corresponds to a 10% population of both possible, exclusively occupied amine molecule sites at special positions x, y, 0. Refinement of the sof's of C3, C4 and C5 to values around 0.4, 0.4, and 0.45, respectively, shows the position of pyridine 2 only to be occupied by ~80%. In particular, the slightly higher sof of C5 implies that this site accomodates two 'overlapping' atoms, i.e., the missing fourth atom of the aminopropane

backbone in addition to C5 of pyridine 2. Therefore, 8 out of 10 py2 sites (see Figure 3a) are occupied by pyridine 2 molecules and two by one of the aminopropane units. In final refinement cycles, the sof's for the atoms of all organic guest molecules were fixed with the values listed in Table 2. Signals occuring in the typical aliphatic region of the ^{13}C CP/MAS as well as the ^{1}H MAS NMR spectra of **1a** confirm the presence of a primary amine (Figure 6). Literature NMR data[28] can be used to exclude the existence of protonated pyridinium cations in the structure of **1a** (Table 7). Direct comparison of the sof's of the two different guest species lead to an overall pyridine (py) to aminopropane (ap) ratio of (0.5 + 0.4) : (2 x 0.05) = 9 : 1, which is in good agreement with the relative peak intensity ratios of both species derived from the ^{1}H NMR spectrum. However, comparing different batches of **1a**, variable overall py : ap ratios (NMR data) are obtained. Additionally, elemental and thermogravimetric analyses of various samples of **1a** reveal a limited variation in the ratio of the entrapped organic guests in the range of $4 : 0 \leq py : ap \leq 3 : 1$ molecules per unit cell (see Experimental Section). Due to the disorder of the organic molecules the bond lengths of pyridine 1 [d(C-C) = 135(1) - 137.7(9) pm] and 2 [d(C-C) = 133(1) - 134(1) pm] are systematically shortened, while the bond angles are within the expected ranges[29] (Table 4). Refinement of atom positions of the hardly occuring 1-amino-n-propane units failed (lead only to an approximate determination of the molecular geometry).

Host-guest interactions

A cup model representation of the structure of Si-FER **1a** using van der Waals radii for all atoms, shows that there is almost complete space-filling of the non-charged organic guest molecules within the electroneutral inorganic $\{^{3}_{\infty}\}[SiO_{4/2}]$ host framework (partly shown in Figure 5a). This result is in reasonable agreement with a comparison of void volume (V_V) data obtained from nitrogen adsorption experiments and the V_V values derived from evaluated molecular volumes (V_m) of the occluded organics. The experimental value

of 0.10 g N_2 per g **1b** at a relative nitrogen pressure of $P/P_0 = 0.3$ corresponds to V_v = 0.124 cm^3/g or $V_v \approx 440 \cdot 10^6$ pm^3 per unit cell of Si-FER. Assuming four pyridine molecules ($V_{m,py} \approx 90 \cdot 10^6$ pm^3)[30] per unit cell as guest species, the total molecular volumes would lead to a void volume of $V_v \approx 360 \cdot 10^6$ pm^3 for the Si-FER unit cell. The lower value calculated from molecular volumes is consistent with a slightly incomplete space-filling of the ferrierite micropores by the organic guests. Additional quantities that can be used to describe the interactions between the framework and the entrapped molecules in **1a** are the guest-host distances d(C···O)[31,32] that are listed in Table 6. Astonishingly, pyridine 2 [d(C···O) ≥ 354(2) pm] at the intersection of the 8MR and 10MR channel shows shorter C···O contacts than pyridine 1 in the ferrierite cage [d(C···O) ≥ 359(1) pm] (see Figure 5a). Consideration of hypothetical hydrogen positions for the pyridine molecules [d(C-H) = 108 pm][25] shows that the resulting (C)H···O distances are in the range of relatively unspecific, weak interactions that do not fulfill the geometric criteria required for the existence of C-H···O hydrogen bonds[33] (Table 6). This again reflects from a geometric point of view, the abililty of the pyridine rings to rotate within the ferrierite framework. Although, there exist only weak host-guest interactions, the shortest C_{py}···O distances (< 360 pm) mainly occur between pyridine atoms and the framework oxygens that possess the smallest T-O-T angles (< 151°) (Table 5). For the 1-amino-n-propane molecules, a slightly closer approach to the framework oxygen atoms is observed [d(C···O) ≥ 340 pm]. One reason for this could be the higher polarity of the alkyl amine in comparison to the aromatic pyridine.

Despite the relatively long C···O distances, the pyridine molecule appears to possess a high potential for shape-selective structure direction towards the ferrierite cage. Therefore, a possible but highly speculative scenario for the reaction mechanism in the nucleation phase of the organothermal synthesis could be a pre-formation of pyridine-enclathrated

cage subunits as the initial step followed by further condensation leading to the 10MR-containing FER topology. The formation of the 10MR channels in a second reaction step would also explain the indiscriminate distribution of the therein occluded organics, which only play the role of accidentally trapped, pore-filling species.

^{29}Si MAS NMR spectroscopy

The experimental and simulated ^{29}Si MAS NMR spectra of Si-FER **1a** and Si-FER **1b** are shown in Figures 7 and 8, respectively. In the highly resolved spectrum for the organic-free compound **1b**, five very sharp, distinctive signals in the chemical shift range of δ = -111.9 to -117.2 ppm with a relative intensity ratio of 2 : 2 : 2 : 1 : 2 can be observed. These resonances correspond to the five crystallographically non-equivalent T-sites, as expected from the single-crystal structure determination. In contrast, the non-CP ^{29}Si MAS NMR spectrum of the as-synthesized Si-FER **1a** shows only four well-resolved, broad peaks with chemical shifts between -113.2 and -118.1 ppm. Closer inspection of the spectrum, however, gives rise to a possible fifth resonance at either -115.6 ppm or as a weak shoulder at about -118.5 ppm. This additional signal would be necessary to match the number of crystallographically different T-atoms found in the X-ray structure of **1a**. Several simulation attempts including a peak at -115.6 ppm always specified that the resonance at -118.1 ppm has a relative intensity of ~30%. Using instead a simulated peak at -118.5 ppm, a satisfactory spectrum deconvolution is achieved and results in five peaks with an approximate intensity ratio of 2 : 2 : 2 : 2 : 1. The ^{1}H-^{29}Si CP MAS NMR spectrum of **1a** (not shown) differs only slightly from the non-CP spectrum shown in Figure 8, and reveals no obvious enhancement of any of the signals during the cross-polarization experiment. As about 90% of the shortest hydrogen silicon contacts in **1a** are $H_{py}\cdots$Si distances that are $\geq$ 339 pm (Table 6), this observation is consistent with the distance criterion [d(H···Si) < 330 pm] for efficient ^{1}H-^{29}Si polarization transfer,

recently reported for organic-containing Si-MFI samples[34,35]. Relative intensities, chemical shifts and assignments of the ^{29}Si NMR resonances for **1a** and **1b** are listed in Table 8.

The assignment of the ^{29}Si NMR peaks to the respective T-atoms was first derived in the usual manner by comparing the chemical shifts δ_T with the T-O-T bond angles $\angle$(T-O-T) = α extracted from the crystal structure data, using the well-known expression $<\rho_T> = <\cos\alpha / (\cos\alpha - 1)>$[36]. Here, $<\rho_T>$ represents the average of the cosine terms of the four T-O-T angles surrounding each T-site. Regression analysis of the obtained ρ_T,δ_T data pairs leads for both structures to the expected, pronounced linear relationship between NMR and X-ray data, as shown in Figure 9a. However, employment of a slightly modified correlation results in a perceptible improvement of the linearity for a broad range of data (Table 9). In addition to the cosine values of the T-O-T angles, the new correlation includes the individual T-O bond distances d(T-O) as a multiplicative factor, thus giving the following relationship:

$$\delta_T = b + m <\{d(T\text{-}O)\cdot[\cos\alpha / (\cos\alpha - 1)]\}> = b + m <[d(T\text{-}O)\cdot\rho_T]>.$$

The apparently better coverage of the structure flexibility is obtained by using structural information on both bond angles *and* distances. All relations applied thus far have only considered one of these closely structure-related characteristics (see Ref. 36, pp. 129 - 133). Since the values of the individual bond parameters occur not accidently, but are originated in the unique bonding situation of any particular part of a specific structure, the simultaneous use of both parameters appears merited. The driving force of periodic structure formation is mainly minimizing the free energy of a chosen system, e.g., the synthesis mixture, including enthalpy and entropy terms. For a given $\{^3_\infty\}[SiO_{4/2}]$

framework, this is reflected in the individual combinations of distances d(T-O) and angles ∠(T-O-T) that are not necessarily strongly correlated. This effect is even more obvious for the three Si-MFI structures for which accurate X-ray and NMR data are available from the literature[37-40]. The d(T-O)/sin[∠(T-O-T)] diagrams[37-39] show considerable scattering of the individual data points and thus a not well-defined relationship. The graph of the traditional ρ_T,δ_T correlation shown in Figure 9a also visibly deviates from linearity, especially when all 60 MFI data pairs are used for the regression analysis (squared correlation coefficient R^2 = 0.849). On the contrary, the modified relation maintains a remarkable linear dependence of d(T-O)·ρ_T and δ_T values, even when including all Si-MFI and Si-FER data points (R^2 = 0.939) (Figure 9b). All correlation equations in Table 9 that contain MFI data were obtained by calculating the respective bond parameters from the atom coordinates reported in the literature[37-39], and subsequently correlating them by linear regression to the chemical shifts of ^{29}Si NMR data also taken from the literature[40].

Surprisingly, the new, modified correlation derived from the data of the microporous high-silica FER and MFI zeolites also holds for the more dense SiO_2 materials cristobalite[41,42,44] and quartz[41,43,44], as can be seen from Figure 9b. Note also, that the new correlation leads to more reasonable T-O-T angles for five synthetic high-silica sodalites (Si-SOD), for which NMR data were recently published[45]. Due to the high symmetry (space group $I\bar{4}3m$ or $Im\bar{3}m$), the Si-SOD framework contains only one crystallographically independent T-O distance and one T-O-T angle. Assuming a bond distance of d(T-O) = 159.0 pm, angles in the range of α = 155.5 - 158.8° are obtained and are below the theoretical maximum value of 160.5° reported for a completely expanded

SOD framework[46]. With the previously described correlation, $\delta_T = 2.19 - 247.05 <[\cos \alpha / (\cos \alpha - 1)]>$[47], three angles with $\alpha > 160.5°$ are obtained[45].

2.4 Summary

The detailed structure investigation of the as-synthesized, i.e., organic-containing, and the calcined, i.e., organic-free form of high-silica ferrierite (Si-FER) presented in this work demonstrates that even weak interactions between a host framework and enclathrated guest species can cause visible distortion of a $\{^3_\infty\}[TO_{4/2}]$ network. This distortion is reflected in the individual differences of T-O bond lengths *and* T-O-T bond angles in the Si-FER framework of the organic-containing and the organic free material. Taking into account both bond parameters, a remarkably good linear relationship between the geometric structure data and the spectroscopic data from ^{29}Si NMR chemical shifts can be obtained. It should be noted, however, that highly accurate data from both XRD and NMR investigations are required to obtain this well-defined linear correlation.

Acknowledgments

Financial support for this work was provided by the Gas Research Institute and the National Science Foundation (Grant No. CTS-9114829). The authors also gratefully acknowledge Dr. Saeed Khan at the University of California at Los Angeles for his expert assistance in collecting the single crystal data sets. Dr. Hubert Koller and Shervin Khodabandeh also provided assistance with recording and interpreting the NMR spectra.

Supplementary Material

Listings of anisotropic displacement parameters for all refined atoms (Tables A1, A2) and structure factor amplitudes (Tables A3, A4) are given in the appendix.

Literature Cited

[1] Venuto, P. B. *Microporous Mater.* **1994**, *2*, 297.

[2] Ozin, G. A.; Gil, C. *Chem. Rev.* **1989**, *89*, 1749.

[3] Davis, M. E.; Lobo, R. F. *Chem Mater.* **1992**, *4*, 756.

[4] Zones, S. I.; Olmstead, M. M.; Santilli, D. S. *J. Am. Chem. Soc.* **1992**, *114*, 4195.

[5] Yoon, K. B. *Chem. Rev.* **1993**, *93,* 321.

[6] Meier, W.M.; Olson, D.H. *Atlas of Zeolite Structure Types*, Butterworth-Heinemann: Boston, 1992.

[7] Vaughan, P. A. *Acta Crystallogr.* **1966**, *21*, 983.

[8] Wise, W. S.; Tschernich, R. W. *Am. Mineral.* **1976**, *61*, 60.

[9] Smith, B. K. *Am. Mineral.* **1986**, *71*, 989.

[10] Szostak, R. *Handbook of Molecular Sieves;* Van Nostrand Reinhold: New York, 1992.

[11] Liebau, F. *Structural Chemistry of Silicates*; Springer: New York, 1985; p72.

[12] Gramlich-Meier, R.; Meier, W. M.; Smith, B. K. *Z. Kristallogr.* **1984**, *169*, 201.

[13] Gramlich-Meier, R.; Gramlich, V.; Meier, W. M. *Am. Mineral.* **1985**, *70*, 619.

[14] Alberti, A.; Sabelli, C. *Z. Kristallogr.* **1987**, *178*, 249.

[15] Rice, S. B.; Treacy, M. M. J.; Newsam, J. M. *Zeolites* **1994**, *14*, 335.

[16] Jacob, N. E.; Joshi, P. N.; Shaikh, A. A.; Shiralkar, V. P. *Zeolites* **1993**, *13*, 430.

[17] Gies, H.; Gunawardane, R. P. *Zeolites* **1987**, *7*, 442.

[18] Kuperman, A.; Nadimi, S.; Oliver, S.; Ozin, G. A.; Garcés, J. M.; Olken, M. M. *Nature* **1993**, *365*, 239.

[19] Nadimi, S.; Oliver, S.; Kuperman, A.; Lough, A.; Ozin, G. A. ; Garcés, J. M.; Olken, M. M.; Rudolf, P. In *Proceedings of the 10th International Zeolite Conference*; Weitkamp, J., Karge, H. G., Pfeifer, H., Hölderich, W., Eds.; Elsevier: Amsterdam, 1994; Vol. 84A, pp. 93-100.

[20] Morris, R. E.; Weigel, S. J.; Henson, N. J.; Bull, L. M.; Janicke, M. T.; Chmelka, B. F.; Cheetham, A. K. *J. Am. Chem. Soc.* **1994**, *116*, 11849.

[21] Hathaway, P. E.; Davis, M. E. *Catal. Lett.* **1990**, *5*, 333.

[22] Sheldrick, G. M. *Acta Crystallogr., Sect A* **1990**, *46*, 467.

[23] Sheldrick, G. M. *J. Appl. Crystallogr.*, In preparation.

[24] *International Tables for Crystallography*; Wilson, A. J. C., Ed.; Kluwer Academic: Dordrecht, 1992, Vol. C.

[25] Allen, F. H. *Acta Crystallogr., Sect. B* **1986**, *42*, 515.

[26] Keller, E. *J. Appl. Crystallogr.* **1989**, *22*, 19.

[27] Johnson, C. K. *Ortep II* Report ORNL-5138, Oak Ridge National Laboratory, 1974.

[28] *The Aldrich Library of ^{13}C and ^{1}H FT NMR Spectra Edition I*; Pouchert, C. J., Behnke, J., Eds.;Aldrich: Milwaukee, 1993, Vol. 1 and 3.

[29] Mootz, D.; Wussow, H. G. *J. Chem. Phys.* **1981**, *75*, 1517.

[30] Gavezzotti, A. *J. Am. Chem. Soc.* **1983**, *103*, 5220.

[31] Emmer, J.; Wiebcke, M. *J. Chem. Soc., Chem Commun.* **1994**, 2079.

[32] Behrens, P.; van de Goor, G.; Freyhardt, C. C. *Angew. Chem.*, in press.

[33] Steiner, T. *J. Chem. Soc., Chem Commun.* **1994**, 101.

[34] Lefebvre, F.; Sacerdote-Peronnet, M.; Mentzen, B. F. *C. R. Acad. Sci. Paris, Ser. 2* **1993**, *316*, 1549.

[35] Burkett, S. L.; Davis, M. E. *J. Phys. Chem.* **1994**, *98*, 4647.

[36] Engelhardt, G.; Michel, D. *High-Resolution Solid State NMR of Silicates and Zeolites*; Wiley: Chichester, 1987.

[37] van Koningsveld, H.; Tuinstra, F.; van Bekkum, H., Jansen, J. C. *Acta Crystallogr., Sect. B* **1989**, *45*, 423.

[38] van Koningsveld, H. *Acta Crystallogr., Sect. B* **1990**, *46*, 731.

[39] van Koningsveld, H.; Jansen, J. C.; van Bekkum, H. *Zeolites* **1990**, *10*, 235.

[40] Fyfe, C. A.; Feng, Y.; Grondey, H. *Microporous Mater.* **1993**, *1*, 939.

[41] Lippmaa, E.; Mägi, M.; Samoson, A.; Engelhardt, G. *J. Am. Chem. Soc.* **1980**, *102*, 4889.

[42] Peacor, D. R. *Z. Kristallogr.* **1973**, *138*, 274.

[43] Wright, A. F.; Lehman, M. S. *J. Solid State Chem.* **1981**, *36*, 371.

[44] Smith, J. V.; Blackwell, C. S. *Nature* **1983**, *303*, 223.

[45] Braunbarth, C. M.; Behrens, P.; Felsche, J.; van de Goor, G.; Wildermuth, G.; Engelhardt, G. *Zeolites*, in press.

[46] Depmeier, W. *Acta Crystallogr., Sect. B* **1984**, *40*, 185.

[47] Engelhardt, G.; Radeglia, R. *Chem. Phys. Lett.* **1984**, *108*, 271.

Table 2.1 $[Si_{36}O_{72}]\{py_{(4-x)}ap_x\}$ (**1a**, x = 0.4), $[Si_{36}O_{72}]$ (**1b**); crystal data and details of intensity measurement and structure refinement.

	1a	**1b**
Chemical formula	$[Si_{36}O_{72}]$ $\{(C_5H_5N)_{3.6}(C_3H_9N)_{0.4}\}$	$[Si_{36}O_{72}]$
Formula weight	2471.69	2163.24
Crystal size [mm]	0.24 x 0.21 x 0.01	0.22 x 0.20 x 0.01
Crystal system	orthorhombic	orthorhombic
Space Group (No.); Z	Pnnm (58); 1	Pnnm (58); 1
a [pm]	743.0(1)	741.8(1)
b [pm]	1409.2(2)	1407.0(2)
c [pm]	1882.0(2)	1871.3(2)
V [10^6·pm^3]	1970.5(4)	1953.1(4)
T [K]	298	298
d_{calc} [Mg · m^{-3}]	2.083 (1.823[a])	1.839
Framework density [T-atoms / 10^9·pm^3]	18.27	18.43
F (000)	1244.8	1080
μ ($CuK_{<\alpha>}$) [mm^{-1}]	6.64	6.59
Range of 2θ [°]	8 - 120	8 - 120
Range of indices h, k, l	-8≤h≤8 0≤k≤15 0≤l≤21	0≤h≤8 0≤k≤15 0≤l≤21
No. of reflections measured	3179	1717
No. of unique reflections i	1524 (R_{int} = 0.039)	1514
No. of observed reflections m ($I > 2\sigma_I$)	1112	1370
Refined parameters n	160	126
No. of restraints	3[b]	0
$R = \Sigma(\Delta F)/\Sigma F$[c]	0.041 (0.054)	0.037 (0.041)
$R_W = [\Sigma w(\Delta F^2)^2/\Sigma w(F^2)^2]^{1/2}$[c,d]	0.133 (0.149)	0.125 (0.130)
$S = \{\Sigma[w(\Delta F^2)^2]/(m-n)\}^{1/2}$[d]	1.183	1.283
min, max $\Delta\rho$ [e · Å^{-3}]	-0.54, +0.64[e]	-0.51, +0.49[e]

[a] Value considering only framework atoms

[b] Distances between carbon atoms C3, C4 and C5 of pyridine molecule 2

[c] Values for observed data (all data)

[d] For weighting scheme w, see experimental section

[e] In close proximity to framework atoms Si (-) and O (+), respectively

Table 2.2 Fractional atomic coordinates and equivalent isotropic or isotropic displacement parameters [$10^4 pm^2$] for **1a**.

Atom	sof	x	y	z	$100 \cdot U_{eq/iso}$[a]
Si1	0.5	0.00000	0.50000	0.15329(7)	0.90(4)
Si2	1.0	0.29308(12)	0.50020(5)	0.27299(5)	1.12(4)
Si3	1.0	0.21099(11)	0.29920(6)	0.32667(4)	1.09(4)
Si4	1.0	0.29746(11)	0.20331(6)	0.17749(4)	1.06(4)
Si5	1.0	0.00324(9)	0.29941(6)	0.08367(5)	0.87(4)
O12	1.0	0.1751(4)	0.4964(1)	0.2024(1)	3.24(8)
O15	1.0	-0.0062(3)	0.4088(2)	0.1041(2)	2.80(7)
O22	0.5	0.5000	0.5000	0.2498(2)	2.30(10)
O23	1.0	0.2509(3)	0.4107(2)	0.3221(1)	2.55(7)
O24	1.0	0.2481(3)	0.5927(2)	0.3184(1)	2.67(7)
O34	1.0	0.2630(3)	0.2504(1)	0.2536(1)	3.49(8)
O35	1.0	0.3270(3)	0.2542(2)	0.3892(1)	2.42(6)
O43	1.0	0.5034(2)	0.2184(2)	0.1555(1)	2.25(7)
O45	1.0	0.1770(3)	0.2526(2)	0.1190(1)	2.64(7)
O55	0.5	0.0163(4)	0.2880(3)	0.0000	2.23(9)
C1	0.5	0.5019(11)	0.4014(8)	0.0000	8.6(4)
C2	1.0	0.5004(8)	0.4520(5)	0.0626(5)	8.8(2)
C3	0.40	0.311(3)	-0.011(4)	0.000	14.0(10)
C4	0.40	0.391(7)	0.074(2)	0.000	15.2(11)
C5	0.45	0.570(7)	0.081(1)	0.000	13.2(7)
C6	0.05	0.226	-0.047	0.000	10.0*
C7	0.05	0.230	0.051	0.000	10.0*
C8	0.05	0.404	0.107	0.000	10.0*

[a] U_{eq} is defined as one third of the trace of the orthogonalized U_{ij} tensor. Non-marked values denote U_{eq}, values marked with * denote U_{iso}

Table 2.3 Fractional atomic coordinates and equivalent isotropic displacement parameters [$10^4 pm^2$] for **1b**.

Atom	sof	x	y	z	$100 \cdot U_{eq}$[a]
Si1	0.5	0.00000	0.50000	0.15308(6)	0.98(3)
Si2	1.0	0.29257(11)	0.50045(4)	0.27302(5)	1.21(3)
Si3	1.0	0.21818(10)	0.30140(5)	0.33089(4)	1.04(3)
Si4	1.0	0.30497(10)	0.20609(5)	0.18112(4)	0.98(3)
Si5	1.0	0.00876(9)	0.29945(5)	0.08351(4)	0.83(3)
O12	1.0	0.1749(3)	0.4908(1)	0.2022(1)	3.13(6)
O15	1.0	-0.0171(3)	0.4088(2)	0.1038(1)	2.66(6)
O22	0.5	0.5000	0.5000	0.2503(2)	2.52(9)
O23	1.0	0.2520(3)	0.4139(1)	0.3258(1)	2.50(6)
O24	1.0	0.2455(3)	0.5956(1)	0.3150(1)	2.99(6)
O34	1.0	0.2841(3)	0.2517(2)	0.2585(1)	2.98(6)
O35	1.0	0.3307(3)	0.2589(1)	0.3961(1)	1.86(5)
O43	1.0	0.5089(2)	0.2185(2)	0.1550(1)	2.43(6)
O45	1.0	0.1780(3)	0.2579(1)	0.1255(1)	2.38(6)
O55	0.5	0.0444(4)	0.2893(2)	0.0000	1.77(7)

[a] U_{eq} is defined as one third of the trace of the orthogonalized Uij tensor.

Table 2.4 Bond lengths [pm] and angles [°] for Si-FER **1a** and Si-FER **1b**[a].

	1a	**1b**		**1a**	**1b**
framework					
Si1-O12	159.6(3)	159.5(2)	O12-Si1-O12 [i]	109.3(2)	109.7(2)
Si1-O12 [i]	159.6(3)	159.5(2)	O12-Si1-O15	109.6(1)	109.5(1)
Si1-O15	158.4(3)	158.5(2)	O12-Si1-O15 [i]	109.9(1)	109.6(1)
Si1-O15 [i]	158.4(3)	158.5(2)	O12 [i]-Si1-O15	109.9(1)	109.6(1)
			O12 [i]-Si1-O15 [i]	109.6(1)	109.5(1)
			O15-Si1-O15 [i]	108.5(2)	108.9(2)
<Si1-O>	159.0	159.0	<O-Si1-O>	109.5	109.5
Si2-O12	159.3(3)	159.4(3)	O12-Si2-O22	107.5(2)	107.8(2)
Si2-O22	159.8(1)	159.7(1)	O12-Si2-O23	110.4(1)	110.2(1)
Si2-O23	159.5(2)	159.7(2)	O12-Si2-O24	111.0(1)	111.3(1)
Si2-O24	159.3(2)	159.1(2)	O22-Si2-O23	110.3(1)	110.1(1)
			O22-Si2-O24	110.5(1)	110.3(1)
			O23-Si2-O24	107.1(2)	107.2(1)
<Si2-O>	159.5	159.5	<O-Si2-O>	109.5	109.5
Si3-O23	160.2(2)	160.5(2)	O23-Si3-O34	109.5(1)	109.4(1)
Si3-O34	158.6(2)	160.0(2)	O23-Si3-O35	109.3(1)	109.5(1)
Si3-O35	159.0(2)	159.4(2)	O23-Si3-O43 [ii]	110.0(2)	109.5(1)
Si3-O43 [ii]	159.8(2)	160.0(2)	O34-Si3-O35	109.7(1)	108.9(1)
			O34-Si3-O43 [ii]	110.5(1)	111.1(1)
			O35-Si3-O43 [ii]	107.8(1)	108.4(1)
<Si3-O>	159.4	160.0	<O-Si3-O>	109.5	109.5
Si4-O24 [iii]	159.8(2)	160.1(2)	O24 [iii]-Si4-O34	109.1(1)	109.1(1)
Si4-O34	159.9(2)	159.2(2)	O24 [iii]-Si4-O43	110.2(2)	110.0(1)
Si4-O43	159.9(2)	159.9(2)	O24 [iii]-Si4-O45	110.1(1)	109.8(1)
Si4-O45	158.0(2)	158.1(2)	O34-Si4-O43	109.3(1)	109.0(1)
			O34-Si4-O45	110.6(1)	110.8(1)
			O43-Si4-O45	107.7(1)	108.2(1)
<Si4-O>	159.4	159.3	<O-Si4-O>	109.5	109.5

Table 2.4 (cont.) Bond lengths [pm] and angles [°] for Si-FER **1a** and Si-FER **1b**[a].

	1a	**1b**		**1a**	**1b**
Si5-O15	159.0(3)	159.7(2)	O15-Si5-O35 ^{ii}	110.2(1)	109.8(1)
Si5-O35 ^{ii}	159.6(2)	160.2(2)	O15-Si5-O45	109.6(1)	109.3(1)
Si5-O45	159.5(2)	159.3(2)	O15-Si5-O55	110.0(2)	109.9(1)
Si5-O55	158.6(1)	159.13(9)	O35 ^{ii}-Si5-O45	109.6(2)	110.1(1)
			O35 ^{ii}-Si5-O55	108.7(2)	109.0(1)
			O45-Si5-O55	108.8(2)	108.7(1)
<Si5-O>	159.2	159.6	<O-Si5-O>	109.5	109.5
<Si-O>	159.3	159.5	<O-Si-O>	109.5	109.5
pyridine 1					
C1-C2	137.7(9)		C2-C1-C2 ^{vii}	117.6(10)	
C2-C2 ^{iv}	135(2)		C1-C2-C2 ^{iv}	121.2(5)	
pyridine 2					
C3-C4	134(1)		C4-C3-C5 ^{viii}	112(2)	
C3-C5 ^{viii}	133(1)		C3-C4-C5	121(2)	
C4-C5	134(1)		C4-C5-C3 ^{viii}	127(2)	
1-amino-n-propane					
C5 ^{viii}-C6	159(6)		C5 ^{viii}-C6-C7	106.3(6)	
C6-C7	138		C6-C7-C8	123	
C7-C8	152				

[a] Symmetry transformations used to generate equivalent atoms:
i: -x,-y+1,z ii: x-1/2,-y+1/2,-z+1/2 iii: -x+1/2,y-1/2,-z+1/2
iv: -x+1,-y+1,z

v: -x+1/2,y+1/2,-z+1/2 vi: x+1/2,-y+1/2,-z+1/2 vii: x,y,-z
viii: -x+1,-y,-z ;

< > = average values

Table 2.5 Bond angles ∠(T-O-T) [°] for **1a** and **1b** and the two shortest host-guest contacts d(O···C_{py}) [pm] for pyridine molecules in **1a**.

T-O-T[a]	**1a**	**1b**	**1a**[b]	
Si1-O12-Si2	158.5(5)	156.6(2)	363 $_{C2}$	364 $_{C2}$
Si1-O15-Si5	157.9(2)	155.4(2)	380 $_{C2}$	389 $_{C2}$
Si2-O22-Si2 ^{iv}	148.3(3)	149.1(3)	359 $_{C2}$	359 $_{C2}$
Si2-O23-Si3	147.5(2)	144.9(2)	355 $_{C3}$	361 $_{C5}$
Si2-O24-Si4 ^{v}	150.3(2)	153.0(2)	358 $_{C4}$	374 $_{C3}$
Si3-O34-Si4	174.8(2)	167.4(2)	489 $_{C2}$	491 $_{C2}$
Si3-O35-Si5 ^{vi}	150.5(2)	143.7(1)	365 $_{C5}$	387 $_{C1}$
Si4-O43-Si3 ^{vi}	148.1(2)	148.1(2)	354 $_{C5}$	366 $_{C4}$
Si4-O45-Si5	158.6(2)	164.5(2)	372 $_{C4}$	385 $_{C2}$
Si5-O55-Si5 ^{vii}	166.4(3)	158.3(2)	395 $_{C1}$	410 $_{C4}$
<Si-O-Si>	156.1	154.1		

[a] For symmetry codes, see Table 4

[b] Respective carbon atoms are denoted as subscripts

Table 2.6 Shortest guest-host distances d(C···O), d(H_{py}···O) and d(H_{py}···Si) [pm], and angles ∠(C-H_{py}···O) [°] for Si-FER **1a**[a].

pyridine 1							
C1···O35 vi	387.2(9)	H1···O43	329	C1-H1···O43	117	H1···Si3 vi	401
C2···O22	358.7(10)	H2···O22	285	C2-H2···O22	125	H2···Si4	355
pyridine 2							
C3···O23 iii	355(2)	H3···O23 iii	354	C3-H3···O23 iii	82	H3···Si3 iii	423
C4···O24 iii	358(1)	H4···O45	293	C4-H4···O45	130	H4···Si4	347
C5···O43	354(2)	H5···O35 vi	289	C5-H5···O35 vi	128	H5···Si3 vi	339
1-amino-n-propane							
C6···O23 iii	340						
C7···O24 iii	347						
C8···O43	340						

[a] For symmetry codes, see Table 4

Table 2.7 ^{13}C CP/MAS and ^{1}H MAS NMR data for Si-FER **1a** and literature data for pyridine, pyridine · HCl and 1-amino-n-propane (Ref. 28).

	Chemical shift [ppm]			
	1a	pyridine	pyridine · HCl	1-amino-n-propane
^{13}C	124.2, 136.0, 150.8 12.3, 27.3, 44.9	123.6, 135.8,149.8	127.5, 141.0, 146.3	11.3, 26.8, 44.1
^{1}H	7.40, 8.77 1.11, 2.69	7.35, 7.64, 8.60	8.20, 8.68, 9.03	0.91, 1.46, 1.78, 2.65

Table 2.8 Comparison of ^{29}Si MAS NMR data with single-crystal XRD data for Si-FER **1a** and Si-FER **1b**[a].

T-site	**1a**				**1b**			
	$<\rho_T>$	$<[d(T\text{-}O) \cdot \rho_T]>$	δ_T [ppm]	r.i. [%]	$<\rho>$	$<[d(T\text{-}O) \cdot \rho_T]>$	δ_T [ppm]	r.i. [%]
Si1	0.48137	0.76538	-118.5	8.3	0.47739	0.75906	-116.5	10.5
Si2	0.46597	0.74309	-113.2	20.4	0.46532	0.74205	-112.3	22.4
Si3	0.47025	0.74949	-114.2	26.3	0.46226	0.73951	-111.9	22.6
Si4	0.47628	0.75917	-116.5	23.0	0.47868	0.76257	-117.2	23.6
Si5	0.48033	0.76453	-118.1	21.9	0.47367	0.75580	-116.2	21.0

[a] $\rho_T = [\cos \alpha / (\cos \alpha - 1)]$, with $\alpha = \angle(T\text{-}O\text{-}T)$, see Ref 36; r.i.: relative signal intensity obtained from spectrum simulation.

Table 2.9 Correlation of chemical shifts δ from ^{29}Si MAS NMR data with single-crystal XRD data; results of linear regression analyses (R^2: correlation coefficient squared) for some high-silica zeolites.

Zeosil[a]	$\delta_T = b + m \cdot \langle\rho_T\rangle$[b]	R^2	$\delta_T = b + m \cdot \langle[d(T\text{-}O) \cdot \rho_T]\rangle$[b]	R^2	Number of data points	Ref.
Si-FER(as)$_{RT}$	δ = 51.61 - 353.20 x	0.993	δ = 64.66 - 239.00 x	0.987	5	this work
Si-FER(c)$_{RT}$	δ = 44.60 - 338.13 x	0.971	δ = 66.34 - 240.96 x	0.990	5	this work
Si-FER	δ = 48.84 - 347.25 x	0.981	δ = 67.46 - 242.57 x	0.988	10	this work
Si-MFI(c)$_{RT}$	δ = 23.12 - 291.27 x	0.986	δ = 40.84 - 206.27 x	0.989	24	39, 40
Si-MFI(c)$_{HT}$	δ = 8.60 - 258.73 x	0.970	δ = 29.36 - 190.61 x	0.968	12	38, 40
Si-MFI(px-l)	δ = 27.64 - 302.89 x	0.977	δ = 42.49 - 209.47 x	0.990	24	37, 40
Si-MFI	δ = 17.21 - 279.14 x	0.849	δ = 42.99 - 209.46 x	0.937	60	37 - 40
Si-FER, Si-MFI	δ = 23.56 - 292.79 x (shown in Figure 9a)	0.864	δ = 48.54 - 216.95 x (shown in Figure 9b)	0.939	70	this work, 37 - 40

[a] as: as synthesized, c: calcined; RT = 298 K, HT = 350 K; px-l: reloaded with p-xylene

[b] δ_T = chemical shift for T-site (T = Si); $\rho_T = [\cos\alpha / (\cos\alpha - 1)]$ with $\alpha = \angle$(T-O-T), see Ref. 36; < > = average values, see also text

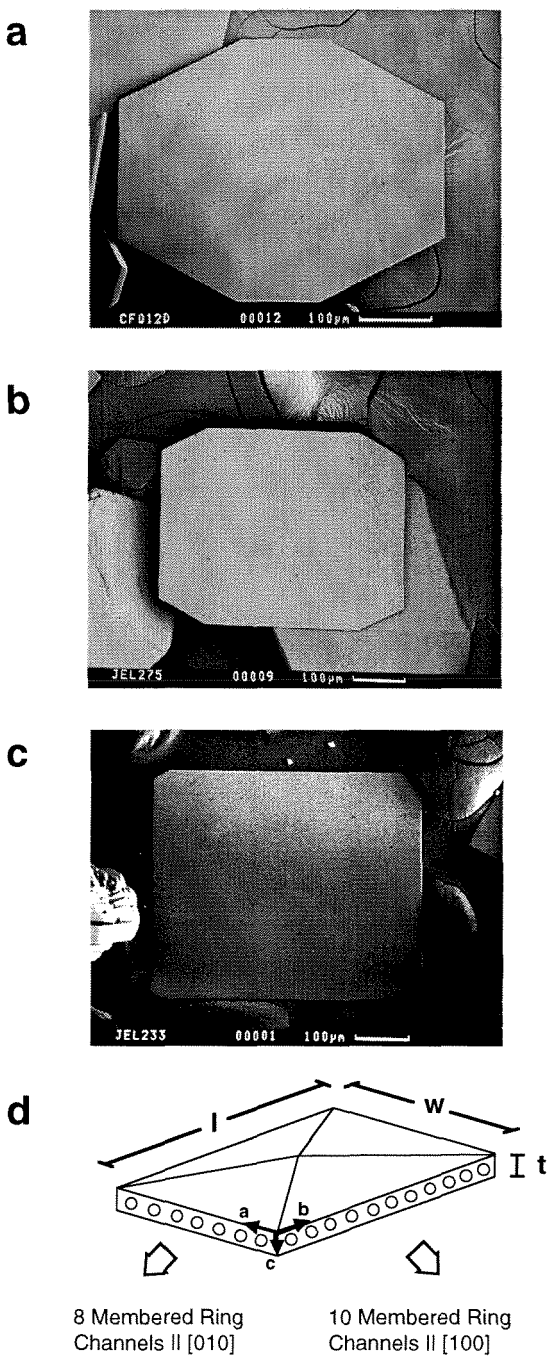

Figure 2.1 Single-crystals of high-silica ferrierite Si-FER (**1b**) obtained from organothermal synthesis; SEM images of crystals from different batches (a-c), schematic representation of crystal morphology and its relation to the micropore structure (d). l, w and t denote crystal dimensions length, width and thickness, respectively.

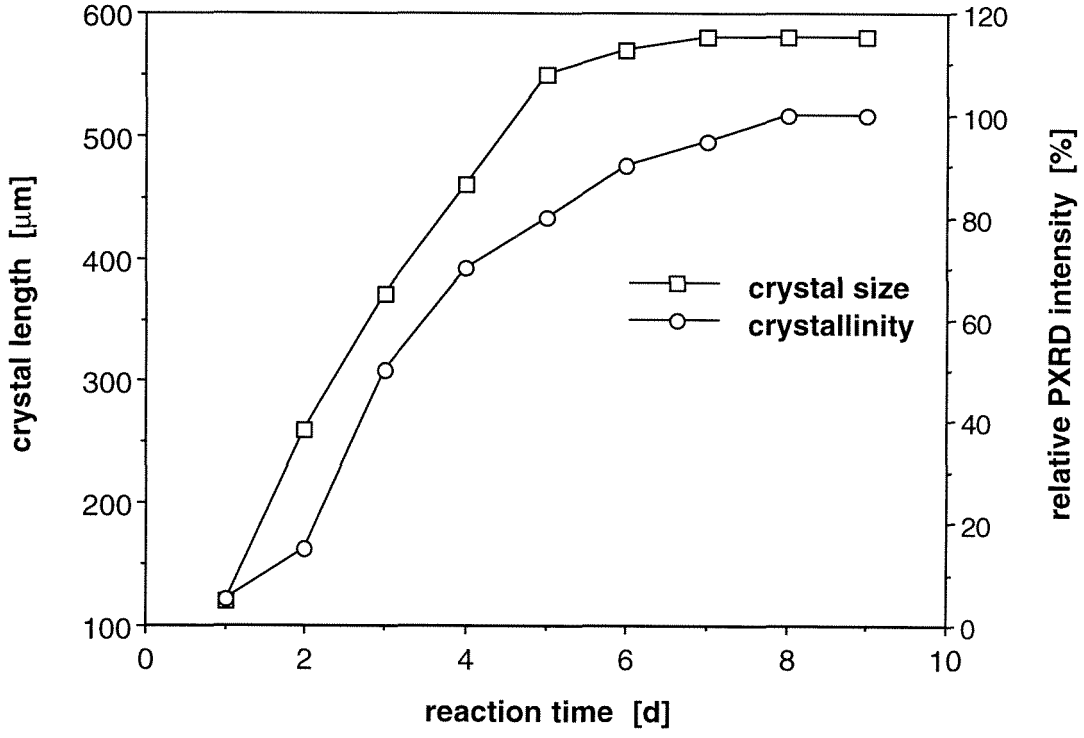

Figure 2.2 Maximum crystal size and average crystallinity during the course of organothermal Si-FER synthesis; crystallinity determination is based on powder X-ray diffraction (PXRD) data [(015) reflection].

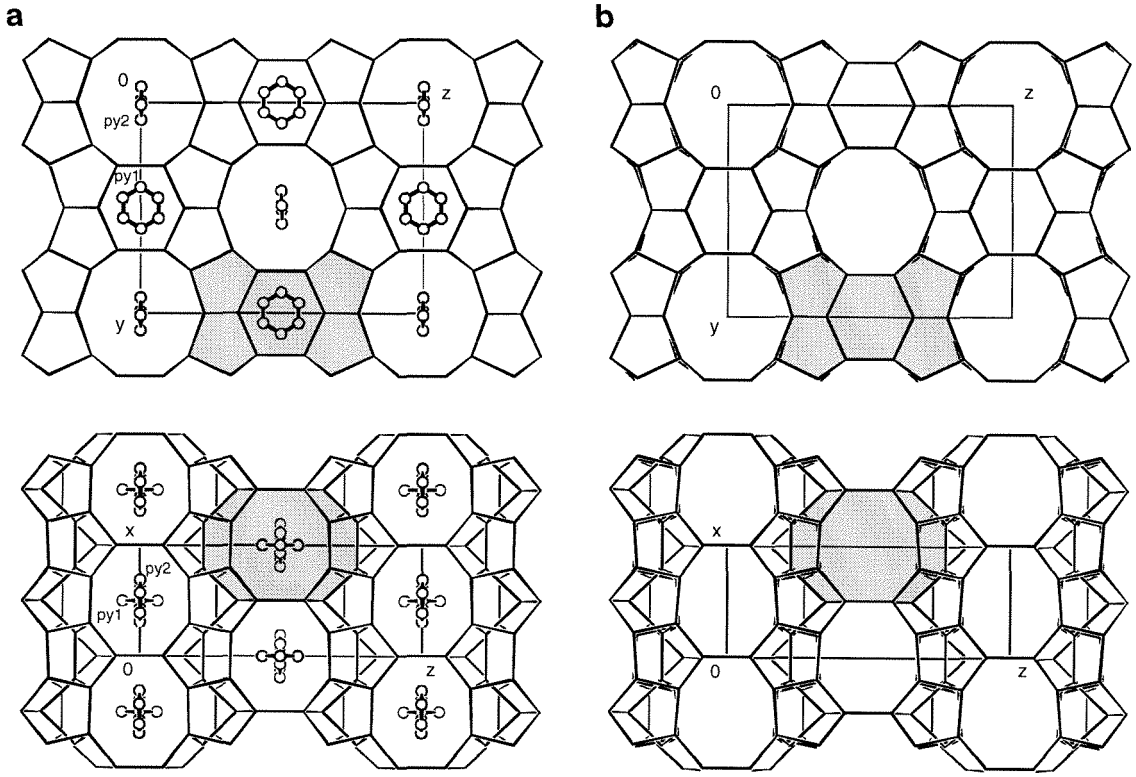

Structure **1a** Structure **1b**

Figure 2.3 Single-crystal structures of as synthesized Si-FER (**1a**) (a) and calcined Si-FER (**1b**) (b) as viewed along the 10MR channels ([100] direction, top) and 8MR channels ([010] direction, bottom), respectively. Oxygen atoms of the $\{^3{}_\infty\}[TO_{4/2}]$ host frameworks are omitted for clarity and the T-T distances are represented as straight lines; shaded areas depict one cage-type subunit. The two crystallographically different pyridine guest molecules in **1a** are designated as py1 and py2, 1-amino-n-propane units are not shown.

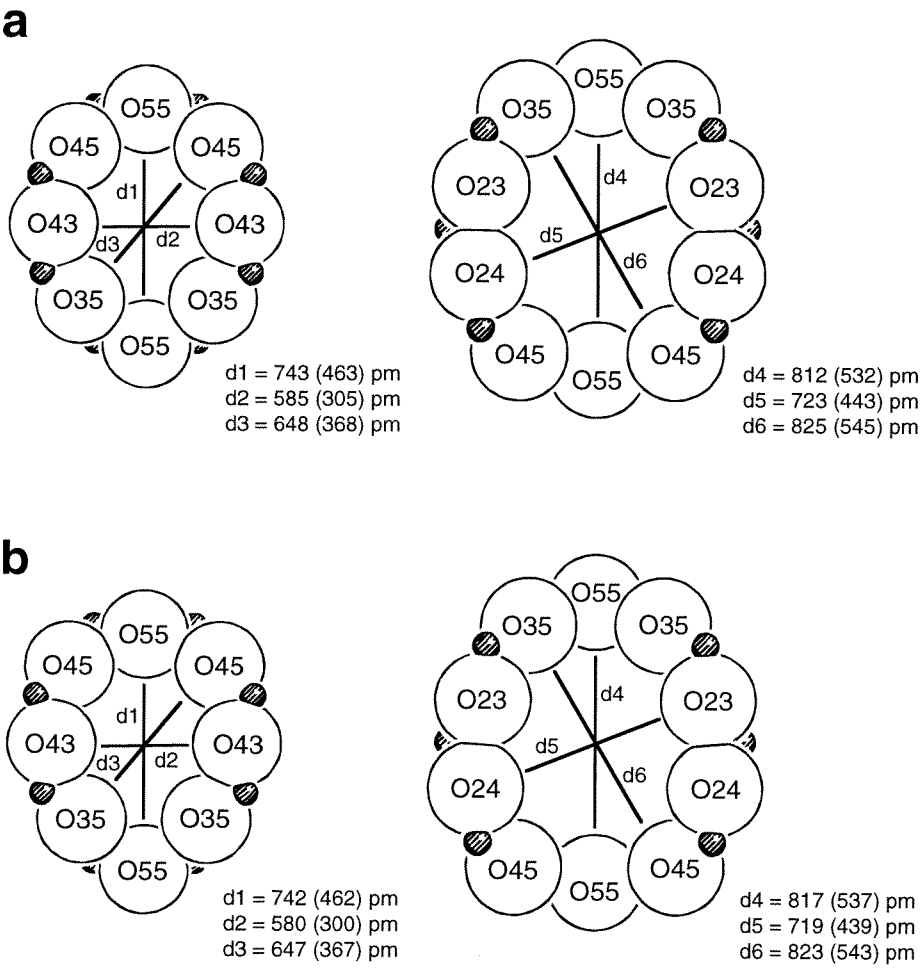

Figure 2.4 Pore sizes for **1a** (a) and **1b** (b) at the 8MR (left) and 10MR (right). Ring diameters are given as respective O(center)-O(center) distances; values in brackets denote approximate free diamters obtained by subtracting two times the van der Waals radius of oxygen [$r(O)_{vdW}$ = 140 pm].

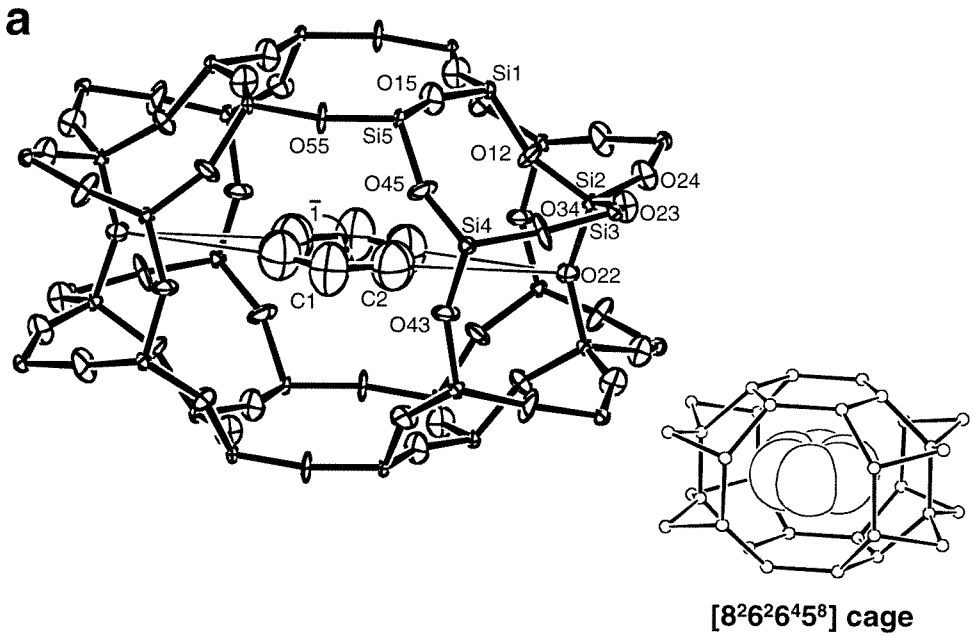

Figure 2.5 Details of the crystal structure of the organic-containing Si-FER **1a**. Cage-like void section with enclathrated pyridine 1; the shortest $C_{py1}\cdots O$ distances (359 pm) are drawn as thin lines (a). Pyridine 2 (left, 80% occupied) and disordered 1-amino-n-propane molecules (right, each 10% occupied) with superimposedimage (center) of mutually exclusive molecules located at position py2 in Figure 3a (b). Inversion centers are marked by o; displacement ellipsoids correspond to the 50% (a) and 30% (b) probability level, respectively.

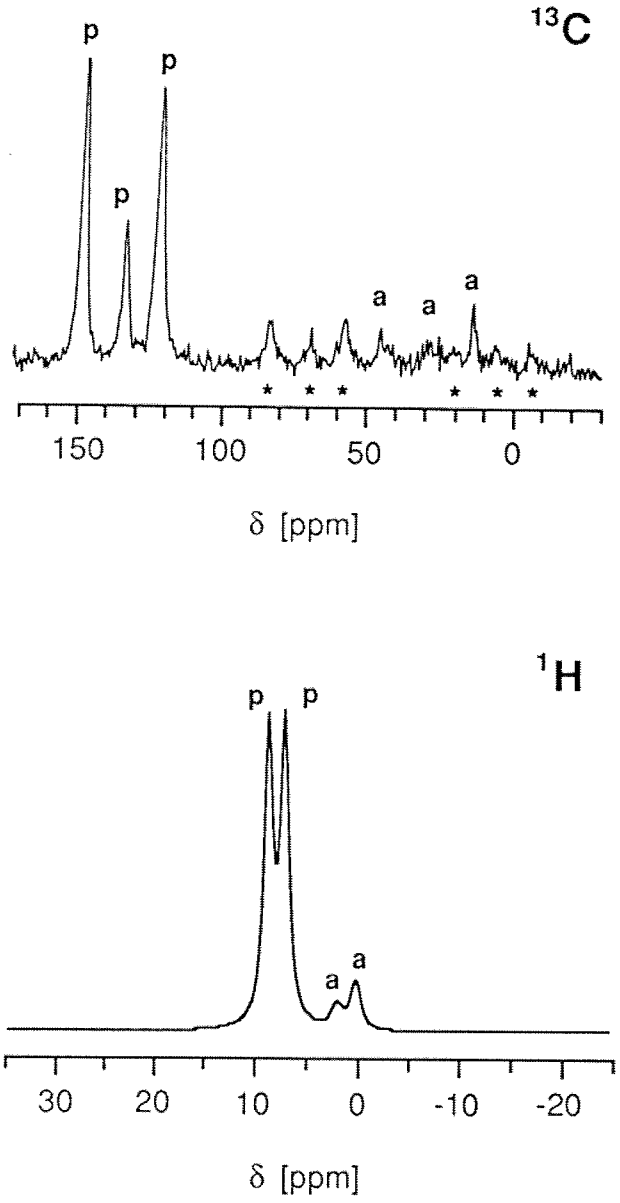

Figure 2.6 ^{13}C CP/MAS (top) and ^{1}H MAS NMR spectrum (bottom) of Si-FER **1a**; respective chemical shifts are listed in Table 7. Signals assigned to pyridine, 1-amino-n-propane and spinning sidebands are labelled as p, a and *, respectively.

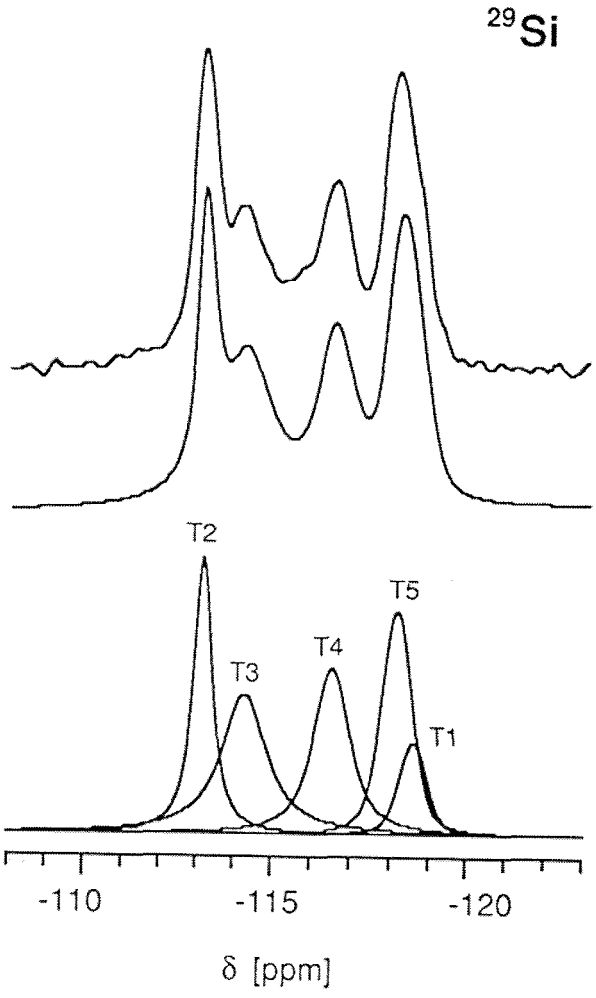

Figure 2.7 Experimental (top), simulated (middle) and deconvoluted (bottom) non-CP ^{29}Si MAS NMR spectrum of as-synthesized Si-FER **1a**; for chemical shifts and assignment of T-sites see Table 8.

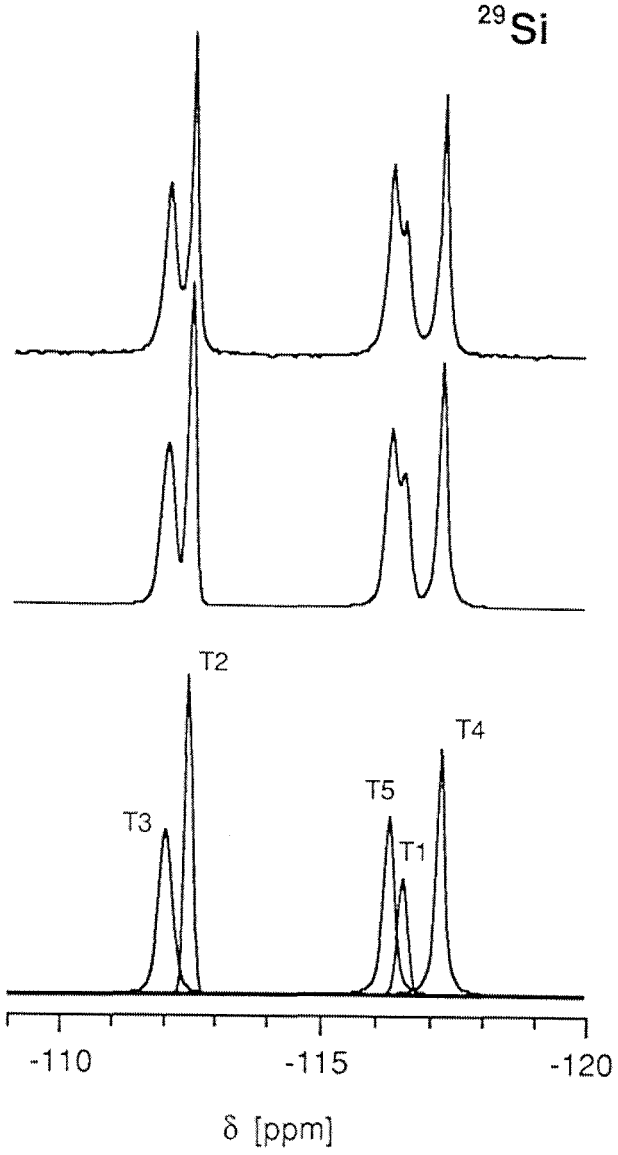

Figure 2.8 Experimental (top), simulated (middle) and deconvoluted (bottom) non-CP ^{29}Si MAS NMR spectrum of calcined Si-FER **1b**; for chemical shifts and assignment of T-sites see Table 8.

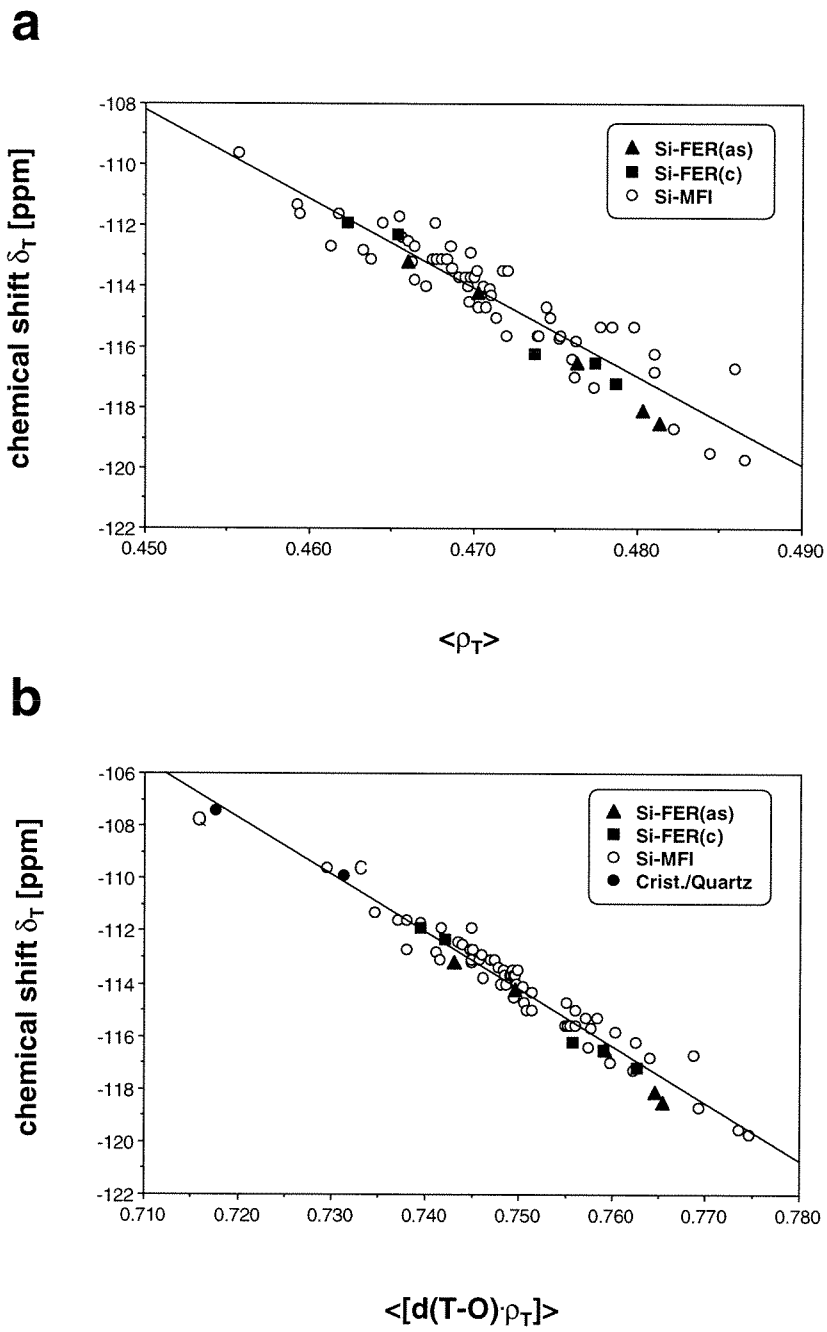

Figure 2.9 Traditional (a) and new (b) linear correlation of chemical shifts δ_T from ^{29}Si MAS NMR data with single-crystal XRD data for microporous high-silica zeolites (<> = average values, $\rho_T = [\cos \alpha / (\cos (\alpha - 1)]$ with $\alpha = \angle$(T-O-T), see Ref. 36); in (b) data points for the dense SiO_2 phases cristobalite (C, Ref. 41, 42, 44) and quartz (Q, Ref. 41, 43, 44) are added.

Chapter 3

Permeation Studies On Oriented Single-Crystal Ferrierite Membranes

---

Submitted for publication in The AIChE Journal

Permeation Studies on Oriented Single-Crystal Ferrierite Membranes

John E. Lewis, Jr., George R. Gavalas and Mark E. Davis

Chemical Engineering, California Institute of Technology

Pasadena, CA 91125

Abstract

Large, high quality, single-crystals of pure-silica ferrierite (FER) are synthesized and the single-crystal structure described (Lewis et al., 1996). Selected individual crystals (approximately 600 μm x 500 μm x 20 μm) are mounted in a membrane configuration so that only the 10-membered ring channels (5.4 Å x 5.4 Å x 4.2 Å) or the 8-membered ring channels (4.6 Å x 3.7 Å x 3.0 Å) are accessible for gas molecule permeation. The first examples of transport exclusively through 8- or 10-membered ring channel systems are reported and obtained through crystal orientation in the membrane. A series of adsorption experiments are conducted in order to assist the selection of suitable probe molecules and evaluate the role of adsorption in the permeation process for the single-crystal membranes. Methane, n-butane, isobutane and nitrogen probe molecules are used to study intracrystalline sorption and transport effects for different crystal orientations, pressures and temperatures. Both pure gas selectivities and mixed gas separation factors are reported. A mixed gas separation factor of n-butane/isobutane = 116 for the 10-membered ring

orientation of the crystal at 383 K and a transmembrane pressure difference of 1.01 x 10^5 Pa is found using this technique. In addition, molecular sieving is observed for the 8-membered ring orientation of the crystal since methane, but not butane, transport is observed for this crystal orientation.

3.1 Introduction

Polycrystalline zeolite membranes have attracted much interest during the past decade on account of their potential for high separation selectivities and their thermal and chemical stability. This interest has been translated into remarkable developments and constant improvements in zeolite membrane preparation (Jansen and Coker, 1996). Despite these advances, a fundamental understanding of how the two fundamental measures of performance, permeance and selectivity, depend on the physical structure of the membrane has not been attained. The sieving layer of polycrystalline membranes is composed of randomly oriented individual crystallites leaving some void space between them. This void space is not necessarily connected, but any existing pathways spanning the thickness of the membrane will reduce the selectivity because they will most likely have larger diameters than the zeolitic pores. The intercrystalline contacts are quite irregular so that relating the permeance to the membrane thickness and the intrinsic crystal permeability is not a simple matter even in the absence of nonzeolitic pathways. The membrane selectivity, however, should be more closely related to the intrinsic crystal selectivity if the contribution of nonzeolitic pores and surface barriers can be neglected.

Provided the transport mechanisms remain the same for polycrystalline and single-crystal membranes, the intrinsic crystal selectivity sets an upper bound for the selectivity of multicrystalline membranes and shows to what extent this selectivity can be improved by eliminating nonzeolitic pores. Permeation measurements with single-crystals then

approximately define the maximum selectivity attainable with a multicrystalline membrane and, in addition, provide information about fundamental issues such as the role of crystal anisotropy, the contribution of different types of channels within a crystal, the permeability activation energy, etc. Here, we present a new method of preparing a single-crystal zeolite membrane and the hydrocarbon separation selectivities obtained from this system.

The use of single-crystal membranes for gas permeation studies was inaugurated by Wernick and Osterhuber who studied the diffusion of hydrocarbons in zeolite NaX (Wernick and Osterhuber, 1984) and by Paravar and Hayhurst who carried out similar studies for silicalite (Paravar and Hayhurst, 1984). This work established the usefulness of single-crystal membranes as a direct method for studying diffusion in zeolites. Other techniques, such as pulse field gradient NMR and uptake or chromatographic methods, are indirect and subject to various limitations (Kärger and Ruthven, 1992). In addition, these methods have generated diffusivity estimates differing by several orders of magnitude (Chen et al., 1994; Ruthven, 1995). Since the purpose of this work is to provide an upper bound for evaluating the properties of polycrystalline membranes, the membrane configuration and steady-state nature of the measurements is most appropriate.

Since much work on zeolite membranes involves ZSM-5 or silicalite, it is natural to pursue single-crystal measurements with the same zeolite. In fact, Shah and co-workers conducted such measurements for C_4 hydrocarbons across a single-crystal silicalite membrane (Shah et al., 1993). However, large silicalite crystals have the tendency for microtwinning along the b-axis (van Koningsveld, 1990) and as a result, it is very difficult to obtain true single-crystals in the crystallographic sense. The complicating effects of this twinning relative to the study of the transport of hydrocarbon molecules through single-crystal silicalite membranes has been discussed (Shah and Liou, 1994). As a result of this propensity towards twinning, it is impossible to precisely define the exact free diameters of the zeolite channels and orient the crystals to study exclusively diffusion in the straight or the sinusoidal channel systems. Thus, only average diffusivities are obtained from these

twinned silicalite crystal membranes (Paravar and Hayhurst, 1984) and the need for high quality, orientable single-crystal membranes remains.

Recently, an organothermal synthesis for high-silica ferrierite was developed that yields high quality, single-crystals with dimensions up to several hundred microns in size (Kuperman et al., 1993; Nadimi et al., 1995). Synthesis of this highly crystalline material has made possible detailed structure investigations (Weigel et al., 1996; Lewis et al., 1996). Based upon the single-crystal structure investigation and corresponding characterization studies (Lewis et al., 1996), the defect free nature of selected single-crystals and the precise dimensions of the channels were ascertained. As a result of the large crystal size, convenient morphology and exceptional crystal quality, these ferrierite crystals are ideal candidates for the construction of oriented single-crystal membranes.

Pure-silica ferrierite has a fully condensed framework structure containing a system of intersecting channels that are circumscribed by 10 and 8 silicon atoms (Meier and Olson, 1992). The topology of the ferrierite structure is shown in Figure 1. The 10 membered ring (MR) channels viewed along [100] are shown in Figure 1a while the 8MR channels viewed along [010] are shown in Figure 1b. The pores of ferrierite are not completely circular so three slightly different pore diameters for both the 10MR and 8MR channel systems are obtained from the structure solution Through construction of oriented single-crystal membranes and intelligent selection of probe molecule, it is possible for the first time to exploit these structural features of ferrierite and study exclusively diffusion through the 10MR channels (5.4 Å x 5.4 Å x 4.2 Å) *or* 8MR channels (4.6 Å x 3.7 Å x 3.0 Å).

3.2 Experimental Section

Crystal synthesis and calcination. The pure-silica ferrierite crystals were prepared using an organothermal technique (Kuperman et al., 1993). The precise preparation procedures

and corresponding characterization of the crystals used to construct the membranes have been reported previously (Lewis et al., 1996). The general morphology and channel orientation of the the crystals are shown in Figure 2. As is illustrated in Figure 2b, the 10MR channels run parallel to the short axis of the rectangular plate crystals while the 8MR channels run parallel to the longer axis of the rectangular plate. Thus, the only access to the micropore channel systems is via the pore mouths on the thin edges of the plate-shaped crystals. The large top and bottom sides of the plate-shaped crystals are nonporous faces composed of sheets of 5 MR's impervious to the probe molecules used in the adsorption and permeation experiments. A convenient feature resulting from these channel orientations relative to the crystal morphology is the fact that either the 10MR or the 8MR channels may be selectively chosen for study in a given single-crystal membrane.

A critical step in the preparation of the ferrierite crystals for use in membranes is the removal of the organic structure-directing agent from the as-synthesized crystals to free intracrystalline pore space for adsorption and transport. The calcination of large tetrapropylammonium containing silicalite crystals and the effects of calcination on the crystal's inorganic framework have been studied previously (Geus et al., 1994). The development of cracks in large crystal silicalite calcined in air has been documented (Geus and van Bekkum, 1995). As suggested from the silicalite calcination studies, initial attempts to calcine the large ferrierite crystals using conventional methods of heating in air led to severe cracking of the crystals and incomplete removal of the organic that make the crystals unsuitable for use as single-crystal membranes. The organic-free ferrierite was obtained by careful calcination of the as-synthesized material under controlled conditions to avoid damaging the single-crystals. The calcination process was performed in a temperature-controlled tube furnace equipped with a valve-regulated T-shaped gas inlet connected to nitrogen and air gas cylinders. The following heating program in a controlled atmosphere yielded clear, colorless, organic-free crystals without any obvious cracking as observed by optical and scanning electron microscopy: heat in N_2 from 298 K to 973 K at

1.25 K/min, hold isothermal at 973 K for 10 hours in N_2, heat in air from 973 K to 1173 K at 0.83 K/min, finally hold isothermal in air at 1173 K for 24 hours. By initially heating the crystals in an inert atmosphere, the organic structure-directing agent decomposes in an endothermic manner leaving coke deposits. If the calcination is stopped at this point, the color of the crystals (originally clear) is opaque black. Switching the calcination atmosphere from nitrogen to air allows complete oxidation and removal of the decomposed organics as gases at the elevated temperatures of calcination. The separation of the decomposition and oxidation steps during calcination creates a more controlled process for removal of the organic structure-directing agents that avoids damaging the crystals.

Scanning electron microscopy (SEM). SEM images were recorded on a Camscan 2-LV scanning electron microscope using an acceleration voltage of 15 kV.

Adsorption. Nitrogen adsorption isotherms were collected on a Omnisorp 100 analyzer at 77 K with a sample weight (W) to flow rate (F) ratio of W / F = 0.67 g·min / cm^3 at STP (standard temperature and pressure). Hydrocarbon adsorption isotherms were recorded on a McBain-Bakr balance using a quartz spring and optical sighter to observe the degreee of extension of the quartz spring. All ferrierite crystals used for adsorption (both nitrogen and hydrocarbon) were ground to micron sized particles as determined by SEM. The reason for grinding is to remove diffusional constraints during the adsorption experiments in order to quickly obtain equilibrium adsorption isotherms. The adsorbate uptakes are reported in cm^3 of condensed liquid probe molecule per gram of ferrierite. Liquid densities used to calculate adsorption uptakes, as well as saturation pressures (P_0) of the probe molecules for all temperatures used in the permeation experiments are reported in Table 1. These values were obtained from tables and correlations found in the CRC Handbook (Weast et al., 1986) and Gas Processors Suppliers Association Engineering Data Book (GPSA, 1987).

Membrane Construction. The sequence of steps used to fabricate the oriented single-crystal ferrierite membranes is shown in Figure 3. All single-crystal membranes were constructed under an optical microscope due to the delicate nature of precisely orienting and

positioning the crystal. The first step is to apply a thin line of Torr Seal epoxy (Varian Vacuum Products) on the edge of a glass microscope cover slip (Fischer Scientific). While holding the prepared glass slip vertically under the optical microscope, a calcined ferrierite crystal is selected and carefully positioned on the thin line of epoxy using a metal probe with a very fine tip. At this point, the channel system and pore size of the single-crystal membrane is determined as either 10MR or 8MR depending on crystal orientation. This intermediate point in the membrane construction is shown in Figure 3a. Next, the half-constructed membrane is placed in a guide constructed of glass microscope slides. A thin line of Torr Seal epoxy is placed on the edge of a second glass cover slip. Again under the microscope, the second prepared glass slip is inserted into the tracks of the guide and slowly slid up to the first glass slip and crystal. At this point, the oriented, single-crystal of ferrierite is sandwiched between the two glass cover slips and embedded in epoxy in all places except for the two exposed edges (front and back) of the crystal as shown in Figure 3b. The thin line feature in the center of the SEM micrograph is the protruding edge of the ferrierite crystal. The rough surfaced region surrounding the crystal is the epoxy and the smooth surfaces on either side of the epoxy are the glass cover slips. The membrane is left in the guide to maintain proper positioning and alignment of the crystal and glass cover slips as the epoxy is allowed to cure at room temperature for 24 hours. At this point the membrane is removed from the guide and two 15 cm lengths of glass tubing are attached perpendicular to either side of the membrane using epoxy as shown in the cross-sectional view of Figure 4. These attached segments of glass tubing are used to connect the membrane to the permeation apparatus using Ultra-Torr fittings. A control experiment was also conducted by constructing the device without a crystal. No hydrocarbon flux was observed for this control membrane as detected by gas chromotography (*vide infra*), thus demonstrating the tight seal provided by the epoxy.

Permeation measurements. The experimental apparatus and sampling procedure used for measuring hydrocarbon flux through the oriented single-crystal ferrierite membranes is

shown in Figure 5. The hydrocarbon flux through zeolite membranes is commonly measured either by the pressure rise technique using sensitive pressure transducers or by the steady-state technique of flowing a feed gas from one side of the membrane and a carrieir gas from the other side. Initial attempts in this study to use the pressure rise technique failed because the cross-sectional area of the ferrierite crystal in the membrane available for permeation is too small for the flux to be measured with reasonable accuracy. Subsequently, the steady-state technique was applied collecting the hydrocarbon permeate in a sampling loop constructed of 1/16 inch stainless steel tubing and submerged in a liquid nitrogen bath as shown in Figure 5a. By injecting known quantities of hydrocarbons into the apparatus, it was verified that the hydrocarbon permeate is quantitatively trapped as it passes through the chilled sampling loop. Permeate can be collected over a sufficiently long period of time (typically 15 minutes to 10 hours) to obtain adequate sample for gas chromatographic determination. To insure that the sampling loop did not become plugged with condensate during the sample collection period, the sample collection time was doubled to make sure the amount of collected hydrocarbon detected also doubled before finalizing the measurement conditions. This test verifies that the pressure on the permeate side of the crystal remains approximately zero and a constant membrane pressure differential, i.e., driving force, is maintained throughout the permeate collection period.

After collecting permeate for a given length of time, the sample loop is isolated from the rest of the system by closing the four-way valve and removing the sample loop from the liquid nitrogen bath as shown in Figure 5b. The collected permeate is allowed to warm to room temperature and then swept into the gas chromatograph (GC) with helium by adjusting the four and six way values as shown in Figure 5c. The amount of hydrocarbon collected during the sampling phase of the permeation experiment is measured using a Hewlett Packard 5890 Series II GC equipped with a flame ionization detector (FID). An Alltech chromatographic column packed with 0.17% picric acid on Graphpac and GC responses were recorded on a Hewlett Packard 3394A integrator. The gas chromatograph

was calibrated using a calibration gas mixture of n-butane and isobutane, 1025 ppm and 985 ppm respectively, in nitrogen from Matheson Gas Products, Inc. The FID responses for methane were quantified using sensitivity factors relative to the calibrated butane responses (Dietz, 1967). At the conclusion of a permeation experiment, the cross-sectional area of the embedded crystal available for gas flux was measured by SEM. With the amount of hydrocarbon collected, collection time, crystal cross-sectional area and feed pressure known, calculation of flux and permeance was carried out. For all the measurements, the partial pressure of the hydrocarbon at the permeate side could be neglected for the purpose of calculating the transmembrane pressure difference.

3.3 Results and Discussion

A series of physical adsorption experiments were conducted in order to assist in the selection of suitable probe molecules. The adsorption capacities listed in Table 2 are measured at temperatures (T) and pressures (P) chosen to allow for maximum possible saturation of the micropores in ferrierite and test size-exclusion of particular probe molecules based on uptakes. The void volumes calculated from the nitrogen and methane uptakes are 0.12 cm^3/g and 0.11 cm^3/g respectively, which compare well with the void volume of 0.12 cm^3/g calculated from the crystal structure (Lewis et al., 1996). The void volume found by methane adsorption is slightly lower than the theoretical value and is likely due to incomplete filling of the micropores that results from the steric limitations in packing methane in the channels. Equilibrium adsorption uptakes for n-butane and isobutane indicate an adsorption capacity of 0.04 cm^3/g. Figure 1a shows that there are two 10MR channels per unit cell (unit cells denoted by rectangular boxes) Assuming that the void space resulting from the 10MR channels in one unit cell can be represented as two

cylinders of diameter 5 Å and length 7.43 Å (a axis length of ferrierite unit cell, Lewis et al., 1996), a volume of 0.04 cm^3/g is calculated. Thus, based on the adsorption data, nitrogen and methane molecules are able to access both the 8MR and 10MR channel systems, while the n-butane and isobutane are only able to access the 10MR channel system (are size-excluded from the 8MR channel system).

Adsorption isotherms describe uptake of the adsorbate gas as a function of relative pressure, P/P_o, at a fixed temperature. However, permeation experiments are conducted at a particular temperature and feed pressure which defines a discrete point on the adsorption isotherm. Thus, temperature and feed pressure of a permeation experiment determine whether or not the micropores are filled with condensed probe molecules, at least near the feed side of the membrane. This is demonstrated by the data given in Figure 6 which shows adsorption isotherms measured for n-butane and isobutane at T = 383 K. The final datum point on each isotherm is at a pressure of 1.01 x 10^5 Pa, but the final relative pressures are different due to the different saturation pressures, P_o, for the two probe molecules as listed in Table 1. As can be seen from the data given in Figure 6, a single-crystal ferrierite membrane in the 10MR orientation at T = 383 K and a pressure of 1.01 x 10^5 Pa on the feed side of the membrane with n-butane as the probe molecule is operating under conditions where the n-butane would saturate the 10MR channel system. However, this saturation would not extend across the entire width of the membrane due to the fact that the pressure drops to zero at the permeate side. On the other hand, a membrane operating at the same temperature and feed pressure with isobutane as the probe molecule does not reach saturation anywhere in the crystal. Thus, even though these two experiments are conducted with the same crystal orientation, temperature and pressure, the results are obtained at two different regimes on the isotherm. In the case of n-butane, transport in certain regions of the crystal would proceed under conditions close to saturation. However, in the case of isobutane, transport would take place under conditions removed from

saturation. In summary, different transport mechanisms can be occurring depending on temperature, pressure, probe molecule and pore size.

Based on data from the adsorption experiments, a set of temperatures (323 K, 383 K and 398 K) and feed membrane pressures (1.01×10^5 Pa and 2.02×10^5 Pa) were selected for permeation experiments. The upper temperature limit is set by the thermal stability of the epoxy used to seal the ferrierite crystals. Due to the thin line of epoxy used to construct the single-crystal membranes, leaks resulting from the thermal degradation of the epoxy occur after extended membrane operation at temperatures in excess of 403 K. The equilibrium hydrocarbon adsorption uptakes at the temperature and pressure selected for the permeation experiments are listed in Table 3. None of the methane permeation experiments are conducted near adsorption saturation conditions. In contrast, all of the n-butane permeation experiments are conducted at temperatures and feed pressures where n-butane saturation of the 10MR channels is possible. For the isobutane permeation experiments, only the measurements conducted at T = 323 K and $\Delta P = 2.02 \times 10^5$ Pa have the potential to yield isobutane saturation of the 10MR channels.

The single gas, steady-state permeation results for the single-crystal ferrierite membranes as a function of crystal orientation, temperature, feed pressure and probe molecules are reported in Table 4. Several interesting trends are observed in this data. For methane transport in the 8MR membrane configuration, the flux increases only slightly with temperature over the range of temperatures investigated and increases almost linearly with feed pressure from 1.01×10^5 Pa to 2.02×10^5. Based on the measured equilibrium adsorption capacity, methane is able to access both the 8MR and 10MR ring channels. Therefore, in the 8MR crystal orientation experiments, methane can enter the 10MR channels after entering the crystal since the two channel systems intersect. However, since there is no pressure gradient in the 10MR direction, the 10MR channels do not contribute to the measured fluxes. The relative pressures of methane for all the 8MR/methane permeation

experiments shown in Table 4 are sufficiently low so that the entire thickness of the membrane is far from saturation and most likely in the Henry's Law regime (resulting in the observed linear pressure dependence). No detectable n-butane or isobutane permeance is observed through the 8MR oriented FER crystals indicating that the n-butane and isobutane are size-excluded from the 8MR membranes in agreement with the equilibrium adsorption capacities listed in Table 2. This result is also the hallmark signature of zeolite molecular sieving and confirms the absence of cracks and pinholes in the single-crystal or sealing epoxy.

A much higher methane flux is observed in the 10MR oriented crystals relative to the 8MR flux at all selected temperatures and pressures as would be expected from the larger free diameters of the 10MR channels. The methane permeances through the 10MR channels show a sharp increase with temperature from 41.1 x 10^{-12} mol/(m^2·s·Pa) at T = 323 K to 186 x 10^{-12} mol/(m^2·s·Pa) at T = 398 K, both at feed pressures of 1.01 x 10^{-5} Pa. This strong temperature dependence is not observed for methane in the 8MR channels where the permeance increased only slightly from 2.04 x 10^{-12} mol/(m^2·s·Pa) to 2.25 x 10^{-12} mol/(m^2·s·Pa) over the same temperature range. The differences in methane permeance between the 8MR and 10MR orientations originate from the smaller free diameter of the 8MR (4.6 Å x 3.7 Å x 3.0 Å) versus the 10MR (5.4 Å x 5.4 Å x 4.2 Å).

All of the n-butane permeation experiments are conducted at temperatures and feed pressures capable of inducing near saturation of n-butane in a portion of the 10MR channels. Similar to the methane in the 10MR channels, the n-butane also exhibits a sharp increase in permeance with increasing temperature. The flux increases slightly more than linearly with increasing feed pressure.

Table 4 shows the transport of isobutane through the 10MR oriented single-crystal membranes to be much slower than that of any of the other probe molecules for this crystal orientation. The reported isobutane kinetic diameter of 5.0 Å (Breck, 1974) is very close in

size to the pore dimensions of 5.4 Å x 5.4 Å x 4.4 Å of the 10MR channel (Lewis et al., 1996). Therefore, isobutane has low mobility and the approach to adsorption equilibrium requires several hours. In contrast, equilibrium uptake is reached within minutes for all other probe molecules. A similar trend is observed in the single-crystal permeation experiments. Steady-state permeation rates are obtained on a time scale of minutes for all gases except isobutane which requires several hours. Changes in temperature over the range investigated produced only minor changes in the isobutane permeance. However, the isobutane fluxes increase linearly with pressure with one exception. For all experimental parameter sets except one, i.e., T = 323 K and P = 2.02 x 10^5 Pa as shown in Table 3, the membrane is operating under conditions where isobutane is unable to condense in the crystal. At the particular T and P mentioned, condensation may occur and the highest isobutane permeance is observed at these conditions. This would indicate that intracrystalline transport of the isobutane is fastest when its density in the 10MR channels is greatest.

The results of the mixed gas (45% n-butane and 55% isobutane) permeation experiments are reported in Table 5. In general, the mixed gas permeances are lower than the single gas permeances; however, high n-butane/isobutane selectivities are maintained. It appears that the n-butane preferentially adsorbs into the crystal over the isobutane consistent with the adsorption uptakes reported in Table 3 and the adsorption kinetics mentioned previously. The presence of small amounts of isobutane in the 10MR channels at these temperatures and pressures does not markedly retard the transport of n-butane through the crystals. This is encouraging in that it demonstrates that high separation selectivities are possible even with mixed gas feeds. It is interesting to note that the lowest n-butane/isobutane (n/i) selectivity is obtained at T = 323 K and P = 2.02 x 10^5 Pa where isobutane condensation in the 10MR channels is possible.

The objective of this work is to construct well defined 8- and 10-membered ring (MR) single-crystal membranes with the intent of establishing experimental upper limits for

separation factors obtainable in polycrystalline zeolite membranes of similar pore dimensions. To date, there has been one report of a polycrystalline ferrierite membrane (Matsukata et al., 1994). Direct comparison of the single-crystal ferrierite data with the polycrystalline ferrierite data is not possible due to the different gases and temperatures used in the permeation experiments. However, data at comparable conditions for polycrystalline ZSM-5 membranes is available. The ZSM-5 structure is composed of intersecting 10MR channels of slightly larger dimensions (5.3 Å x 5.6 Å and 5.1 Å x 5.5 Å) (Meier and Olson, 1992), so comparison to the 10MR single-crystal results is possible. At T = 381 K, a n-butane/isobutane selectivity of 39.4 is reported from single gas permeation measurements from a polycrystalline ZSM-5 membrane (Yan et al., 1996). This compares to a single gas n/i selectivity of 124 from the single-crystal ferrierite membrane experiments conducted at T = 383 K and a membrane pressure differential of 1.01×10^5 Pa.

The high permeances and selectivities shown in Tables 4 and 5 are reproducible only when using fresh single-crystal membranes. For example, after measurement of isobutane permeance, a membrane becomes impermeable to other gases due to the plugging of the micropores by adsorbed isobutane that does not appear to completely desorb even after heating the crystal at 398 K under vacuum for one week. The epoxy component of the single-crystal membrane prevents reactivating the membrane at higher temperatures. Attempts to use plugged membranes for permeation experiments with different probe molecules result in the measurement of the slow desorption of the original probe from the crystal while no flux of the second probe molecule is detected. The second probe molecule evidently is completely blocked by the isobutane molecules in the 10MR channels. This result is not suprising given the size of probe molecules used and the dimensions of the 10MR channels. Even for single-crystal membranes exposed to methane, which apparently desorbs quickly and completely as detected by GC, marked reductions in permeances for other probe molecules were observed. This hysteresis effect for single-crystal membranes

highlights the effect of exposure to different probe molecules on the membrane's performance and selectivity and the importance of adequate membrane activation.

3.4 Conclusions

A technique for constructing leak-free, single-crystal ferrierite membranes is presented. By properly orienting the crystal in a membrane configuration, transport through either the 8 or 10MR channel system may be studied. The 8MR channels admit methane but not n-butane or isobutane, while the 10MR channels admit methane, n-butane and isobutane. Permeation experiments conducted with a mixed gas feed (45% n-butane and 55% isobutane) show maintenance of high n/i selectivities comparable to the selectivities observed from the single gas experiments. Additionally, the measured fluxes and separation factors are shown to depend on the exposure history of the crystal to different probe molecules.

Acknowledgments

Financial support for this work was provided by the National Science Foundation (Grant No. CTS-9114829). The authors also wish to acknowledge helpful discussions with Yushan Yan.

Literature Cited

Breck, D. W., *Zeolite Molecular Sieves*, Krieger, Malabar, Florida, p. 636 (1974).

Chen, N. Y., T. F. Degnan, Jr. and C. M. Smith, *Molecular Transport and Reaction in Zeolites*, VCH, New York, pp. 131 (1994).

Dietz, W. A., "Response Factors for Gas Chromatographic Analyses," *J. Gas Chromatography*, **5**, 68 (1967).

Gas Processors Suppliers Association (GPSA), *Engineering Data Book*, GPSA, Tulsa, Oklahoma, p 23-1 (1987).

Gues, E. R., J. C. Jansen and H. van Bekkum, "Calcination of Large MFI-type Single Crystals: Part 1. Evidence for the Occurrence of Consecutive Growth Forms and Possible Diffusion Barriers Arising Thereof," *Zeolites*, **14**, 82 (1994).

Gues, E. R. and H. van Bekkum, "Calcination of Large MFI-type Single Crystals, Part 2: Crack Formation and Thermomechanical Properties in View of the Preparation of Zeolite Membranes," *Zeolites*, **15**, 333 (1995).

Jansen, K. C. and E. N. Coker, "Zeolitic Membranes," *Current Opinions in Solid State & Materials Science*, **1**, 65 (1996).

Kärger, J. and D. M. Ruthven, *Diffusion in Zeolites*, Wiley, New York, p. 207 (1992).

Kuperman, A., S. Nadimi, S. Oliver, G. A. Ozin, J. M. Garcés and M. M. Olken, "Non-aqueous Synthesis of Giant Crystals of Zeolites and Molecular Sieves," *Nature*, **365**, 239 (1993).

Lewis, Jr., J. E., C. C. Freyhardt, and M. E. Davis, "Location of Pyridine Guest Molecules in an Electroneutral $\{^3_\infty\}[SiO_{4/2}]$ Host Framework: Single Crystal Structures of the As-synthesized and Calcined Forms of High-silica Ferrierite," *J. Phys. Chem.*, **1996**, 5039 (1996).

Matsukata, M., N. Nishiyama and K. Ueyama, "Preparation of a Thin Zeolitic Membrane," *Studies in Surface Science and Catalysis*, J. Weitkamp, H. G. Karge, H. Pfeifer and W. Hölderich, eds., Elsevier, Amsterdam, **84**, p. 1183 (1995).

Meier, W. M. and D. H. Olson, *Atlas of Zeolite Structure Types*, Butterworth-Heinemann, Boston, p.138 (1992).

Nadimi, S., S. Oliver, A. Kuperman, A. Lough, G. A. Ozin, J. M. Garcés, M. M. Olken and P. Rudolf, "Nonaqueous Synthesis of Large Zeolite and Molecular Sieve Crystals," *Proceedings of the 10th International Zeolite Conference*, H. G. Karge, H. Pfeifer and W. Hölderich, eds., Elsevier, Amsterdam, **84**, p. 93 (1995).

Paravar, A. R. and D. T. Hayhurst, "Direct Measurement of Diffusivity for Butane Across a Single Large Silicalite Crystal," *Proceedings of the 6th International Zeolite Conference*, D. Olson and A. Bisio, eds., Butterworths, New York, p. 217 (1984).

Ruthven, D. M., "Diffusion in Zeolites," *Zeolites: A Refined Tool for Designing Catalytic Sites*, L. Bonneviot and S. Kaliaguine, eds., Elsevier, Amsterdam, p. 223 (1995).

Shah, D. B., S. Chokchal-acha and D. T. Hayhurst, "Measurements of Transport Rates of C_4 Hydrocarbons across a Single-Crystal Silicalite Membrane," *J. Chem Soc. Faraday Trans.*, **89**(16), 3161 (1993).

Shah, D. B. and H. Y. Liou, "Diffusion of Aromatics Through a Silicalite Membrane," *Zeolites and Related Microporous Materials: State of the Art 1994*, J. Weitkamp, H. G. Karge, H. Pfeifer and W. Hölderich, eds., Elsevier, Amsterdam, **84**, p. 1347 (1994).

van Koningsveld, H., J. C. Jensen and H. van Bekkum, "The Monoclinic Framework Structure of Zeolite H-ZSM-5. Comparison with the Orthorhombic Framework of As-synthesized ZSM-5," *Zeolites*, **10**, 235 (1990).

Weast, R. C., M. J. Astle and W. H. Beyer, *CRC Handbook of Chemistry and Physics*, CRC, Boca Raton, FL (1986).

Weigel, S. J., J. C. Gabriel, E. G. Puebla, A. M. Bravo, N. J. Henson, L. M. Bull and A. K. Cheetham.

Wernick, D. L. and E. J. Osterhuber, "Diffusional Transition in Zeolite NaX: 1. Single Crystal Gas Permeation Studies," *Proceedings of the 6th International Zeolite Conference*, D. Olson and A. Bislo, eds., Butterworths, New York, p. 22 (1984).

Yan, Y., M. E. Davis and G. R. Gavalas, "Preparation of Highly Selective Zeolite ZSM-5 Membranes by a Post-synthetic Coking Treatment," submitted to *J. Membr. Sci.* (1996).

Table 3.1 Physical properties for probe molecules with saturation pressures (P_o) at temperatures selected for permeation experiments. All values obtained from data and correlations given in the CRC Handbook (Weast et al., 1986); except for methane (in parentheses) which was estimated from data provided in the GPSA Engineering Data Book (GPSA, 1987).

Physical Property and Condition	Nitrogen	Methane	n-Butane	Isobutane
Mol. Weight [g/mol]	28.0	16.04	58.12	58.12
Boiling Point [K]	77	111	272.5	271.4
Liquid Density [g/cm^3]	0.808	0.424	0.601	0.549
P_o(T = 323 K) [x 10^{-5} Pa]		(348)	5.05	6.46
P_o(T = 383 K) [x 10^{-5} Pa]		(500)	17.2	23.2
P_o(T = 398 K) [x 10^{-5} Pa]		(600)	21.2	25.3

Table 3.2 Equilibrium adsorption capacity of probe molecules in pure-silica ferrierite crystals ground to micron size.

	Nitrogen	Methane	n-Butane	Isobutane
Equilibrium Adsorption Capacity [cm^3/g FER]	0.13	0.11	0.04	0.04
Isotherm Temperature [K]	77	77	298	261
P_o [x 10^{-5} Pa]	1.01	0.02	2.69	1.00
Relative Pressure (P/P_o)	0.4	0.4	0.4	0.6

Table 3.3 Equilibrium adsorption uptakes reported in [cm^3 condensed adsorbate/g FER] for hydrocarbon probe molecules in pure-silica ferrierite at pressures and temperatures corresponding to conditions selected for single-crystal membrane permeation experiments. Values listed in parentheses indicate relative pressure (P/P_o) at the feed side of single-crystal membrane.

Temperature and Feed Pressure	Methane	n-Butane	Isobutane
323 K, 1.01 x 10^5 Pa	0.00 (0.003)	0.04 (0.20)	0.00 (0.16)
323 K, 2.02 x 10^5 Pa	0.00 (0.006)	0.04 (0.40)	0.04 (0.32)
383 K, 1.01 x 10^5 Pa	0.00 (0.002)	0.04 (0.059)	0.00 (0.044)
383 K, 2.02 x 10^5 Pa	0.00 (0.003)	0.04 (0.12)	0.00 (0.088)
398 K, 1.01 x 10^5 Pa	0.00 (0.002)	0.04 (0.05)	0.00 (0.04)
398 K, 2.02 x 10^5 Pa	0.00 (0.004)	0.04 (0.10)	0.00 (0.08)

Table 3.4 Single gas steady-state permeation values for single-crystal ferrierite membranes as a function of crystal orientation, temperature, pressure and probe molecule.

Crystal Orientation*	Temperature [K]	Feed Pressure [x10^{-5} Pa]	Probe Molecule	Permeance (x 10^{-12}) [mol/(m^2·s·Pa)]
8	323	1.01	methane	2.04
8	323	2.02	methane	2.05
8	383	1.01	methane	2.12
8	383	2.02	methane	2.18
8	398	1.01	methane	2.25
8	398	2.02	methane	2.89
10	323	1.01	methane	41.1
10	323	2.02	methane	45.3
10	383	1.01	methane	152
10	383	2.02	methane	158
10	398	1.01	methane	186
10	398	2.02	methane	197
10	323	1.01	n-butane	25.3
10	323	2.02	n-butane	27.8
10	383	1.01	n-butane	105
10	383	2.02	n-butane	125
10	398	1.01	n-butane	163
10	398	2.02	n-butane	172
10	323	1.01	isobutane	0.83
10	323	2.02	isobutane	2.03
10	383	1.01	isobutane	0.85
10	383	2.02	isobutane	0.96
10	398	1.01	isobutane	1.07
10	398	2.02	isobutane	1.11

* Average cross-sectional areas: 8MR orientation = 9.63(7) x 10^{-9} m^2, 10MR orientation = 1.18(9) x 10^{-8} m^2; Average number of pore openings: 8MR orientation = 1.39(8) x 10^{10}, 10MR orientation = 8.95(2) x 10^9; Average diffusion pathlengths: 8MR orientation = 6.20(9) x 10^{-4} m, 10MR orientation = 5.07(3) x 10^{-4} m.

Table 3.5 Mixed gas (45% n-butane and 55% isobutane) steady-state permeation values for single-crystal ferrierite membranes as a function of temperature, pressure and probe molecule.

Crystal Orientation	Temperature [K]	Pressure Differential [x10^{-5} Pa]	Probe Molecule	Permeance (x 10^{-12}) [mol/(m^2·s·Pa)]	n/i Separation Factor
10	323	1.01	n-butane isobutane	23.5 0.40	59
10	323	2.02	n-butane isobutane	23.7 0.43	55
10	383	1.01	n-butane isobutane	98.2 0.85	116
10	383	2.02	n-butane isobutane	102.0 0.86	119

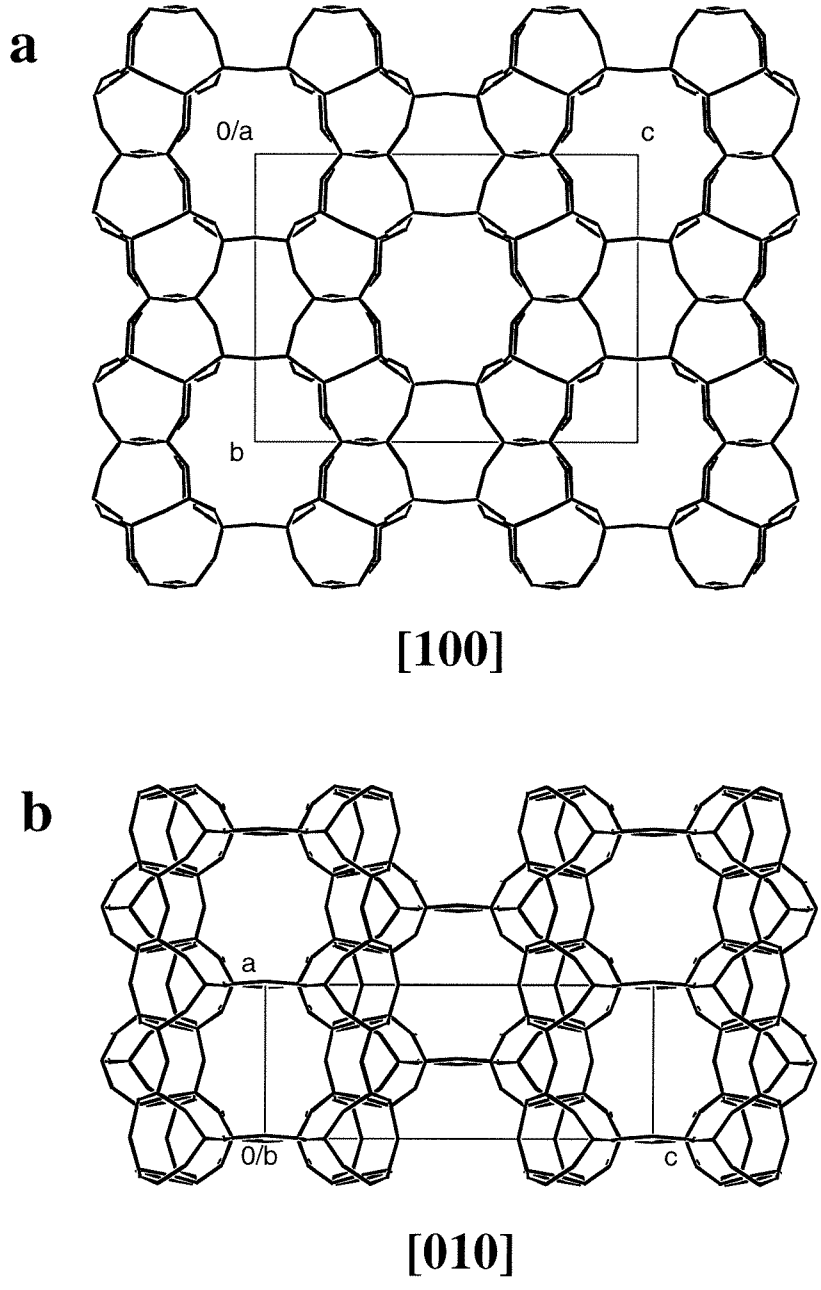

Figure 3.1 Details of the ferrierite crystal structure showing (a) 10MR channels viewed down [100] and (b) the 8MR channels viewed down the [010] axis. Unit cells denoted by rectangular boxes.

a

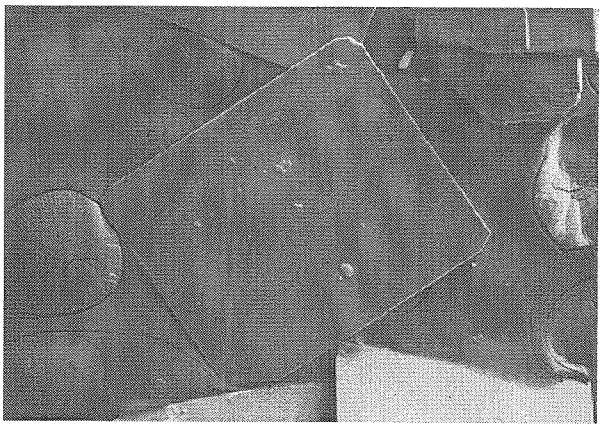

b

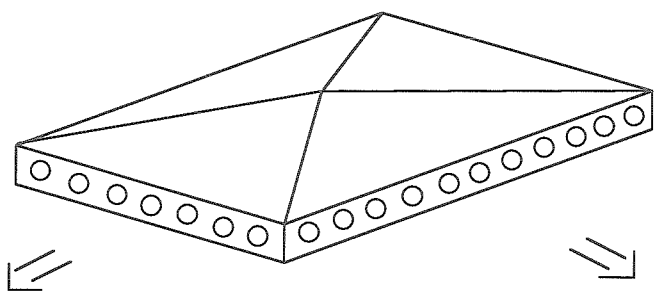

Figure 3.2 (a) SEM micrograph showing general crystal morphology and (b) channel orientation relative to overall crystal morphology.

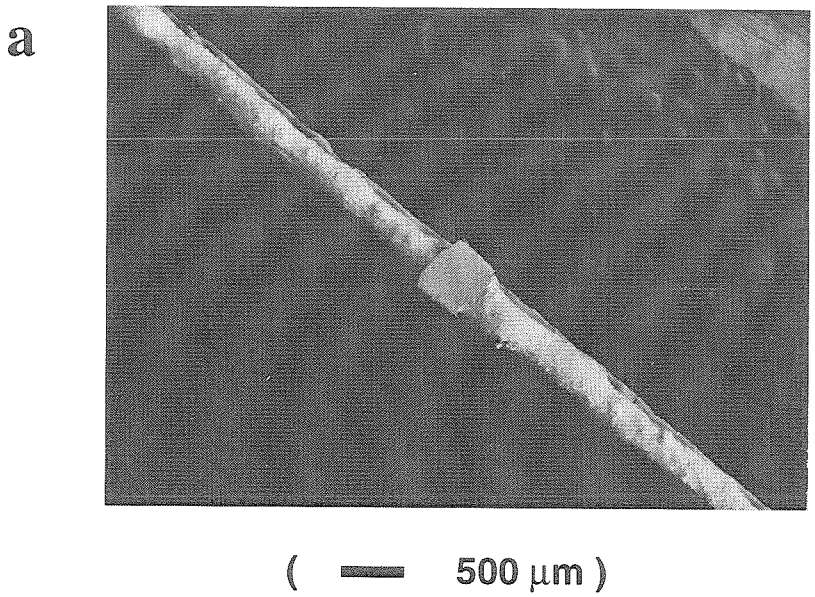

Figure 3.3 The sequence of steps used to fabricate the oriented single-crystal ferrierite membranes. (a) Half-completed membrane showing crystal in 8-membered ring orientation and (b) completed membrane showing protruding crystal edge embedded in epoxy and sandwiched between two glass cover slips.

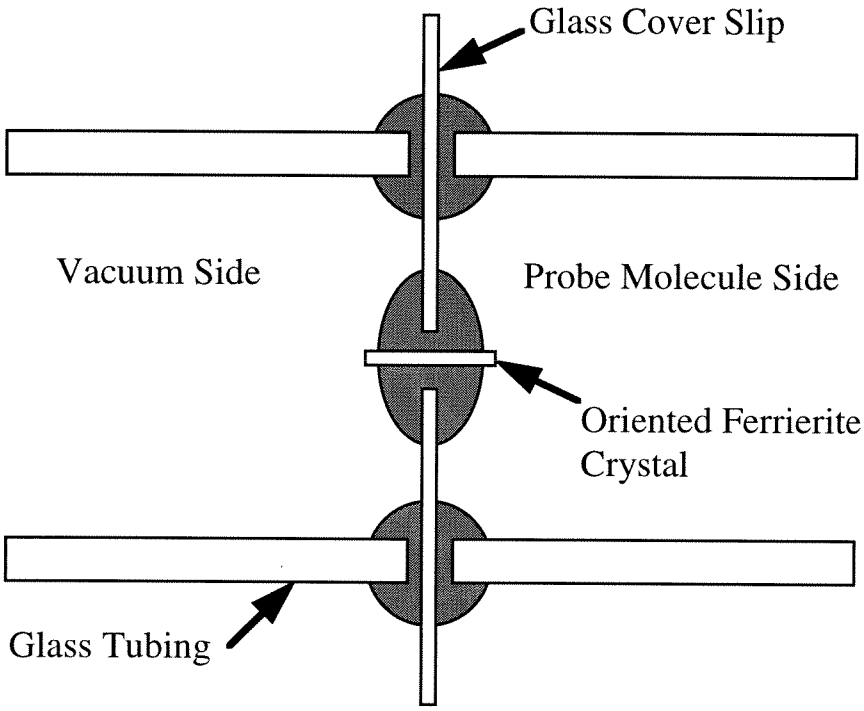

Figure 3.4 Schematic of attachment of glass tubing segments for incorporation of membrane into permeation measurement apparatus. Shaded regions indicate junctions between glass tubing, glass coverslips and crystal sealed with epoxy.

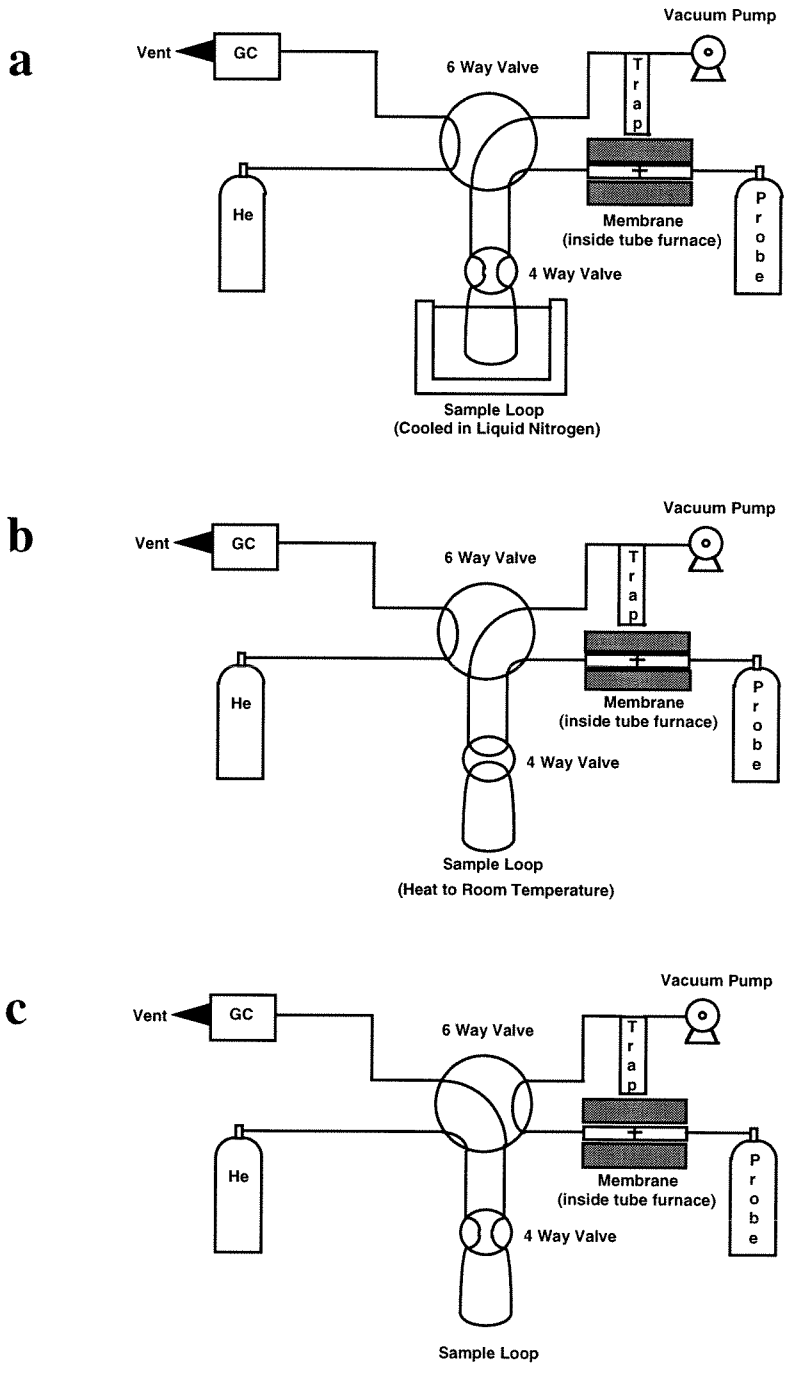

Figure 3.5 The permeation measurement apparatus and sampling procedure used for measuring hydrocarbon flux: (a) collecting sample (b) heating sample (c) analyzing sample.

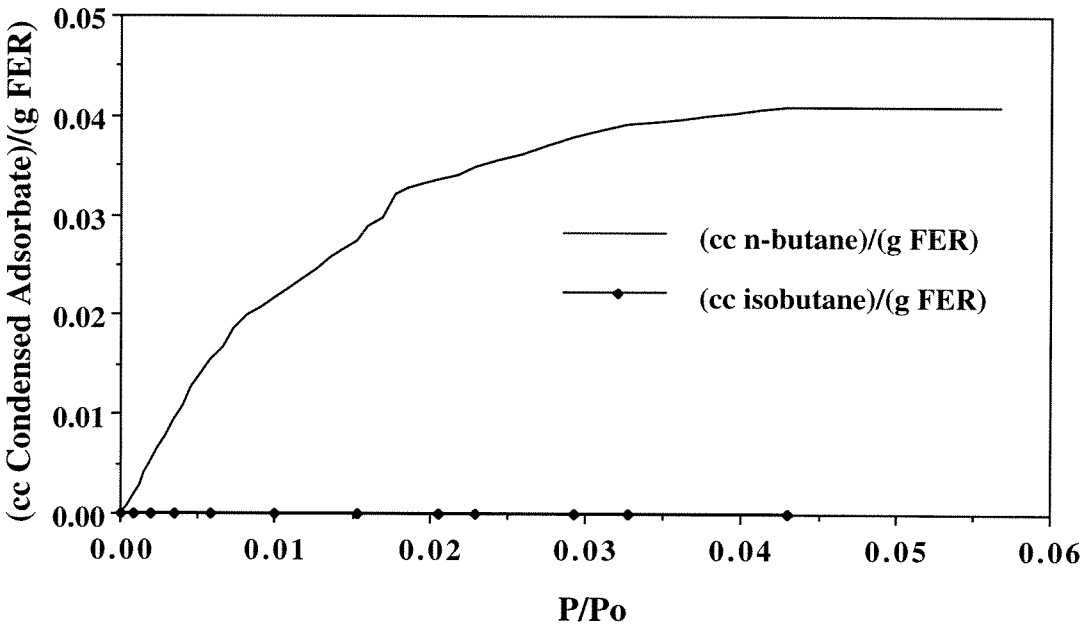

Figure 3.6 Adsorption isotherms of n-butane and isobutane collected at T = 383 K. The final datum point on each of the isotherms represents a relative pressure corresponding to P = 1.01 x 10^5 Pa.

Chapter 4

Conclusions and Future Directions

4.1 Conclusions

In this work, high-quality single-crystals of pure-silica ferrierite are synthesized under organothermal conditions. The organic species in the channels of the as-synthesized ferrierite can be completely removed by calcination in a controlled atmosphere furnace using appropriate heating rates. This calcination procedure avoids damaging the inorganic framework, as occurs with conventional calcination procedures, and produces organic-free ferrierite crystals suitable for single-crystal structure studies and membranes.

Detailed characterization and structure investigations are performed on both the as-synthesized and calcined crystals. Comparison of the as-synthesized and calcined crystal structures demonstrates that even weak interactions between the inorganic host framework and enclathrated organic species can cause measurable distortion of the silica network. This distortion is reflected in the different T-O bond lengths and T-O-T bond angles in the framework of the as-synthesized and calcined forms of Si-FER. Taking into account both of these bond parameters, a new correlation between the geometric structure data and spectroscopic data from the ^{29}Si NMR chemical shifts is obtained. The single-crystal structure of the calcined material defines a defect and fault free system of intersecting 8- and 10-membered ring channels suitable for studying intracrystalline transport.

A convenient feature of these crystals is the channel orientations relative to the crystal morphology allowing individual calcined ferrierite crystals to be mounted in a membrane configuration so that only the 10-membered ring channels (5.4 Å x 5.4 Å x 4.2 Å) or the 8-membered ring channels (4.6 Å x 3.7 Å x 3.0 Å) are accessible for gas molecule permeation. This marks the first reported example of exclusive transport through 8- or 10-membered ring channels obtained from membrane measurements.

Both single gas and mixed gas permeation rates at temperatures ranging from 323 K to 398 K and feed pressures ranging from 1.01 x 10^5 Pa to 2.02 x 10^5 Pa are reported. Permeation experiments conducted with a mixed gas feed (45% n-butane and 55%

isobutane) show maintenance of high n/i selectivities, i.e., approximately two orders of magnitude, comparable to the selectivities observed from single gas experiments at the same conditions. The maintenance of high n/i selectivities for the mixed gas permeation experiments is encouraging since it demonstrates that small amounts of isobutane in the 10MR channels do not stop the transport of n-butane through the crystal.

The obtainable flux and selectivity of a single-crystal membrane is dependent on the crystal's history of exposure to other probe molecules. This hysteresis effect for single-crystal membranes highlights the importance of adequate membrane activation and using freshly calcined crystals to obtain reproducible permeation results. The use of crystal membranes in permeation experiments previously contacted with other probe molecules results in reduced fluxes and lowered separation selectivities. These observations most likely result from blockage of some of the crystal pores by physisorbed previously used probe molecules. One limitation of this system is the inability to reactivate a single-crystal membrane after use due to the temperature constraints imposed by the epoxy used in the membrane construction.

The influence of physical adsorption on the permeation process is also studied in this work. A series of adsorption experiments is conducted to evaluate the possibility of probe molecule saturation of the ferrierite micropores. N-butane saturation of the 10MR channels is possible in all the permeation experiments. However, methane or isobutane saturation of the crystal is not possible at these experimental conditions (except the isobutane experiments conducted at T = 323 K and P = 2.22 x 10^{-5} Pa). Thus, due to differences in micropore saturation, different transport mechanisms can be occurring depending on temperature, pressure, probe molecule and pore size.

The physical adsorption experiments also test size-exclusion of particular probe molecules based on uptakes. Exclusion of n-butane and isobutane, but not methane, from the 8MR channel is observed in both the uptake measurements and permeation measurements. This molecular sieving action is a signature of zeolites resulting from their

regular and precise pore diameters. In addition, the lack of detectable butane molecule permeation through the 8MR oriented membrane indicates the absence of nonzeolitic transport pathways through the membrane.

In conclusion, a system for studying hydrocarbon permeation through single-crystal ferrierite membranes is presented. Assuming the transport mechanisms remain the same for polycrystalline membranes, this work sets an experimental upper limit for obtainable separation selectivities for polycrystalline ferrierite membranes. Currently, there is no directly comparable data in the literature; however, the data presented here will serve as a benchmark for future polycrystalline ferrierite membranes.

4.2 Future Directions

It is shown in the previous chapters that oriented single-crystal ferrierite membranes can be used to study hydrocarbon transport through the 8MR or 10MR channel systems. A logical extension of this technique is to study the transport of permanent gases by altering the sampling and detection methods to allow observation of permanent gas probe molecule flux through the single-crystal membrane.

The technique as applied to hydrocarbon probe molecules is not directly transferable to permanent gas probe molecules. First, the detector must be switched from a flame ionization detector (FID) to a mass spectrometer (MS) in order to detect the permeate. Second, the sampling procedure must be altered. Since the condensation temperatures of the permanent gases are much closer to the temperature of liquid nitrogen (77 K), the sample loop must be altered in order to quantitatively trap permeate from the crystal. Another issue is developing a protocol to deliver the collected permeate to the MS in such a way that a sharp, quantifiable response is detected.

Initial attempts to measure the flux of permanent gases through the single-crystal ferrierite membrane have not yielded quantifiable responses. Argon was choosen as the probe molecule in these preliminary experiments since it has a smaller reported kinetic diameter (3.4 Å) than nitrogen (3.6 Å)[1]. Nitrogen is capable of accessing both the 8MR and 10MR channel systems as shown in Chapter 3, so argon should also enter both these micropore systems. The sample loop was modified by packing it with calcined silicalite (a molecular sieve) to trap argon permeate at 77 K. Quantifiable delivery of the permeate into the MS has proven difficult. This issue is a challenge due to the small amount of permeate collected and the mixing of the permeate with the He carrier gas which causes a broadening of the original input pulse from the sampling loop. Unlike the FID technique described in Chapter 3 where all the permeate passes through the detector allowing for accurate quantitation of the collected permeate, only a fraction of the collected permeate enters the the MS due to splitting. Careful accounting must be employed to relate the amount of permeate detected by MS to the amount of permeate actually passing through the single-crystal membrane.

In summary, the possibility of studying the permeation of non-hydrocarbon probe molecules through a single-crystal ferrierite membrane exists. However, further experimentation with sampling and detection procedures is required to make this possibility a reality.

Literature Cited

[1] Breck, D. W. *Zeolite Molecular Sieves*; Krieger: Malabar, FL, 1974, p 636.

Appendix

Table A1. Anisotropic displacement parameters U_{ij} [10^7 pm^2] for **1a**. The anisotropic displacement factor exponent takes the form: $-2\pi^2 [h^2 a^{*2} U_{11} + ... + 2 h k a^* b^* U_{12}]$.

Atom	U_{11}	U_{22}	U_{33}	U_{23}	U_{13}	U_{12}
Si1	11(1)	9(1)	7(1)	0	0	1(1)
Si2	11(1)	11(1)	12(1)	1(1)	-1(1)	0(1)
Si3	12(1)	11(1)	11(1)	1(1)	1(1)	0(1)
Si4	11(1)	10(1)	11(1)	1(1)	1(1	1(1)
Si5	12(1)	9(1)	6(1)	1(1)	-1(1)	0(1)
O12	21(2)	57(2)	19(2)	0(1)	-11(1)	1(1)
O15	43(2)	14(1)	28(2)	-9(1)	-1(1)	1(1)
O22	14(2)	36(2)	20(2)	0	0	-2(1)
O23	38(1)	13(1)	26(2)	4(1)	5(1)	-7(1)
O24	40(2)	11(1)	29(1)	-2(1)	6(1)	8(1)
O34	49(2)	35(2)	21(2)	-17(1)	18(2)	-4(2)
O35	18(1)	29(1)	26(1)	9(1)	-6(1)	7(1)
O43	10(2)	30(2)	28(2)	5(1)	2(1)	1(1)
O45	18(1)	35(2)	27(1)	12(1)	-8(1)	5(1)
O55	37(2)	27(2)	3(2)	0	0	-1(2)
C1	118(10)	80(7)	61(6)	0	0	-9(5)
C2	103(6)	85(5)	76(4)	5(4)	2(3)	1(4)
C3	238(22)	121(12)	33(5)	0	0	3(17)
C4	294(42)	194(30)	36(6)	0	0	-57(23)
C5	162(19)	254(29)	42(7)	0	0	32(25)

Table A2. Anisotropic displacement parameters U_{ij} [10^7 pm^2] for **1b**. The anisotropic displacement factor exponent takes the form: $-2\pi^2 [h^2 a^{*2} U_{11} + ... + 2 h k a^* b^* U_{12}]$.

Atom	U_{11}	U_{22}	U_{33}	U_{23}	U_{13}	U_{12}
Si1	11(1)	9(1)	10(1)	0	0	0(1)
Si2	10(1)	10(1)	17(1)	1(1)	-2(1)	1(1)
Si3	10(1)	10(1)	11(1)	2(1)	-1(1)	1(1)
Si4	10(1)	9(1)	10(1)	1(1)	-1(1)	1(1)
Si5	10(1)	8(1)	7(1)	1(1)	-1(1)	-1(1)
O12	20(1)	46(2)	28(1)	-1(1)	-15(1)	4(1)
O15	38(1)	12(1)	30(1)	-9(1)	-4(1)	1(1)
O22	4(2)	40(2)	32(2)	0	0	-2(1)
O23	34(1)	13(1)	29(1)	5(1)	5(1)	-4(1)
O24	44(1)	12(1)	34(1)	-2(1)	5(1)	7(1)
O34	39(1)	35(2)	15(1)	-12(1)	2(1)	1(1)
O35	14(1)	26(1)	17(1)	4(1)	-3(1)	9(1)
O43	7(1)	32(2)	33(2)	7(1)	3(1)	2(1)
O45	16(1)	34(1)	22(1)	10(1)	-6(1)	6(1)
O55	23(2)	22(2)	7(2)	0	0	-4(1)

Table A3. Observed and calculated structure factors for **1a**.

h	k	l	10Fo	10Fc	10s	h	k	l	10Fo	10Fc	10s
2	0	0	1326	1402	23	3	12	0	45	40	14
3	10	1	1234	1229	22	3	8	2	9	21	9
7	6	3	206	208	8	4	0	0	3565	3555	63
4	12	0	58	67	10	4	10	1	40	43	16
4	8	2	572	545	11	0	7	3	2232	2207	56
6	0	0	1531	1550	32	5	12	0	43	32	13
5	10	1	172	172	7	5	8	2	25	30	24
1	7	3	76	69	4	8	0	0	119	143	12
1	13	0	281	281	8	6	10	1	42	48	13
6	8	2	328	328	9	2	7	3	476	492	9
1	1	0	1070	1133	19	2	13	0	39	17	15
0	11	1	159	151	8	7	8	2	92	104	7
3	7	3	92	93	5	2	1	0	85	88	3
3	13	0	635	608	18	1	11	1	0	46	1
1	9	2	160	162	6	4	7	3	1024	1049	19
3	1	0	276	328	6	4	13	0	121	124	5
2	11	1	693	704	13	2	9	2	73	65	6
5	7	3	71	79	10	4	1	0	288	264	10
0	14	0	1101	1094	29	3	11	1	36	47	35
3	9	2	77	76	13	6	7	3	384	371	9
5	1	0	415	436	11	1	14	0	23	10	22
4	11	1	172	142	7	4	9	2	26	1	25
7	7	3	54	63	8	6	1	0	63	78	15
2	14	0	35	41	34	5	11	1	0	3	1
5	9	2	217	226	8	1	8	3	825	843	15
7	1	0	583	551	63	3	14	0	0	23	1
1	12	1	108	127	5	6	9	2	0	12	1
2	8	3	34	44	15	8	1	0	0	38	1
1	15	0	627	639	12	2	12	1	44	49	10
0	10	2	1288	1262	33	3	8	3	865	883	16
0	2	0	1088	1175	27	2	15	0	0	19	1
3	12	1	604	591	12	1	10	2	74	66	6
4	8	3	150	151	6	1	2	0	86	90	3
1	0	1	922	960	16	4	12	1	54	58	10
2	10	2	1358	1314	24	5	8	3	1333	1331	24
2	2	0	571	568	10	3	0	1	506	576	22
5	12	1	355	371	11	3	10	2	33	30	33
6	8	3	0	8	1	3	2	0	42	43	9
5	0	1	583	566	11	0	13	1	51	30	14
4	10	2	361	358	9	7	8	3	443	464	22
4	2	0	326	346	7	7	0	1	829	838	27
1	13	1	33	33	33	5	10	2	0	32	1
0	9	3	790	780	21	5	2	0	110	97	6
0	1	1	222	311	6	2	13	1	340	333	9
6	10	2	0	9	1	1	9	3	125	116	5
6	2	0	407	420	15	1	1	1	14	19	13
3	13	1	0	50	1	1	11	2	219	221	10
2	9	3	749	720	14	7	2	0	27	33	26
2	1	1	1813	1815	32	4	13	1	91	90	5
2	11	2	0	33	1	3	9	3	77	83	7

Table A3. Observed and calculated structure factors for **1a**.

h	k	l	10Fo	10Fc	10s	h	k	l	10Fo	10Fc	10s
8	2	0	95	91	14	3	1	1	106	92	8
1	14	1	165	161	6	3	11	2	91	91	9
4	9	3	371	358	15	1	3	0	1565	1588	28
4	1	1	361	350	25	2	14	1	0	14	1
4	11	2	0	29	1	5	9	3	122	123	5
2	3	0	60	57	3	5	1	1	34	13	33
3	14	1	444	437	9	5	11	2	334	348	13
6	9	3	157	168	12	3	3	0	32	42	10
6	1	1	590	550	57	0	15	1	119	110	7
0	12	2	690	690	19	1	10	3	39	45	16
4	3	0	278	262	7	7	1	1	125	124	7
1	15	1	34	38	34	1	12	2	17	22	17
2	10	3	78	72	15	5	3	0	1785	1788	32
8	1	1	260	257	27	2	15	1	654	657	12
2	12	2	60	64	8	3	10	3	859	836	21
6	3	0	81	80	7	1	2	1	743	803	13
0	0	2	2529	2636	64	3	12	2	0	6	1
4	10	3	138	138	5	7	3	0	749	735	24
2	2	1	53	58	4	2	0	2	2927	3431	152
4	12	2	491	488	14	5	10	3	500	492	10
8	3	0	49	54	9	3	2	1	182	228	5
4	0	2	1017	958	38	5	12	2	0	15	1
6	10	3	22	18	21	0	4	0	4122	3952	104
4	2	1	0	17	1	6	0	2	252	249	8
1	13	2	20	10	20	0	11	3	187	197	11
1	4	0	107	104	4	5	2	1	104	93	5
8	0	2	410	416	31	2	13	2	65	65	9
1	11	3	62	64	45	2	4	0	818	819	15
6	2	1	0	13	1	1	1	2	221	231	4
3	13	2	663	630	13	2	11	3	1142	1150	21
3	4	0	53	47	7	7	2	1	499	500	25
2	1	2	161	148	5	4	13	2	38	19	23
3	11	3	0	24	1	4	4	0	855	898	15
8	2	1	48	55	9	3	1	2	87	38	11
0	14	2	655	635	18	4	11	3	71	74	28
5	4	0	261	244	7	0	3	1	264	308	7
4	1	2	56	51	6	1	14	2	0	8	1
5	11	3	89	105	8	6	4	0	1174	1183	21
1	3	1	15	20	14	5	1	2	285	288	22
2	14	2	423	414	9	1	12	3	885	849	17
7	4	0	0	4	1	2	3	1	722	723	13
6	1	2	141	137	19	3	14	2	38	46	15
2	12	3	0	30	1	8	4	0	226	237	7
3	3	1	95	95	4	7	1	2	216	212	32
1	15	2	169	156	7	3	12	3	486	477	10
1	5	0	1439	1486	25	4	3	1	78	66	4
8	1	2	34	31	34	2	15	2	37	24	13
4	12	3	28	57	27	2	5	0	56	53	4
5	3	1	70	77	7	0	2	2	462	529	12
1	0	3	710	604	13	5	12	3	1178	1199	21

Table A3. Observed and calculated structure factors for **1a**.

h	k	l	10Fo	10Fc	10s	h	k	l	10Fo	10Fc	10s
3	5	0	218	226	6	6	3	1	127	122	6
1	2	2	0	19	1	3	0	3	50	84	10
0	13	3	580	574	17	4	5	0	122	116	8
7	3	1	108	103	6	2	2	2	449	476	8
5	0	3	509	461	22	1	13	3	0	7	1
5	5	0	1483	1494	27	8	3	1	237	245	14
3	2	2	34	37	9	7	0	3	729	728	50
2	13	3	104	109	10	6	5	0	49	40	16
1	4	1	602	589	11	4	2	2	230	235	6
0	1	3	715	800	18	3	13	3	0	0	1
7	5	0	244	243	7	2	4	1	133	124	8
5	2	2	0	9	1	1	1	3	0	23	1
4	13	3	247	242	7	0	6	0	650	531	17
3	4	1	335	304	7	6	2	2	541	531	19
2	1	3	1471	1440	52	1	14	3	62	66	13
1	6	0	222	220	5	4	4	1	77	72	6
7	2	2	60	73	15	3	1	3	0	10	1
2	14	3	0	31	1	2	6	0	416	403	8
5	4	1	354	342	13	8	2	2	137	138	10
4	1	3	636	607	29	3	14	3	274	272	7
3	6	0	0	1	1	6	4	1	85	71	6
1	3	2	103	112	10	5	1	3	268	242	12
0	15	3	568	552	16	4	6	0	98	115	5
7	4	1	240	255	8	2	3	2	130	132	4
6	1	3	555	543	58	1	15	3	69	68	7
5	6	0	227	217	11	8	4	1	115	127	14
3	3	2	981	1048	17	7	1	3	101	106	7
2	15	3	765	747	14	6	6	0	431	447	23
0	5	1	194	195	7	4	3	2	60	55	6
8	1	3	175	178	31	0	0	4	666	750	17
7	6	0	0	7	1	1	5	1	0	5	1
5	3	2	680	689	13	1	2	3	1989	1970	35
2	0	4	937	875	17	1	7	0	1386	1416	25
2	5	1	726	812	13	6	3	2	108	113	9
2	2	3	37	25	8	4	0	4	351	364	8
2	7	0	140	136	5	3	5	1	0	4	1
7	3	2	938	946	34	3	2	3	65	36	4
6	0	4	830	825	21	3	7	0	185	193	6
4	5	1	339	349	7	8	3	2	0	20	1
4	2	3	107	101	4	8	0	4	236	279	25
4	7	0	76	70	6	5	5	1	27	5	26
0	4	2	1910	1895	48	5	2	3	1691	1689	74
1	1	4	1188	1167	30	5	7	0	1791	1809	32
6	5	1	295	295	8	1	4	2	70	72	3
6	2	3	42	45	27	2	1	4	59	54	9
6	7	0	138	135	6	7	5	1	28	18	27
2	4	2	613	671	11	7	2	3	438	424	30
3	1	4	616	593	12	7	7	0	658	672	19
1	6	1	112	135	4	3	4	2	98	86	4
8	2	3	0	27	1	4	1	4	182	171	8

Table A3. Observed and calculated structure factors for **1a**.

h	k	l	10Fo	10Fc	10s	h	k	l	10Fo	10Fc	10s
0	8	0	441	409	12	2	6	1	136	133	5
4	4	2	554	547	11	0	3	3	2595	2533	65
5	1	4	1152	1097	86	1	8	0	22	10	22
3	6	1	644	631	12	5	4	2	34	35	19
1	3	3	26	10	25	6	1	4	118	117	21
2	8	0	562	529	11	4	6	1	0	14	1
6	4	2	277	272	8	2	3	3	391	421	8
7	1	4	47	42	47	3	8	0	36	34	35
5	6	1	40	10	31	7	4	2	145	144	6
3	3	3	33	26	9	8	1	4	78	94	12
4	8	0	339	328	8	6	6	1	48	69	21
8	4	2	217	242	17	4	3	3	859	847	26
0	2	4	2475	2407	62	5	8	0	123	119	5
7	6	1	207	190	23	1	5	2	202	220	5
5	3	3	148	134	7	1	2	4	116	108	5
6	8	0	162	187	6	0	7	1	243	249	8
2	5	2	0	33	1	6	3	3	502	488	26
2	2	4	800	800	22	7	8	0	25	27	24
1	7	1	0	4	1	3	5	2	722	717	13
7	3	3	62	65	9	3	2	4	123	113	5
1	9	0	944	925	17	2	7	1	1043	1023	19
4	5	2	33	45	33	8	3	3	0	11	1
4	2	4	64	82	10	2	9	0	2	14	2
3	7	1	97	92	5	5	5	2	20	53	20
1	4	3	0	35	1	5	2	4	13	6	13
3	9	0	700	711	13	4	7	1	117	119	5
6	5	2	83	76	8	2	4	3	0	5	1
6	2	4	672	688	47	4	9	0	57	56	57
5	7	1	38	7	20	7	5	2	226	223	8
3	4	3	646	624	12	7	2	4	0	28	1
5	9	0	555	567	12	6	7	1	230	217	8
0	6	2	884	919	23	4	4	3	87	81	5
8	2	4	377	405	51	6	9	0	71	75	7
7	7	1	69	75	7	1	6	2	0	5	1
5	4	3	163	151	7	1	3	4	44	44	5
0	10	0	2991	2994	76	1	8	1	143	119	6
2	6	2	210	197	6	6	4	3	62	74	22
2	3	4	111	105	13	1	10	0	11	6	11
2	8	1	97	90	5	3	6	2	110	109	4
7	4	3	196	198	16	3	3	4	28	17	27
2	10	0	221	233	7	3	8	1	960	966	24
4	6	2	29	22	29	0	5	3	976	998	25
4	3	4	96	89	7	3	10	0	99	101	6
4	8	1	27	48	27	5	6	2	0	17	1
1	5	3	48	49	4	5	3	4	174	169	23
4	10	0	1854	1869	33	5	8	1	370	376	9
6	6	2	492	508	14	2	5	3	253	348	7
6	3	4	137	137	11	5	10	0	39	36	27
6	8	1	0	47	1	7	6	2	130	145	6
3	5	3	28	33	13	7	3	4	142	140	6

Table A3. Observed and calculated structure factors for **1a**.

h	k	l	10Fo	10Fc	10s	h	k	l	10Fo	10Fc	10s
6	10	0	606	607	12	7	8	1	412	426	14
1	7	2	47	52	5	4	5	3	318	312	7
8	3	4	17	47	17	1	11	0	355	378	8
0	9	1	0	13	1	2	7	2	0	35	1
5	5	3	83	80	6	0	4	4	213	216	7
2	11	0	31	44	31	1	9	1	0	29	1
3	7	2	955	988	17	6	5	3	170	174	7
1	4	4	114	111	4	3	11	0	467	457	10
2	9	1	638	659	12	4	7	2	89	85	5
7	5	3	36	32	35	2	4	4	676	713	12
4	11	0	38	52	21	3	9	1	83	80	6
5	7	2	700	708	15	1	6	3	110	113	7
3	4	4	22	21	21	5	11	0	57	40	8
4	9	1	135	132	6	6	7	2	58	48	21
2	6	3	88	84	4	4	4	4	419	396	18
6	11	0	94	95	5	5	9	1	23	31	23
7	7	2	849	892	37	3	6	3	375	392	8
5	4	4	25	24	24	0	12	0	292	305	12
6	9	1	245	245	9	0	8	2	1118	1055	29
4	6	3	159	154	6	6	4	4	509	517	34
1	12	0	0	16	1	1	10	1	633	637	12
1	8	2	98	100	4	5	6	3	206	204	7
7	4	4	11	32	10	2	12	0	425	446	10
2	10	1	99	93	9	2	8	2	273	289	7
6	6	3	40	49	15	1	5	4	735	762	13
2	5	4	0	18	1	6	3	5	474	469	27
6	2	6	146	146	30	1	2	7	536	584	10
1	2	8	62	65	6	3	5	4	46	48	10
7	3	5	56	50	10	7	2	6	58	73	17
2	2	7	0	37	1	2	2	8	366	291	16
4	5	4	80	75	25	1	4	5	210	212	5
1	3	6	845	871	17	3	2	7	1689	1674	30
3	2	8	24	15	23	5	5	4	1161	1165	26
2	4	5	0	22	1	2	3	6	124	114	5
4	2	7	48	43	11	4	2	8	582	554	34
6	5	4	44	47	12	3	4	5	336	335	7
3	3	6	1141	1116	30	5	2	7	245	247	19
5	2	8	44	61	44	7	5	4	189	189	20
4	4	5	0	38	1	4	3	6	99	103	7
6	2	7	70	65	8	6	2	8	156	147	12
0	6	4	1098	1073	28	5	4	5	0	16	1
5	3	6	275	284	12	7	2	7	695	704	63
7	2	8	57	54	13	1	6	4	115	110	4
6	4	5	0	24	1	6	3	6	54	54	11
0	3	7	1071	1087	27	1	3	8	180	190	6
2	6	4	575	614	11	7	4	5	121	117	11
7	3	6	775	781	46	1	3	7	183	181	5
2	3	8	89	86	5	3	6	4	63	66	6
0	5	5	467	640	13	0	4	6	799	734	20
2	3	7	356	326	8	3	3	8	98	119	12

Table A3. Observed and calculated structure factors for **1a**.

h	k	l	10Fo	10Fc	10s	h	k	l	10Fo	10Fc	10s
4	6	4	77	73	6	1	5	5	60	60	4
1	4	6	24	19	23	3	3	7	46	46	19
4	3	8	49	47	27	5	6	4	0	26	1
2	5	5	320	339	9	2	4	6	1059	1005	19
4	3	7	1045	1034	22	5	3	8	466	422	30
6	6	4	300	322	8	3	5	5	50	45	14
3	4	6	77	68	5	5	3	7	0	44	1
6	3	8	0	33	1	7	6	4	30	9	30
4	5	5	561	568	16	4	4	6	199	176	7
6	3	7	438	420	20	7	3	8	182	205	29
1	7	4	42	54	11	5	5	5	49	49	17
5	4	6	95	90	6	7	3	7	0	13	1
0	4	8	968	915	25	2	7	4	0	19	1
6	5	5	362	364	19	6	4	6	287	303	9
1	4	7	0	16	1	1	4	8	134	126	5
3	7	4	176	194	7	7	5	5	49	56	15
7	4	6	131	137	7	2	4	7	0	14	1
2	4	8	824	744	15	4	7	4	66	71	8
1	6	5	786	764	14	1	5	6	1017	983	18
3	4	7	643	643	12	3	4	8	26	16	26
5	7	4	45	33	30	2	6	5	20	37	20
2	5	6	123	116	11	4	4	7	43	35	42
4	4	8	287	281	8	6	7	4	0	2	1
3	6	5	650	638	12	3	5	6	905	913	16
5	4	7	479	487	17	5	4	8	88	94	8
7	7	4	152	161	5	4	6	5	82	81	6
4	5	6	35	45	20	6	4	7	91	95	8
6	4	8	58	66	24	0	8	4	737	787	19
5	6	5	546	526	18	5	5	6	1449	1448	52
7	4	7	396	413	28	7	4	8	125	128	18
1	8	4	119	107	7	6	6	5	0	3	1
6	5	6	49	38	14	0	5	7	272	262	9
1	5	8	886	839	16	2	8	4	554	562	14
7	6	5	90	82	11	7	5	6	852	891	48
1	5	7	91	98	4	2	5	8	22	17	22
3	8	4	81	76	6	0	7	5	1615	1567	41
0	6	6	159	173	8	2	5	7	449	461	9
3	5	8	693	684	17	4	8	4	640	654	16
1	7	5	0	28	1	1	6	6	26	45	26
3	5	7	39	24	13	4	5	8	0	8	1
5	8	4	52	39	11	2	7	5	90	85	6
2	6	6	117	114	12	4	5	7	152	161	6
5	5	8	1293	1267	31	6	8	4	149	171	12
3	7	5	0	4	1	3	6	6	78	78	6
5	5	7	15	16	15	6	5	8	0	24	1
7	8	4	0	4	1	4	7	5	753	753	18
4	6	6	219	213	10	6	5	7	304	292	17
7	5	8	484	479	52	1	9	4	729	741	14
5	7	5	73	80	13	5	6	6	133	139	7
7	5	7	0	32	1	0	6	8	543	528	15

Table A3. Observed and calculated structure factors for **1a**.

h	k	l	10Fo	10Fc	10s	h	k	l	10Fo	10Fc	10s
2	9	4	36	11	36	6	7	5	382	374	9
6	6	6	208	205	11	1	6	7	19	9	19
1	6	8	86	85	7	3	9	4	189	203	7
7	7	5	35	18	16	7	6	6	134	138	6
2	6	7	66	57	6	2	6	8	0	8	1
4	9	4	0	11	1	1	8	5	602	633	11
1	7	6	447	456	9	3	6	7	955	930	33
3	6	8	30	36	29	5	9	4	871	867	16
2	8	5	13	16	13	2	7	6	103	101	8
4	6	7	46	52	45	4	6	8	269	259	8
6	9	4	0	4	1	3	8	5	160	163	7
3	7	6	1023	1030	30	5	6	7	420	407	28
5	6	8	105	95	6	0	10	4	203	230	10
4	8	5	0	4	1	4	7	6	0	4	1
6	6	7	86	91	14	6	6	8	333	371	13
1	10	4	34	13	22	5	8	5	1026	1029	24
5	7	6	123	104	13	7	6	7	385	400	13
7	6	8	110	133	8	2	10	4	591	604	12
6	8	5	49	66	27	6	7	6	31	30	30
0	7	7	1374	1375	35	1	7	8	0	15	1
3	10	4	0	27	1	0	9	5	834	805	22
7	7	6	681	728	34	1	7	7	181	175	9
2	7	8	0	3	1	4	10	4	614	637	16
1	9	5	0	9	1	0	8	6	1043	1010	27
2	7	7	425	416	10	3	7	8	296	306	15
5	10	4	38	37	29	2	9	5	481	503	10
1	8	6	42	43	9	3	7	7	64	53	7
4	7	8	0	1	1	6	10	4	48	47	8
3	9	5	30	13	30	2	8	6	1974	1977	35
4	7	7	1022	1026	24	5	7	8	453	423	10
1	11	4	579	595	12	4	9	5	560	572	18
3	8	6	24	18	24	5	7	7	9	13	8
6	7	8	0	5	1	2	11	4	0	29	1
5	9	5	23	35	23	4	8	6	61	63	8
6	7	7	461	457	10	0	8	8	1785	1761	45
3	11	4	105	112	5	6	9	5	0	20	1
5	8	6	112	118	6	1	8	7	511	502	10
1	8	8	171	176	6	4	11	4	0	19	1
1	10	5	546	551	11	6	8	6	431	446	14
2	8	7	26	16	26	2	8	8	751	726	14
5	11	4	641	646	22	2	10	5	41	5	14
1	9	6	548	532	11	3	8	7	847	841	16
3	8	8	37	45	36	0	12	4	510	497	15
3	10	5	634	629	12	2	9	6	91	91	5
4	8	7	0	4	1	4	8	8	748	737	21
1	12	4	26	12	26	4	10	5	0	10	1
3	9	6	328	321	8	5	8	7	169	167	7
5	8	8	37	67	36	2	12	4	474	481	11
5	10	5	534	526	11	4	9	6	88	85	6
6	8	7	46	46	15	6	8	8	285	304	8

Table A3. Observed and calculated structure factors for **1a**.

h	k	l	10Fo	10Fc	10s	h	k	l	10Fo	10Fc	10s
3	12	4	0	39	1	6	10	5	21	28	20
5	9	6	821	823	22	0	9	7	438	426	14
1	9	8	300	280	8	4	12	4	345	352	9
0	11	5	926	988	25	6	9	6	0	14	1
1	9	7	181	172	8	2	9	8	82	74	7
5	12	4	61	67	7	1	11	5	107	109	6
0	10	6	984	990	26	2	9	7	228	212	8
3	9	8	420	399	10	1	13	4	154	147	6
2	11	5	374	369	9	1	10	6	124	122	8
3	9	7	89	99	6	4	9	8	96	104	11
2	13	4	32	4	24	3	11	5	51	52	10
2	10	6	1340	1347	24	4	9	7	251	240	8
5	9	8	540	504	11	3	13	4	24	25	23
4	11	5	573	588	21	3	10	6	86	84	10
5	9	7	63	62	10	6	9	8	0	27	1
4	13	4	0	26	1	5	11	5	50	49	11
4	10	6	252	273	14	6	9	7	38	19	38
0	10	8	1355	1313	35	0	14	4	159	159	8
1	12	5	341	335	9	5	10	6	0	3	1
1	10	7	576	555	12	1	10	8	149	131	6
1	14	4	23	4	22	2	12	5	53	55	11
6	10	6	289	315	7	2	10	7	46	8	15
2	10	8	1211	1176	26	2	14	4	426	413	9
3	12	5	339	310	9	1	11	6	50	50	19
3	10	7	254	267	8	3	10	8	62	55	8
3	14	4	36	8	28	4	12	5	35	48	20
2	11	6	76	84	8	4	10	7	0	3	1
4	10	8	432	426	15	1	15	4	418	425	9
5	12	5	772	790	14	3	11	6	446	426	11
5	10	7	697	698	13	5	10	8	34	11	33
2	15	4	44	41	12	0	13	5	444	423	14
4	11	6	71	66	7	0	11	7	514	483	16
1	11	8	222	202	8	1	0	5	1880	1694	33
1	13	5	13	14	13	5	11	6	281	295	7
1	11	7	189	170	8	2	11	8	0	61	1
3	0	5	124	105	9	2	13	5	165	168	6
0	12	6	706	683	20	2	11	7	95	91	11
3	11	8	195	195	7	5	0	5	1186	1122	37
3	13	5	0	16	1	1	12	6	80	84	7
3	11	7	80	72	15	4	11	8	78	81	7
7	0	5	134	139	16	4	13	5	199	190	7
2	12	6	1228	1143	22	4	11	7	368	359	9
5	11	8	348	362	8	0	1	5	2127	2122	54
1	14	5	24	27	23	3	12	6	59	78	17
5	11	7	32	27	31	0	12	8	1239	1162	32
1	1	5	121	112	16	2	14	5	0	29	1
4	12	6	41	10	20	1	12	7	410	417	9
1	12	8	72	67	8	2	1	5	596	579	11
3	14	5	193	199	7	1	13	6	545	558	11
2	12	7	63	63	22	2	12	8	361	353	10

Table A3. Observed and calculated structure factors for **1a**.

h	k	l	10Fo	10Fc	10s	h	k	l	10Fo	10Fc	10s
3	1	5	80	72	5	0	15	5	873	855	23
2	13	6	80	85	18	3	12	7	676	663	13
3	12	8	0	3	1	4	1	5	1124	1050	52
1	15	5	80	76	5	3	13	6	663	670	13
4	12	7	7	46	6	4	12	8	429	418	18
5	1	5	131	124	21	0	0	6	1323	1165	33
4	13	6	79	89	6	0	13	7	894	831	24
1	13	8	193	196	8	6	1	5	124	116	18
2	0	6	1434	1371	25	0	14	6	369	367	12
1	13	7	56	38	9	2	13	8	82	83	6
7	1	5	123	115	16	4	0	6	322	295	8
1	14	6	50	50	9	2	13	7	76	83	7
3	13	8	0	3	1	8	1	5	32	77	32
6	0	6	491	404	11	2	14	6	59	57	14
3	13	7	21	21	21	0	14	8	363	346	13
1	2	5	1229	1184	22	8	0	6	229	275	129
3	14	6	91	94	10	1	14	7	123	129	5
1	14	8	0	34	1	2	2	5	76	72	4
1	1	6	811	793	41	1	15	6	113	119	5
2	14	7	44	42	31	2	14	8	283	289	9
3	2	5	1526	1440	55	2	1	6	161	153	12
1	0	7	1010	910	18	0	0	8	207	320	8
1	0	9	1393	1318	25	4	2	5	0	19	1
3	1	6	520	509	22	3	0	7	274	282	13
2	0	8	1066	993	19	3	0	9	1478	1410	26
5	2	5	1720	1690	58	4	1	6	73	61	7
5	0	7	1038	951	19	4	0	8	631	566	16
5	0	9	1957	1835	35	6	2	5	0	31	1
5	1	6	857	857	54	7	0	7	222	211	11
6	0	8	207	221	8	7	0	9	958	875	23
7	2	5	404	376	39	6	1	6	106	93	13
0	1	7	161	122	8	1	1	8	85	77	4
0	1	9	86	73	6	8	2	5	11	15	10
7	1	6	357	361	35	1	1	7	39	20	10
2	1	8	110	99	4	1	1	9	37	25	9
0	3	5	1254	1247	32	0	2	6	305	346	9
2	1	7	314	308	7	3	1	8	646	597	12
2	1	9	153	169	5	1	3	5	0	14	1
1	2	6	82	71	4	3	1	7	59	49	16
4	1	8	102	90	6	3	1	9	70	62	7
2	3	5	108	81	6	2	2	6	388	489	8
4	1	7	379	342	18	5	1	8	662	594	15
4	1	9	103	64	26	3	3	5	42	44	15
3	2	6	57	49	7	5	1	7	90	101	9
6	1	8	0	36	1	5	1	9	210	186	9
4	3	5	516	516	28	4	2	6	112	93	6
6	1	7	48	72	28	7	1	8	318	289	23
6	1	9	164	149	7	5	3	5	131	124	6
5	2	6	116	114	9	7	1	7	24	12	23
0	2	8	130	179	8	7	1	9	78	78	8

Table A3. Observed and calculated structure factors for **1a**.

h	k	l	10Fo	10Fc	10s	h	k	l	10Fo	10Fc	10s
1	2	9	919	867	17	5	2	10	43	47	43
6	3	11	421	387	30	2	6	12	498	468	11
3	10	13	0	8	1	2	2	9	20	14	20
6	2	10	580	516	27	1	4	11	139	145	6
3	6	12	0	41	1	0	11	13	37	73	37
3	2	9	257	254	8	7	2	10	0	10	1
2	4	11	123	115	5	4	6	12	86	48	18
1	11	13	102	104	6	4	2	9	0	23	1
1	3	10	189	190	8	3	4	11	813	826	16
5	6	12	198	197	14	2	11	13	527	528	11
5	2	9	803	790	16	2	3	10	91	86	6
4	4	11	0	2	1	6	6	12	432	435	30
3	11	13	84	88	7	6	2	9	0	33	1
3	3	10	670	663	13	5	4	11	729	671	19
1	7	12	808	848	16	1	12	13	160	158	6
7	2	9	0	49	1	4	3	10	162	155	7
6	4	11	98	97	10	2	7	12	71	80	11
0	0	14	1000	954	26	0	3	9	2119	2262	54
5	3	10	162	140	7	0	5	11	404	381	14
3	7	12	0	45	1	2	0	14	1738	1722	31
1	3	9	92	89	8	6	3	10	17	20	16
1	5	11	0	25	1	4	7	12	109	93	6
4	0	14	298	305	8	2	3	9	710	729	13
7	3	10	269	256	13	2	5	11	422	446	11
5	7	12	944	880	18	6	0	14	358	380	12
3	3	9	76	78	7	0	4	10	558	549	16
3	5	11	16	20	15	0	8	12	1063	1136	29
1	1	14	173	175	15	4	3	9	1132	1146	71
1	4	10	98	94	7	4	5	11	438	453	11
1	8	12	84	86	8	2	1	14	218	214	8
5	3	9	141	141	15	2	4	10	585	596	12
5	5	11	64	61	39	2	8	12	386	385	14
3	1	14	416	416	9	6	3	9	234	247	39
3	4	10	118	114	7	6	5	11	82	74	7
3	8	12	0	21	1	4	1	14	103	106	12
7	3	9	36	8	35	4	4	10	802	796	45
1	6	11	198	203	7	4	8	12	340	306	9
5	1	14	203	180	7	1	4	9	607	564	12
5	4	10	0	47	1	2	6	11	117	126	16
5	8	12	133	143	6	6	1	14	112	121	5
2	4	9	59	63	11	6	4	10	0	30	1
3	6	11	380	358	15	1	9	12	391	380	10
0	2	14	1276	1243	33	3	4	9	1301	1309	29
7	4	10	0	3	1	4	6	11	46	40	20
2	9	12	102	114	8	1	2	14	0	14	1
4	4	9	0	28	1	1	5	10	132	37	50
5	6	11	569	563	29	3	9	12	199	205	12
2	2	14	1475	1462	27	5	4	9	939	933	66
2	5	10	12	33	11	6	6	11	125	119	6
4	9	12	67	79	10	3	2	14	53	70	23

Table A3. Observed and calculated structure factors for **1a**.

h	k	l	10Fo	10Fc	10s	h	k	l	10Fo	10Fc	10s
6	4	9	101	115	8	3	5	10	328	318	9
0	7	11	1063	1016	28	0	10	12	1394	1453	36
4	2	14	93	84	6	7	4	9	601	622	71
4	5	10	0	15	1	1	7	11	33	13	32
1	10	12	87	85	22	5	2	14	0	12	1
0	5	9	0	48	1	5	5	10	152	98	60
2	7	11	2090	2107	37	2	10	12	150	158	6
6	2	14	41	43	41	1	5	9	56	58	10
6	5	10	54	31	13	3	7	11	85	92	9
3	10	12	27	58	26	1	3	14	134	139	6
2	5	9	290	276	7	0	6	10	663	592	19
4	7	11	124	112	6	4	10	12	857	836	16
2	3	14	145	142	5	3	5	9	0	25	1
1	6	10	72	67	8	5	7	11	61	82	12
1	11	12	115	110	7	3	3	14	511	499	11
4	5	9	215	199	8	2	6	10	465	471	10
6	7	11	469	457	10	2	11	12	0	59	1
4	3	14	116	118	6	5	5	9	0	47	1
3	6	10	125	125	7	1	8	11	524	521	11
3	11	12	0	9	1	5	3	14	407	405	9
6	5	9	30	70	30	4	6	10	325	321	9
2	8	11	98	93	7	0	12	12	805	838	22
6	3	14	49	67	15	7	5	9	23	10	22
5	6	10	47	11	15	3	8	11	600	599	13
1	12	12	53	85	52	0	4	14	144	131	8
1	6	9	406	405	9	6	6	10	272	285	38
4	8	11	44	63	43	2	12	12	150	142	7
1	4	14	22	35	21	2	6	9	59	59	8
1	7	10	437	434	10	5	8	11	251	274	9
1	0	13	393	396	9	2	4	14	490	487	10
3	6	9	678	642	13	2	7	10	0	46	1
0	9	11	132	127	9	3	0	13	418	420	9
3	4	14	29	35	28	4	6	9	0	26	1
3	7	10	664	632	13	1	9	11	69	55	9
5	0	13	852	815	16	4	4	14	308	295	8
5	6	9	109	90	23	4	7	10	0	40	1
2	9	11	257	280	9	0	1	13	229	194	10
5	4	14	14	29	13	6	6	9	65	82	12
5	7	10	237	230	8	3	9	11	56	64	13
1	1	13	252	255	7	1	5	14	524	553	17
0	7	9	2238	2163	57	6	7	10	0	41	1
4	9	11	106	108	7	2	1	13	701	713	13
2	5	14	116	124	6	1	7	9	152	155	6
0	8	10	560	523	17	5	9	11	76	90	28
3	1	13	249	239	8	3	5	14	1445	1379	28
2	7	9	795	809	15	1	8	10	147	140	6
1	10	11	126	126	12	4	1	13	289	280	8
4	5	14	94	100	7	3	7	9	89	68	7
2	8	10	585	580	12	2	10	11	73	60	20
5	1	13	0	11	1	5	5	14	307	278	8

Table A3. Observed and calculated structure factors for **1a**.

h	k	l	10Fo	10Fc	10s	h	k	l	10Fo	10Fc	10s
4	7	9	1267	1239	26	3	8	10	100	106	7
3	10	11	1175	1180	22	6	1	13	144	115	6
0	6	14	975	942	26	5	7	9	61	57	18
4	8	10	676	669	14	4	10	11	0	33	1
1	2	13	0	3	1	1	6	14	0	28	1
6	7	9	205	209	8	5	8	10	25	31	24
0	11	11	249	197	14	2	2	13	44	49	16
2	6	14	353	378	11	1	8	9	144	149	6
6	8	10	172	193	20	1	11	11	120	112	7
3	2	13	500	467	11	3	6	14	58	69	13
2	8	9	16	5	15	1	9	10	82	83	7
2	11	11	25	9	24	4	2	13	143	143	6
4	6	14	441	426	10	3	8	9	516	513	20
2	9	10	19	50	19	3	11	11	32	27	31
5	2	13	278	265	8	5	6	14	0	45	1
4	8	9	38	26	20	3	9	10	269	260	9
4	11	11	27	13	26	6	2	13	25	34	24
1	7	14	127	123	6	5	8	9	160	157	6
4	9	10	101	116	7	1	12	11	356	377	9
0	3	13	1043	998	27	2	7	14	21	49	21
6	8	9	0	16	1	5	9	10	0	3	1
2	12	11	29	2	29	1	3	13	104	111	5
3	7	14	445	431	10	0	9	9	240	229	11
0	10	10	279	289	13	3	12	11	512	509	17
2	3	13	695	675	13	4	7	14	41	45	15
1	9	9	160	148	12	1	10	10	0	37	1
0	13	11	379	368	13	3	3	13	111	112	8
5	7	14	444	431	9	2	9	9	103	104	6
2	10	10	26	16	25	1	13	11	76	85	8
4	3	13	315	292	9	0	8	14	464	455	15
3	9	9	141	137	6	3	10	10	34	21	33
0	0	12	2365	2300	60	5	3	13	34	15	34
1	8	14	16	41	16	4	9	9	113	112	8
4	10	10	168	188	7	2	0	12	374	351	8
6	3	13	132	127	5	2	8	14	687	656	14
5	9	9	98	103	6	5	10	10	0	10	1
4	0	12	1819	1754	33	1	4	13	457	454	10
3	8	14	17	41	17	1	10	9	219	232	9
1	11	10	150	155	10	6	0	12	348	304	9
2	4	13	81	69	7	4	8	14	182	178	7
2	10	9	0	31	1	2	11	10	0	2	1
1	1	12	350	334	8	3	4	13	416	412	10
1	9	14	232	241	11	3	10	9	721	657	14
3	11	10	118	111	6	2	1	12	33	27	17
4	4	13	188	179	6	2	9	14	19	4	18
4	10	9	35	54	35	4	11	10	42	83	42
3	1	12	183	173	8	5	4	13	579	563	12
3	9	14	567	547	11	5	10	9	771	809	15
0	12	10	236	235	13	4	1	12	160	168	6
6	4	13	38	57	20	4	9	14	56	59	8

Table A3. Observed and calculated structure factors for **1a**.

h	k	l	10Fo	10Fc	10s	h	k	l	10Fo	10Fc	10s
0	11	9	164	134	11	1	12	10	72	65	8
5	1	12	391	384	9	0	5	13	248	252	13
0	10	14	248	229	12	1	11	9	74	70	9
2	12	10	283	304	9	6	1	12	109	105	7
1	5	13	88	88	7	1	10	14	42	57	33
2	11	9	82	77	7	3	12	10	43	40	13
0	2	12	1288	1234	33	2	5	13	1317	1266	24
2	10	14	757	715	14	3	11	9	5	42	4
1	13	10	310	296	9	1	2	12	138	130	6
3	5	13	49	72	34	3	10	14	0	30	1
4	11	9	115	124	5	2	13	10	0	19	1
2	2	12	306	315	8	4	5	13	414	381	10
1	11	14	0	14	1	1	12	9	215	181	8
1	0	11	160	175	6	3	2	12	82	74	16
5	5	13	0	18	1	2	11	14	10	45	9
2	12	9	0	16	1	3	0	11	1959	1931	35
4	2	12	830	811	16	6	5	13	533	529	15
1	0	15	130	128	9	3	12	9	247	256	8
5	0	11	818	785	16	5	2	12	149	148	7
1	6	13	848	815	16	3	0	15	304	305	9
4	12	9	25	40	25	7	0	11	1343	1290	24
6	2	12	211	189	8	2	6	13	112	102	6
5	0	15	99	101	6	0	13	9	860	840	23
0	1	11	124	85	7	1	3	12	861	831	16
3	6	13	20	40	20	0	1	15	677	693	19
1	13	9	0	11	1	1	1	11	29	29	29
2	3	12	0	40	1	4	6	13	226	212	16
1	1	15	365	360	9	2	13	9	593	551	12
2	1	11	382	363	12	3	3	12	0	18	1
5	6	13	848	802	27	2	1	15	799	805	15
3	13	9	0	10	1	3	1	11	0	31	1
4	3	12	134	134	6	0	7	13	894	865	24
3	1	15	155	150	7	1	14	9	76	61	10
4	1	11	0	27	1	5	3	12	976	910	34
1	7	13	0	3	1	4	1	15	196	185	8
0	0	10	907	787	23	5	1	11	0	54	1
6	3	12	0	41	1	2	7	13	719	689	14
5	1	15	102	99	5	2	0	10	239	218	7
6	1	11	288	267	8	0	4	12	438	415	14
3	7	13	0	18	1	1	2	15	561	556	11
4	0	10	264	260	8	7	1	11	132	125	5
1	4	12	97	94	7	4	7	13	328	299	9
2	2	15	34	57	33	6	0	10	248	250	9
1	2	11	634	626	12	2	4	12	590	561	12
5	7	13	62	62	21	3	2	15	143	149	6
1	1	10	534	501	10	2	2	11	56	65	9
3	4	12	12	15	11	1	8	13	155	160	7
4	2	15	0	29	1	2	1	10	128	120	5
3	2	11	882	882	16	4	4	12	757	736	15
2	8	13	23	52	23	5	2	15	776	772	15

Table A3. Observed and calculated structure factors for **1a**.

h	k	l	10Fo	10Fc	10s	h	k	l	10Fo	10Fc	10s
3	1	10	245	243	7	4	2	11	31	35	30
5	4	12	158	152	16	3	8	13	48	39	16
0	3	15	147	153	9	4	1	10	188	178	9
5	2	11	224	211	9	6	4	12	163	132	14
4	8	13	154	148	6	1	3	15	168	179	13
5	1	10	237	232	8	6	2	11	35	53	35
1	5	12	1033	1005	19	5	8	13	0	7	1
2	3	15	90	92	6	6	1	10	65	34	12
7	2	11	538	536	28	2	5	12	105	95	6
0	9	13	0	2	1	3	3	15	40	51	19
7	1	10	76	71	7	0	3	11	854	808	23
3	5	12	291	299	10	1	9	13	95	88	8
4	3	15	189	194	7	0	2	10	195	220	10
1	3	11	12	21	11	4	5	12	159	150	7
2	9	13	506	491	11	5	3	15	0	2	1
1	2	10	141	138	8	2	3	11	2097	2012	37
5	5	12	1360	1255	50	3	9	13	102	96	6
1	4	15	133	141	9	2	2	10	821	778	15
3	3	11	46	34	45	6	5	12	51	54	17
4	9	13	157	150	6	2	4	15	3	46	2
3	2	10	122	107	6	4	3	11	37	43	37
0	6	12	129	83	8	1	10	13	742	739	15
3	4	15	158	166	6	4	3	7	5	57	3
4	2	10	313	296	25	5	3	11	87	88	7
1	6	12	73	92	34	2	10	13	47	48	11
4	4	15	57	46	26	5	4	15	79	75	6
5	1	16	0	19	1	1	9	16	230	241	13
3	7	17	0	11	1	1	8	18	108	118	6
0	5	15	1361	1303	35	0	2	16	580	607	17
2	9	16	102	106	8	1	8	17	391	413	9
1	0	19	65	68	7	1	5	15	161	168	6
1	2	16	116	117	5	0	10	16	407	424	13
2	8	17	52	68	10	3	0	19	398	397	9
2	5	15	687	681	13	2	2	16	713	707	14
1	10	16	9	4	9	0	9	17	764	794	20
0	1	19	561	582	16	3	5	15	42	36	28
3	2	16	70	83	15	1	0	17	694	683	13
1	9	17	15	6	14	1	1	19	190	209	8
4	5	15	395	392	9	4	2	16	99	102	5
3	0	17	163	162	6	0	0	18	684	680	19
2	1	19	199	207	7	5	5	15	0	19	1
5	2	16	0	6	1	0	1	17	1181	1228	31
2	0	18	948	945	20	3	1	19	52	50	12
1	6	15	71	93	19	1	3	16	88	87	6
1	1	17	0	16	1	4	0	18	45	40	15
1	2	19	380	396	9	2	6	15	57	68	9
2	3	16	0	14	1	2	1	17	501	497	10
1	1	18	59	52	12	2	2	19	66	66	7
3	6	15	0	20	1	3	3	16	117	126	5
3	1	17	31	53	30	2	1	18	38	27	26

Table A3. Observed and calculated structure factors for **1a**.

h	k	l	10Fo	10Fc	10s	h	k	l	10Fo	10Fc	10s
3	2	19	814	824	15	4	6	15	48	52	13
4	3	16	50	33	17	4	1	17	512	513	10
3	1	18	187	210	7	0	3	19	376	369	13
0	7	15	233	231	12	5	3	16	0	12	1
1	2	17	43	23	27	4	1	18	98	90	5
1	3	19	110	122	5	1	7	15	0	47	1
0	4	16	297	281	12	2	2	17	0	18	1
0	2	18	188	181	11	2	3	19	563	565	11
2	7	15	15	2	14	1	4	16	133	129	6
3	2	17	349	311	8	1	2	18	132	132	5
3	3	19	0	23	1	3	7	15	41	18	13
2	4	16	187	205	13	4	2	17	15	29	15
2	2	18	333	324	8	1	4	19	47	44	27
4	7	15	218	224	12	3	4	16	62	62	11
0	3	17	361	316	13	3	2	18	110	115	7
2	4	19	85	90	5	1	8	15	195	205	9
4	4	16	336	343	8	1	3	17	27	39	26
4	2	18	351	354	8	3	4	19	101	89	4
2	8	15	0	23	1	5	4	16	28	6	28
2	3	17	197	202	8	1	3	18	141	160	9
0	5	19	85	77	8	3	8	15	470	453	10
1	5	16	361	358	9	3	3	17	15	16	15
2	3	18	26	13	26	1	5	19	49	40	42
4	8	15	0	23	1	2	5	16	27	40	27
4	3	17	272	270	7	3	3	18	831	841	15
2	5	19	516	522	10	0	9	15	667	670	19
3	5	16	919	922	17	1	4	17	197	178	8
4	3	18	30	34	25	1	6	19	16	38	16
1	9	15	22	54	22	4	5	16	0	17	1
2	4	17	51	56	15	0	4	18	298	297	12
0	0	20	713	722	19	2	9	15	555	520	11
0	6	16	803	844	22	3	4	17	286	292	10
1	4	18	118	120	5	2	0	20	1127	1210	20
3	9	15	73	81	7	1	6	16	124	117	5
4	4	17	59	53	15	2	4	18	548	566	11
1	1	20	259	297	7	1	10	15	28	6	28
2	6	16	325	334	8	0	5	17	1436	1458	37
3	4	18	85	84	7	2	1	20	40	42	12
2	10	15	25	6	24	3	6	16	65	62	7
1	5	17	0	17	1	1	5	18	370	374	9
0	2	20	552	616	16	0	11	15	237	260	10
4	6	16	365	381	8	2	5	17	309	294	10
2	5	18	2	30	2	1	2	20	0	32	1
1	11	15	27	22	26	1	7	16	0	19	1
3	5	17	24	22	23	3	5	18	309	319	8
2	2	20	164	160	7	0	0	16	176	194	11
2	7	16	82	88	17	4	5	17	623	643	12
0	6	18	0	22	1	1	3	20	468	504	10
2	0	16	896	899	17	3	7	16	45	56	12
1	6	17	382	412	9	1	6	18	108	115	5

Table A3. Observed and calculated structure factors for **1a**.

h	k	l	10Fo	10Fc	10s	h	k	l	10Fo	10Fc	10s
2	3	20	0	44	1	4	0	16	265	263	8
4	7	16	73	91	6	2	6	17	48	47	9
2	6	18	554	594	11	0	4	20	160	168	10
1	1	16	354	367	9	0	8	16	280	250	12
3	6	17	52	41	22	3	6	18	79	81	7
1	4	20	0	10	1	2	1	16	35	38	34
1	8	16	121	119	5	0	7	17	479	461	15
1	7	18	108	95	5	1	0	21	145	139	6
3	1	16	814	810	15	2	8	16	254	242	8
1	7	17	24	13	24	2	7	18	35	52	33
0	1	21	77	59	6	4	1	16	97	105	6
3	8	16	76	89	6	2	7	17	359	370	8
0	8	18	212	241	10						

Table A4. Observed and calculated structure factors for **1b**.

h	k	l	10Fo	10Fc	10s	h	k	l	10Fo	10Fc	10s
2	0	0	1928	1835	49	4	12	0	20	9	19
4	10	1	157	136	8	4	8	2	529	514	14
0	7	3	2223	2171	56	4	0	0	3267	3203	83
5	12	0	125	129	6	5	10	1	167	163	8
5	8	2	94	83	5	1	7	3	223	214	7
6	0	0	1533	1487	39	1	13	0	319	316	10
6	10	1	112	115	5	6	8	2	360	360	11
2	7	3	480	476	13	8	0	0	43	47	43
2	13	0	58	65	7	0	11	1	221	218	8
7	8	2	256	249	9	3	7	3	264	267	8
1	1	0	1308	1384	33	3	13	0	575	556	16
1	11	1	123	130	6	1	9	2	110	117	5
4	7	3	948	931	24	2	1	0	217	230	6
4	13	0	334	353	10	2	11	1	750	742	20
2	9	2	180	177	7	5	7	3	211	198	9
3	1	0	593	637	15	0	14	0	1183	1150	30
3	11	1	135	131	6	3	9	2	65	75	7
6	7	3	347	326	11	4	1	0	672	667	17
1	14	0	29	12	11	4	11	1	140	138	6
4	9	2	22	6	21	7	7	3	163	174	8
5	1	0	482	465	13	2	14	0	0	26	1
5	11	1	21	22	20	5	9	2	171	177	9
1	8	3	867	863	22	6	1	0	203	196	8
3	14	0	37	45	8	1	12	1	95	98	5
6	9	2	7	36	7	2	8	3	117	112	5
7	1	0	567	567	15	1	15	0	592	620	16
2	12	1	112	118	5	0	10	2	1232	1205	31
3	8	3	801	795	21	8	1	0	28	41	16
2	15	0	68	65	5	3	12	1	587	575	16
1	10	2	181	181	7	4	8	3	411	409	12
0	2	0	1941	1989	49	1	0	1	1786	1924	45
4	12	1	175	158	8	2	10	2	1330	1304	34
5	8	3	1276	1254	33	1	2	0	255	263	6
3	0	1	605	710	16	5	12	1	352	360	10
3	10	2	82	73	6	6	8	3	25	13	25
2	2	0	332	310	9	5	0	1	544	590	16
0	13	1	43	21	9	4	10	2	384	373	12
7	8	3	436	434	12	3	2	0	123	126	5
7	0	1	647	766	19	1	13	1	85	84	5
5	10	2	89	84	5	0	9	3	761	740	20
4	2	0	270	260	8	0	1	1	313	304	8
2	13	1	312	310	10	6	10	2	30	10	29
1	9	3	342	328	10	5	2	0	268	261	9
1	1	1	51	58	2	3	13	1	113	119	5
1	11	2	220	219	8	2	9	3	715	700	19
6	2	0	485	482	14	2	1	1	1399	1390	35
4	13	1	44	60	10	2	11	2	82	83	6
3	9	3	218	213	8	7	2	0	116	108	5
3	1	1	265	268	7	1	14	1	165	156	6
3	11	2	142	131	6	4	9	3	278	270	10

Table A4. Observed and calculated structure factors for **1b**.

h	k	l	10Fo	10Fc	10s	h	k	l	10Fo	10Fc	10s
8	2	0	182	183	8	4	1	1	159	161	6
2	14	1	42	36	7	4	11	2	85	83	5
5	9	3	344	340	11	1	3	0	1457	1460	37
5	1	1	0	17	1	3	14	1	394	398	11
5	11	2	383	390	11	6	9	3	147	153	8
2	3	0	126	136	5	6	1	1	496	482	14
0	15	1	130	145	6	0	12	2	689	682	18
1	10	3	73	60	5	3	3	0	122	163	5
7	1	1	306	305	10	1	15	1	115	106	6
1	12	2	87	79	6	2	10	3	219	210	8
4	3	0	701	713	18	8	1	1	197	201	8
2	15	1	668	673	17	2	12	2	79	58	5
3	10	3	823	805	21	5	3	0	1707	1694	43
1	2	1	271	265	7	0	0	2	3863	3785	98
3	12	2	45	39	7	4	10	3	356	351	11
6	3	0	209	217	8	2	2	1	133	137	4
2	0	2	3098	3010	79	4	12	2	473	470	13
5	10	3	439	421	13	7	3	0	788	758	21
3	2	1	35	61	4	4	0	2	1125	1069	29
5	12	2	0	35	1	6	10	3	93	90	5
8	3	0	105	101	5	4	2	1	44	37	4
6	0	2	34	38	33	1	13	2	67	62	5
0	11	3	182	195	8	0	4	0	4081	3955	104
5	2	1	216	214	8	8	0	2	380	373	12
2	13	2	211	196	9	1	11	3	158	160	8
1	4	0	270	278	7	6	2	1	43	25	9
1	1	2	317	356	8	3	13	2	649	624	17
2	11	3	1123	1118	29	2	4	0	689	697	17
7	2	1	434	416	13	2	1	2	387	394	10
4	13	2	59	67	8	3	11	3	63	63	6
3	4	0	142	143	6	8	2	1	140	139	6
3	1	2	332	302	9	0	14	2	607	621	16
4	11	3	120	121	5	4	4	0	755	772	19
0	3	1	296	312	7	4	1	2	148	143	7
1	14	2	0	2	1	5	11	3	259	268	9
5	4	0	662	643	17	1	3	1	57	62	3
5	1	2	364	366	11	2	14	2	447	439	13
1	12	3	832	829	22	6	4	0	1258	1248	32
2	3	1	875	890	22	6	1	2	318	311	11
3	14	2	130	125	7	2	12	3	86	86	6
7	4	0	18	11	18	3	3	1	224	233	7
7	1	2	220	224	9	1	15	2	167	166	8
3	12	3	489	466	14	8	4	0	310	311	9
4	3	1	77	75	4	8	1	2	88	80	6
2	15	2	36	61	36	4	12	3	162	167	8
1	5	0	1407	1459	35	5	3	1	167	174	8
0	2	2	1121	1200	28	1	0	3	29	49	8
5	12	3	1092	1132	28	2	5	0	150	150	5
6	3	1	102	94	6	1	2	2	63	70	3
3	0	3	59	34	6	0	13	3	551	533	15

Table A4. Observed and calculated structure factors for **1b**.

h	k	l	10Fo	10Fc	10s	h	k	l	10Fo	10Fc	10s
3	5	0	204	212	7	7	3	1	254	238	9
2	2	2	537	569	14	5	0	3	417	389	12
1	13	3	0	40	1	4	5	0	292	289	9
8	3	1	173	174	8	3	2	2	101	102	4
7	0	3	716	691	19	2	13	3	107	102	5
5	5	0	1359	1333	34	1	4	1	481	509	12
4	2	2	345	347	10	0	1	3	984	1002	25
3	13	3	25	24	25	6	5	0	127	120	6
2	4	1	317	318	8	5	2	2	33	39	11
1	1	3	53	53	3	4	13	3	263	265	9
7	5	0	268	259	9	3	4	1	406	378	11
6	2	2	412	419	12	2	1	3	1644	1658	41
1	14	3	54	58	7	0	6	0	390	273	10
4	4	1	186	184	7	7	2	2	190	184	9
3	1	3	39	17	5	2	14	3	80	81	6
1	6	0	575	566	15	5	4	1	342	328	10
8	2	2	155	162	8	4	1	3	539	506	14
3	14	3	293	297	9	2	6	0	563	524	14
6	4	1	179	165	9	1	3	2	77	71	3
5	1	3	674	647	18	0	15	3	568	567	15
3	6	0	29	15	7	7	4	1	208	217	9
2	3	2	360	368	9	6	1	3	621	595	17
1	15	3	191	191	8	4	6	0	267	283	8
8	4	1	320	323	10	3	3	2	887	912	22
7	1	3	309	310	12	2	15	3	731	723	19
5	6	0	584	575	16	0	5	1	215	216	6
4	3	2	139	133	7	8	1	3	155	168	7
0	0	4	1441	1478	36	6	6	0	361	365	11
1	5	1	7	2	7	5	3	2	742	721	19
1	2	3	1630	1626	41	2	0	4	948	971	24
7	6	0	19	33	19	2	5	1	743	795	19
6	3	2	283	274	10	2	2	3	57	65	3
4	0	4	511	522	14	1	7	0	1454	1440	37
3	5	1	0	8	1	7	3	2	887	851	23
3	2	3	32	29	6	6	0	4	766	769	20
2	7	0	362	360	10	4	5	1	381	366	11
8	3	2	52	54	7	4	2	3	264	264	8
8	0	4	399	408	12	3	7	0	163	166	7
5	5	1	0	4	1	0	4	2	1833	1857	46
5	2	3	1552	1538	39	1	1	4	1317	1280	33
4	7	0	157	165	8	6	5	1	292	273	10
1	4	2	191	197	6	6	2	3	123	120	6
2	1	4	159	157	6	5	7	0	1761	1753	45
7	5	1	27	29	27	2	4	2	707	752	18
7	2	3	455	431	13	3	1	4	523	473	14
6	7	0	380	367	11	1	6	1	82	59	4
3	4	2	239	247	7	8	2	3	85	91	6
4	1	4	435	412	12	7	7	0	683	675	18
2	6	1	357	367	10	4	4	2	523	525	14
0	3	3	2401	2370	61	5	1	4	1066	1095	28

Table A4. Observed and calculated structure factors for **1b**.

h	k	l	10Fo	10Fc	10s	h	k	l	10Fo	10Fc	10s
0	8	0	551	496	14	3	6	1	544	544	14
5	4	2	74	76	6	1	3	3	53	47	3
6	1	4	284	320	11	1	8	0	20	6	20
4	6	1	57	44	5	6	4	2	391	397	12
2	3	3	300	316	8	7	1	4	64	54	10
2	8	0	464	440	12	5	6	1	44	37	9
7	4	2	376	359	11	3	3	3	51	46	4
8	1	4	176	189	10	3	8	0	74	73	5
6	6	1	182	172	8	8	4	2	266	265	9
4	3	3	834	807	21	0	2	4	2018	1986	51
4	8	0	333	333	10	7	6	1	202	184	8
1	5	2	210	213	6	5	3	3	334	320	10
1	2	4	278	282	7	5	8	0	290	282	10
0	7	1	265	271	8	2	5	2	77	78	4
6	3	3	457	425	13	2	2	4	746	772	19
6	8	0	278	303	10	1	7	1	18	15	17
3	5	2	662	646	17	7	3	3	195	192	9
3	2	4	318	314	9	7	8	0	92	93	5
2	7	1	958	951	24	4	5	2	128	120	6
8	3	3	0	11	1	4	2	4	172	206	7
1	9	0	902	885	23	3	7	1	245	246	8
5	5	2	0	28	1	1	4	3	139	155	5
5	2	4	49	41	8	2	9	0	35	41	7
4	7	1	65	49	5	6	5	2	165	171	8
2	4	3	14	29	14	6	2	4	622	648	17
3	9	0	615	622	16	5	7	1	38	12	12
7	5	2	100	94	5	3	4	3	554	512	14
7	2	4	34	69	34	4	9	0	143	136	6
6	7	1	131	123	6	0	6	2	641	674	16
4	4	3	206	195	7	8	2	4	225	249	9
5	9	0	508	509	14	7	7	1	213	215	8
1	6	2	16	10	15	5	4	3	241	224	9
1	3	4	135	125	5	6	9	0	206	209	8
1	8	1	0	5	1	2	6	2	49	29	5
6	4	3	169	170	9	2	3	4	278	282	8
0	10	0	3083	3009	78	2	8	1	239	229	8
3	6	2	276	276	8	7	4	3	190	192	9
3	3	4	18	21	17	1	10	0	40	53	7
3	8	1	973	971	25	4	6	2	43	50	7
0	5	3	950	1014	24	4	3	4	235	225	8
2	10	0	218	212	9	4	8	1	108	117	5
5	6	2	61	64	7	1	5	3	134	142	5
5	3	4	182	161	8	3	10	0	310	307	10
5	8	1	345	341	11	6	6	2	387	402	12
2	5	3	269	346	8	6	3	4	345	350	11
4	10	0	1905	1868	48	6	8	1	97	102	6
7	6	2	360	350	11	3	5	3	81	83	4
7	3	4	159	155	8	5	10	0	81	84	5
7	8	1	396	389	11	1	7	2	68	65	4
4	5	3	303	304	9	8	3	4	69	73	5

Table A4. Observed and calculated structure factors for **1b**.

h	k	l	10Fo	10Fc	10s	h	k	l	10Fo	10Fc	10s
6	10	0	538	538	14	0	9	1	55	51	5
2	7	2	89	92	4	5	5	3	213	205	9
0	4	4	361	339	9	1	11	0	313	335	10
1	9	1	103	103	5	3	7	2	1015	1009	26
6	5	3	93	100	6	1	4	4	269	285	7
2	11	0	103	107	5	2	9	1	692	662	18
4	7	2	258	243	9	7	5	3	107	99	5
2	4	4	540	574	14	3	11	0	493	493	14
3	9	1	226	227	8	5	7	2	714	710	19
1	6	3	284	305	8	3	4	4	74	76	4
4	11	0	152	150	8	4	9	1	165	162	8
6	7	2	99	99	6	2	6	3	197	203	7
4	4	4	354	334	10	5	11	0	24	8	24
5	9	1	72	77	7	7	7	2	784	786	20
3	6	3	406	412	11	5	4	4	87	92	6
0	12	0	262	269	9	6	9	1	187	175	8
0	8	2	1030	1010	26	4	6	3	408	403	11
6	4	4	491	482	14	1	12	0	16	9	15
1	10	1	645	644	17	1	8	2	275	283	8
5	6	3	238	238	9	7	4	4	94	92	5
2	12	0	392	408	12	2	10	1	245	240	9
2	8	2	210	225	7	6	6	3	110	111	5
1	5	4	748	776	19	3	12	0	111	113	5
3	10	1	1193	1175	30	3	8	2	44	44	7
7	6	3	200	202	8	2	5	4	60	61	4
3	5	4	43	17	5	7	3	5	111	104	6
1	3	6	666	688	17	3	2	7	1337	1540	34
3	2	8	56	55	5	4	5	4	174	174	7
1	4	5	67	51	3	2	3	6	308	292	9
4	2	7	106	117	6	4	2	8	665	627	18
5	5	4	1298	1284	33	2	4	5	49	47	4
3	3	6	1117	1109	28	5	2	7	257	275	10
5	2	8	184	169	9	6	5	4	108	111	5
3	4	5	190	188	7	4	3	6	269	262	9
6	2	7	204	181	10	6	2	8	253	221	10
7	5	4	152	141	6	4	4	5	160	149	7
5	3	6	312	323	10	7	2	7	760	731	20
7	2	8	131	129	7	0	6	4	1230	1183	31
5	4	5	0	22	1	6	3	6	130	110	7
0	3	7	1252	1302	32	1	3	8	47	41	5
1	6	4	287	295	8	6	4	5	84	81	6
7	3	6	704	752	19	1	3	7	471	444	12
2	3	8	263	264	9	2	6	4	457	474	12
7	4	5	225	230	9	0	4	6	576	555	15
2	3	7	417	398	11	3	3	8	113	108	6
3	6	4	169	168	7	0	5	5	485	578	13
1	4	6	42	35	4	3	3	7	125	119	6
4	3	8	107	124	6	4	6	4	43	25	8
1	5	5	173	177	6	2	4	6	1146	1094	29
4	3	7	1227	1169	31	5	3	8	348	347	12

Table A4. Observed and calculated structure factors for **1b**.

h	k	l	10Fo	10Fc	10s	h	k	l	10Fo	10Fc	10s
5	6	4	107	102	5	2	5	5	303	324	9
3	4	6	181	184	7	5	3	7	157	151	7
6	3	8	91	94	7	6	6	4	261	285	9
3	5	5	105	104	5	4	4	6	120	111	6
6	3	7	364	405	12	7	3	8	102	110	7
7	6	4	54	52	6	4	5	5	549	553	15
5	4	6	254	242	9	7	3	7	19	5	19
0	4	8	968	911	25	1	7	4	87	84	4
5	5	5	133	131	7	6	4	6	229	219	9
1	4	7	196	199	6	1	4	8	340	339	10
2	7	4	66	59	4	6	5	5	417	405	12
7	4	6	385	390	11	2	4	7	79	76	4
2	4	8	587	528	15	3	7	4	195	205	8
7	5	5	153	154	8	1	5	6	1011	954	26
3	4	7	549	531	15	3	4	8	58	54	6
4	7	4	163	164	8	1	6	5	686	636	17
2	5	6	291	291	8	4	4	7	102	95	5
4	4	8	285	282	10	5	7	4	71	22	7
2	6	5	139	144	6	3	5	6	974	980	25
5	4	7	513	523	14	5	4	8	258	236	10
6	7	4	23	34	22	3	6	5	673	676	17
4	5	6	101	104	5	6	4	7	311	294	11
6	4	8	23	71	23	7	7	4	194	191	8
4	6	5	247	233	8	5	5	6	1336	1313	34
7	4	7	316	365	11	7	4	8	353	324	12
0	8	4	845	859	22	5	6	5	542	536	15
6	5	6	89	86	6	0	5	7	185	161	6
1	5	8	855	814	22	1	8	4	271	261	8
6	6	5	14	8	14	7	5	6	865	870	22
1	5	7	251	242	8	2	5	8	52	53	5
2	8	4	612	608	16	7	6	5	112	97	6
0	6	6	61	50	4	2	5	7	462	476	12
3	5	8	617	597	16	3	8	4	204	203	8
0	7	5	1488	1447	38	1	6	6	115	112	6
3	5	7	67	56	5	4	5	8	31	33	17
4	8	4	651	654	17	1	7	5	77	81	4
2	6	6	222	226	8	4	5	7	196	192	8
5	5	8	1294	1245	33	5	8	4	60	66	9
2	7	5	78	77	4	3	6	6	229	235	8
5	5	7	25	45	24	6	5	8	45	44	12
6	8	4	153	154	8	3	7	5	0	1	1
4	6	6	222	227	9	6	5	7	226	238	9
7	5	8	303	342	10	7	8	4	22	7	21
4	7	5	748	742	20	5	6	6	359	350	11
7	5	7	51	60	8	0	6	8	335	326	10
1	9	4	710	706	18	5	7	5	231	231	9
6	6	6	219	210	9	1	6	7	81	72	4
1	6	8	218	219	8	2	9	4	37	42	9
6	7	5	467	452	13	7	6	6	393	393	11
2	6	7	150	155	7	2	6	8	0	17	1

Table A4. Observed and calculated structure factors for **1b**.

h	k	l	10Fo	10Fc	10s	h	k	l	10Fo	10Fc	10s
3	9	4	174	185	8	7	7	5	14	40	13
1	7	6	499	498	13	3	6	7	885	869	23
3	6	8	82	84	5	4	9	4	52	44	7
1	8	5	610	625	16	2	7	6	249	244	8
4	6	7	170	157	8	4	6	8	279	284	10
5	9	4	908	906	23	2	8	5	70	69	5
3	7	6	1115	1104	28	5	6	7	396	398	12
5	6	8	258	251	10	6	9	4	0	12	1
3	8	5	133	126	6	4	7	6	0	20	1
6	6	7	275	258	10	6	6	8	308	325	10
0	10	4	296	299	9	4	8	5	3	22	3
5	7	6	188	179	9	7	6	7	416	448	12
7	6	8	247	326	9	1	10	4	0	10	1
5	8	5	1028	1013	26	6	7	6	54	53	8
0	7	7	1238	1227	31	1	7	8	98	98	5
2	10	4	639	634	17	6	8	5	159	165	6
7	7	6	647	691	17	1	7	7	448	443	12
2	7	8	0	5	1	3	10	4	68	70	7
0	9	5	924	897	24	0	8	6	1021	995	26
2	7	7	425	400	12	3	7	8	239	246	9
4	10	4	633	633	17	1	9	5	33	26	10
1	8	6	111	106	5	3	7	7	117	125	6
4	7	8	34	17	15	5	10	4	90	93	5
2	9	5	474	463	13	2	8	6	1925	1898	49
4	7	7	1133	1105	29	5	7	8	455	423	13
6	10	4	97	91	5	3	9	5	50	60	8
3	8	6	22	24	21	5	7	7	25	34	24
6	7	8	0	4	1	1	11	4	576	575	16
4	9	5	613	607	17	4	8	6	56	61	8
6	7	7	423	411	12	0	8	8	1582	1545	40
2	11	4	64	76	7	5	9	5	90	89	6
5	8	6	322	308	10	1	8	7	526	518	14
1	8	8	472	466	13	3	11	4	88	93	5
6	9	5	63	57	7	6	8	6	446	445	13
2	8	7	21	13	20	2	8	8	670	644	18
4	11	4	49	48	7	1	10	5	505	496	14
1	9	6	636	631	17	3	8	7	949	908	24
3	8	8	140	132	6	5	11	4	606	606	16
2	10	5	33	42	33	2	9	6	223	222	9
4	8	7	39	27	11	4	8	8	654	631	18
0	12	4	501	467	14	3	10	5	536	558	15
3	9	6	391	373	12	5	8	7	191	198	8
5	8	8	212	201	9	1	12	4	27	5	27
4	10	5	95	82	5	4	9	6	178	181	9
6	8	7	133	147	7	6	8	8	308	321	10
2	12	4	518	496	14	5	10	5	514	503	14
5	9	6	834	835	22	0	9	7	463	480	13
1	9	8	228	209	9	3	12	4	121	110	6
6	10	5	80	76	5	6	9	6	0	37	1
1	9	7	473	462	13	2	9	8	189	178	8

Table A4. Observed and calculated structure factors for **1b**.

h	k	l	10Fo	10Fc	10s	h	k	l	10Fo	10Fc	10s
4	12	4	331	338	10	0	11	5	937	953	24
0	10	6	824	826	21	2	9	7	402	386	12
3	9	8	478	475	14	5	12	4	157	153	8
1	11	5	329	313	10	1	10	6	353	342	11
3	9	7	272	274	10	4	9	8	274	270	10
1	13	4	184	168	8	2	11	5	304	292	10
2	10	6	1363	1332	35	4	9	7	224	201	9
5	9	8	549	534	15	2	13	4	0	4	1
3	11	5	125	129	6	3	10	6	234	237	9
5	9	7	178	177	8	6	9	8	59	63	5
3	13	4	0	9	1	4	11	5	566	564	15
4	10	6	144	155	6	6	9	7	0	37	1
0	10	8	1290	1243	33	4	13	4	46	56	7
5	11	5	154	154	8	5	10	6	0	4	1
1	10	7	445	431	13	1	10	8	331	340	11
0	14	4	147	148	8	1	12	5	395	379	12
6	10	6	298	321	9	2	10	7	29	5	28
2	10	8	991	972	26	1	14	4	0	27	1
2	12	5	117	122	5	1	11	6	34	58	34
3	10	7	233	244	9	3	10	8	134	130	6
2	14	4	414	414	12	3	12	5	334	327	11
2	11	6	218	214	9	4	10	7	0	0	1
4	10	8	419	394	12	3	14	4	26	34	25
4	12	5	91	108	5	3	11	6	303	292	10
5	10	7	644	662	17	5	10	8	25	39	25
1	15	4	404	413	12	5	12	5	806	828	21
4	11	6	168	166	7	0	11	7	325	318	10
1	11	8	124	122	6	2	15	4	108	116	4
0	13	5	365	371	11	5	11	6	312	295	10
1	11	7	445	435	13	2	11	8	166	154	8
1	0	5	1418	1372	36	1	13	5	59	57	6
0	12	6	710	691	19	2	11	7	54	43	7
3	11	8	205	186	9	3	0	5	218	200	7
2	13	5	179	197	9	1	12	6	255	234	9
3	11	7	193	183	9	4	11	8	207	205	9
5	0	5	1101	1074	28	3	13	5	52	51	7
2	12	6	1122	1071	29	4	11	7	302	307	10
5	11	8	262	277	9	7	0	5	277	288	10
4	13	5	158	155	8	3	12	6	216	207	8
5	11	7	43	57	10	0	12	8	1103	1052	28
0	1	5	1621	1670	41	1	14	5	18	7	18
4	12	6	69	53	5	1	12	7	440	429	13
1	12	8	168	181	9	1	1	5	312	335	9
2	14	5	49	48	6	1	13	6	596	586	16
2	12	7	139	141	6	2	12	8	355	345	11
2	1	5	473	525	12	3	14	5	134	140	6
2	13	6	213	211	9	3	12	7	750	743	20
3	12	8	0	14	1	3	1	5	150	170	8
0	15	5	796	813	21	3	13	6	575	579	15
4	12	7	105	105	5	4	12	8	359	359	11

Table A4. Observed and calculated structure factors for **1b**.

h	k	l	10Fo	10Fc	10s	h	k	l	10Fo	10Fc	10s
4	1	5	960	1054	25	1	15	5	209	225	8
4	13	6	203	216	8	0	13	7	928	901	24
1	13	8	190	184	9	5	1	5	304	329	11
0	0	6	792	769	20	0	14	6	329	342	10
1	13	7	102	102	5	2	13	8	227	229	9
6	1	5	102	114	8	2	0	6	1369	1376	34
1	14	6	136	140	6	2	13	7	0	9	1
3	13	8	42	54	7	7	1	5	309	287	11
4	0	6	351	346	10	2	14	6	12	31	12
3	13	7	35	51	34	0	14	8	311	323	10
8	1	5	71	85	6	6	0	6	543	545	15
3	14	6	242	238	8	1	14	7	81	87	6
1	14	8	58	62	7	1	2	5	1275	1268	32
1	1	6	483	500	13	1	15	6	70	71	5
2	14	7	99	103	5	2	14	8	246	250	8
2	2	5	194	196	6	2	1	6	402	387	11
1	0	7	811	814	20	0	0	8	507	563	13
1	0	9	1407	1347	35	3	2	5	1468	1430	37
3	1	6	508	500	14	3	0	7	149	139	6
2	0	8	1045	1020	26	3	0	9	1436	1438	36
4	2	5	51	47	7	4	1	6	187	182	8
5	0	7	1023	1022	26	4	0	8	554	519	15
5	0	9	1652	1625	42	5	2	5	1723	1663	44
5	1	6	841	824	22	7	0	7	170	158	8
6	0	8	141	159	6	7	0	9	918	887	24
6	2	5	96	78	6	6	1	6	201	203	10
0	1	7	313	328	9	1	1	8	336	329	9
0	1	9	385	362	10	7	2	5	256	245	10
7	1	6	360	352	11	1	1	7	25	12	24
2	1	8	278	273	8	1	1	9	91	94	4
8	2	5	9	29	9	0	2	6	464	485	12
2	1	7	277	234	8	3	1	8	558	551	15
2	1	9	125	104	5	0	3	5	1420	1417	36
1	2	6	211	207	7	3	1	7	171	168	7
4	1	8	268	261	9	3	1	9	176	168	7
1	3	5	0	10	1	2	2	6	584	662	15
4	1	7	349	338	10	5	1	8	632	623	17
4	1	9	79	49	6	2	3	5	66	38	3
3	2	6	160	157	7	5	1	7	301	301	10
6	1	8	68	68	7	5	1	9	479	471	14
3	3	5	75	65	4	4	2	6	88	71	5
6	1	7	29	44	24	7	1	8	234	231	9
6	1	9	178	169	9	4	3	5	548	542	15
5	2	6	296	297	11	7	1	7	0	6	1
0	2	8	111	171	5	7	1	9	247	242	9
5	3	5	360	344	11	6	2	6	241	287	11
1	2	7	555	606	14	1	2	8	178	182	7
1	2	9	838	803	21	6	3	5	536	525	15
7	2	6	222	220	10	2	2	7	95	108	4
2	2	8	459	389	12	2	2	9	37	31	8

Table A4. Observed and calculated structure factors for **1b**.

h	k	l	10Fo	10Fc	10s	h	k	l	10Fo	10Fc	10s
3	2	9	154	152	7	7	2	10	18	15	17
2	4	11	311	307	10	4	6	12	167	152	7
1	11	13	278	274	10	4	2	9	66	65	6
1	3	10	282	284	9	3	4	11	764	740	20
5	6	12	489	475	14	2	11	13	625	599	17
5	2	9	692	679	18	2	3	10	232	215	8
4	4	11	0	7	1	6	6	12	311	314	10
3	11	13	242	261	9	6	2	9	91	80	6
3	3	10	650	649	17	5	4	11	747	714	20
1	7	12	693	746	19	1	12	13	140	147	6
7	2	9	34	60	33	4	3	10	447	436	13
6	4	11	254	244	10	2	7	12	221	215	11
0	0	14	907	897	23	0	3	9	1630	1978	41
5	3	10	134	119	7	0	5	11	355	383	11
3	7	12	139	128	7	2	0	14	1380	1386	35
1	3	9	199	213	8	6	3	10	0	11	1
1	5	11	57	60	8	4	7	12	236	220	10
4	0	14	166	182	8	2	3	9	683	748	18
7	3	10	263	247	9	2	5	11	376	389	12
5	7	12	747	723	20	6	0	14	234	245	8
3	3	9	197	188	8	0	4	10	411	459	12
3	5	11	50	51	9	0	8	12	928	1076	25
1	1	14	172	176	8	4	3	9	1085	1068	28
1	4	10	234	264	9	4	5	11	546	525	16
1	8	12	202	241	10	2	1	14	543	543	15
5	3	9	353	338	12	2	4	10	461	499	13
5	5	11	145	146	7	2	8	12	346	378	12
3	1	14	461	451	13	6	3	9	126	130	6
3	4	10	323	329	11	6	5	11	0	24	1
3	8	12	69	58	8	4	1	14	269	281	9
7	3	9	50	44	8	4	4	10	794	758	21
1	6	11	239	249	10	4	8	12	440	419	13
5	1	14	119	120	6	1	4	9	450	410	12
5	4	10	137	125	7	2	6	11	295	346	11
5	8	12	322	321	10	6	1	14	293	310	9
2	4	9	169	156	8	6	4	10	28	24	28
3	6	11	263	264	10	1	9	12	309	357	12
0	2	14	879	876	23	3	4	9	1303	1340	33
7	4	10	22	2	21	4	6	11	101	105	8
2	9	12	279	305	11	1	2	14	64	63	5
4	4	9	44	56	13	1	5	10	65	61	6
5	6	11	504	451	15	3	9	12	262	258	10
2	2	14	1295	1265	33	5	4	9	793	834	21
2	5	10	89	91	6	6	6	11	315	293	10
4	9	12	190	196	9	3	2	14	162	162	8
6	4	9	324	293	12	3	5	10	314	339	11
0	7	11	950	915	25	0	10	12	1143	1296	30
4	2	14	41	17	7	7	4	9	663	614	18
4	5	10	31	35	31	1	7	11	57	48	9
1	10	12	203	214	11	5	2	14	0	24	1

Table A4. Observed and calculated structure factors for **1b**.

h	k	l	10Fo	10Fc	10s	h	k	l	10Fo	10Fc	10s
0	5	9	0	10	1	5	5	10	0	24	1
2	7	11	1998	2027	51	2	10	12	183	175	10
6	2	14	112	108	5	1	5	9	142	141	7
6	5	10	33	44	32	3	7	11	196	211	11
3	10	12	181	174	9	1	3	14	98	89	5
2	5	9	273	264	9	0	6	10	567	530	15
4	7	11	0	38	1	4	10	12	857	825	22
2	3	14	364	367	11	3	5	9	70	72	6
1	6	10	228	214	9	5	7	11	190	186	9
1	11	12	142	145	7	3	3	14	382	368	11
4	5	9	191	194	10	2	6	10	396	360	12
6	7	11	316	309	10	2	11	12	157	159	7
4	3	14	297	304	10	5	5	9	81	90	8
3	6	10	342	331	11	1	8	11	568	545	16
3	11	12	35	7	34	5	3	14	329	311	10
6	5	9	0	6	1	4	6	10	334	346	12
2	8	11	262	252	10	0	12	12	691	746	19
6	3	14	166	176	7	7	5	9	48	39	9
5	6	10	26	12	25	3	8	11	477	514	14
1	12	12	216	213	9	0	4	14	218	225	9
1	6	9	477	466	13	6	6	10	242	221	10
4	8	11	138	139	6	2	12	12	74	77	6
1	4	14	132	122	6	2	6	9	148	154	8
1	7	10	399	387	12	5	8	11	375	365	12
1	0	13	658	663	17	2	4	14	435	439	13
3	6	9	682	632	18	2	7	10	119	111	6
0	9	11	55	32	8	3	0	13	285	279	10
3	4	14	82	77	6	4	6	9	63	59	7
3	7	10	588	567	16	1	9	11	173	152	7
5	0	13	885	850	23	4	4	14	331	337	10
5	6	9	120	111	6	4	7	10	131	124	6
2	9	11	232	234	10	0	1	13	163	139	7
5	4	14	69	63	6	6	6	9	162	206	7
5	7	10	170	209	8	3	9	11	156	173	8
1	1	13	672	675	18	1	5	14	600	589	16
0	7	9	2184	2120	55	6	7	10	85	89	7
4	9	11	140	156	7	2	1	13	687	681	18
2	5	14	299	303	10	1	7	9	404	394	12
0	8	10	484	461	14	5	9	11	220	213	9
3	1	13	618	619	17	3	5	14	1273	1219	33
2	7	9	733	729	19	1	8	10	392	383	12
1	10	11	183	182	9	4	1	13	179	170	8
4	5	14	243	246	9	3	7	9	194	186	8
2	8	10	702	678	19	2	10	11	164	166	8
5	1	13	28	40	28	5	5	14	215	204	8
4	7	9	1180	1168	30	3	8	10	278	275	10
3	10	11	1065	1134	28	6	1	13	173	149	8
0	6	14	926	919	24	5	7	9	156	148	7
4	8	10	564	560	16	4	10	11	105	104	6
1	2	13	36	17	7	1	6	14	119	114	6

Table A4. Observed and calculated structure factors for **1b**.

h	k	l	10Fo	10Fc	10s	h	k	l	10Fo	10Fc	10s
6	7	9	104	128	6	5	8	10	44	73	16
0	11	11	339	322	11	2	2	13	110	110	5
2	6	14	215	224	9	1	8	9	122	102	6
6	8	10	341	303	11	1	11	11	325	312	11
3	2	13	304	286	10	3	6	14	156	151	8
2	8	9	0	5	1	1	9	10	2	34	2
2	11	11	143	90	7	4	2	13	373	372	11
4	6	14	372	374	11	3	8	9	486	480	14
2	9	10	140	136	7	3	11	11	47	60	10
5	2	13	238	240	9	5	6	14	116	102	6
4	8	9	53	62	9	3	9	10	289	262	10
4	11	11	29	20	15	6	2	13	75	85	5
1	7	14	93	84	6	5	8	9	72	71	7
4	9	10	298	295	11	1	12	11	324	350	11
0	3	13	890	871	23	2	7	14	104	103	5
6	8	9	16	36	16	5	9	10	0	33	1
2	12	11	29	3	29	1	3	13	303	297	10
3	7	14	360	351	11	0	9	9	48	49	7
0	10	10	203	217	9	3	12	11	468	486	13
2	3	13	539	540	15	4	7	14	112	114	5
1	9	9	390	379	12	1	10	10	94	82	6
0	13	11	203	253	10	3	3	13	233	241	9
5	7	14	329	338	10	2	9	9	120	108	5
2	10	10	0	20	1	1	13	11	201	230	9
4	3	13	208	196	8	0	8	14	440	430	13
3	9	9	376	365	12	3	10	10	54	51	9
0	0	12	1989	1984	50	5	3	13	54	43	8
1	8	14	136	141	6	4	9	9	38	22	11
4	10	10	30	65	30	2	0	12	350	311	10
6	3	13	181	173	8	2	8	14	626	594	17
5	9	9	291	297	10	5	10	10	14	4	14
4	0	12	1597	1567	41	1	4	13	484	480	13
3	8	14	79	85	6	1	10	9	297	292	10
1	11	10	190	173	9	6	0	12	292	275	10
2	4	13	178	183	9	4	8	14	175	174	7
2	10	9	64	68	7	2	11	10	37	21	10
1	1	12	267	265	9	3	4	13	223	218	9
1	9	14	228	234	9	3	10	9	641	589	17
3	11	10	70	59	6	2	1	12	85	78	5
4	4	13	468	454	13	2	9	14	0	31	1
4	10	9	120	124	6	4	11	10	210	238	9
3	1	12	246	250	9	5	4	13	615	610	17
3	9	14	511	493	14	5	10	9	693	740	18
0	12	10	346	324	11	4	1	12	378	396	11
6	4	13	181	177	8	4	9	14	137	134	7
0	11	9	170	144	8	1	12	10	160	165	9
5	1	12	375	351	11	0	5	13	230	231	9
0	10	14	168	149	8	1	11	9	185	175	9
2	12	10	283	290	10	6	1	12	267	284	9
1	5	13	219	218	9	1	10	14	170	163	9

Table A4. Observed and calculated structure factors for **1b**.

h	k	l	10Fo	10Fc	10s	h	k	l	10Fo	10Fc	10s
2	11	9	132	119	6	3	12	10	114	116	6
0	2	12	1355	1341	34	2	5	13	1306	1264	33
2	10	14	661	654	18	3	11	9	108	104	5
1	13	10	310	309	10	1	2	12	357	355	10
3	5	13	158	161	7	3	10	14	88	80	4
4	11	9	106	111	5	2	13	10	63	63	7
2	2	12	256	272	9	4	5	13	288	264	10
1	11	14	92	20	5	1	12	9	141	134	6
1	0	11	323	330	9	3	2	12	208	196	8
5	5	13	0	17	1	2	11	14	132	134	7
2	12	9	0	29	1	3	0	11	1829	1807	46
4	2	12	702	673	19	6	5	13	569	576	15
1	0	15	31	20	30	3	12	9	207	218	9
5	0	11	798	782	21	5	2	12	364	378	11
1	6	13	678	666	18	3	0	15	150	168	7
4	12	9	105	109	6	7	0	11	1124	1147	29
6	2	12	185	176	8	2	6	13	261	247	10
5	0	15	10	11	9	0	13	9	855	839	22
0	1	11	147	157	6	1	3	12	820	795	21
3	6	13	153	160	7	0	1	15	682	693	18
1	13	9	0	2	1	1	1	11	91	98	4
2	3	12	108	100	5	4	6	13	548	540	15
1	1	15	893	906	23	2	13	9	585	542	16
2	1	11	304	289	9	3	3	12	42	24	9
5	6	13	660	661	18	2	1	15	851	828	22
3	13	9	24	34	24	3	1	11	92	88	5
4	3	12	321	326	10	0	7	13	863	822	23
3	1	15	378	385	11	1	14	9	61	63	6
4	1	11	63	63	6	5	3	12	817	793	21
1	7	13	28	12	28	4	1	15	149	148	6
0	0	10	519	481	14	5	1	11	150	143	8
6	3	12	145	128	7	2	7	13	617	589	17
5	1	15	230	237	9	2	0	10	163	140	7
6	1	11	215	214	9	0	4	12	479	463	13
3	7	13	0	6	1	1	2	15	382	380	11
4	0	10	330	347	10	7	1	11	309	320	9
1	4	12	261	260	9	4	7	13	175	169	8
2	2	15	145	142	6	6	0	10	218	216	9
1	2	11	558	564	15	2	4	12	612	593	16
5	7	13	114	112	6	3	2	15	93	86	5
1	1	10	347	318	10	2	2	11	182	175	7
3	4	12	47	36	7	1	8	13	142	138	7
4	2	15	71	72	5	4	3	7	0	209	8
2	1	10	331	321	10	3	2	11	889	884	23
4	4	12	603	602	16	2	8	13	128	115	6
5	2	15	608	610	16	3	1	10	229	232	8
4	2	11	88	80	6	5	4	12	375	372	12
3	8	13	172	154	7	0	3	15	145	142	6
4	1	10	480	465	13	5	2	11	162	174	8
6	4	12	199	182	8	4	8	13	391	372	12

Table A4. Observed and calculated structure factors for **1b**.

h	k	l	10Fo	10Fc	10s	h	k	l	10Fo	10Fc	10s
1	3	15	423	439	12	5	1	10	171	191	7
6	2	11	133	135	6	1	5	12	1001	938	26
5	8	13	110	115	5	2	3	15	90	97	5
6	1	10	152	145	8	7	2	11	428	450	12
2	5	12	277	256	10	0	9	13	55	63	9
3	3	15	138	140	7	7	1	10	85	76	5
0	3	11	842	829	22	3	5	12	351	352	11
1	9	13	254	247	10	4	3	15	195	191	8
0	2	10	295	302	9	1	3	11	58	53	6
4	5	12	373	359	12	2	9	13	474	429	14
5	3	15	0	33	1	1	2	10	392	388	11
2	3	11	1934	1906	49	5	5	12	1091	1058	28
3	9	13	303	292	10	1	4	15	82	75	5
2	2	10	708	691	18	3	3	11	71	78	6
6	5	12	128	125	6	4	9	13	114	104	5
2	4	15	112	110	5	3	2	10	297	293	9
4	3	11	0	14	1	0	6	12	151	134	7
1	10	13	736	722	20	3	4	15	212	194	9
4	2	10	216	200	9	5	3	11	203	204	9
1	6	12	251	251	10	2	10	13	130	120	7
4	4	15	150	140	8	5	2	10	143	143	7
6	3	11	313	302	10	2	6	12	481	467	14
3	10	13	70	67	6	5	4	15	133	134	5
6	2	10	480	475	14	1	4	11	249	225	9
3	6	12	108	102	6	0	11	13	145	149	7
0	5	15	1287	1254	33	1	5	15	387	404	12
0	2	16	565	593	15	2	9	16	251	263	8
2	7	17	256	274	9	2	7	18	97	112	5
2	5	15	667	671	18	1	2	16	332	334	11
0	10	16	394	404	11	3	7	17	23	6	22
0	8	18	194	196	7	3	5	15	85	80	5
2	2	16	539	538	15	1	10	16	21	22	20
1	8	17	304	314	10	1	0	19	24	18	24
4	5	15	407	398	12	3	2	16	231	223	9
1	0	17	566	544	15	2	8	17	142	155	7
3	0	19	341	337	10	5	5	15	63	61	5
4	2	16	43	30	7	3	0	17	188	175	8
0	9	17	696	715	18	0	1	19	487	512	14
1	6	15	59	53	7	5	2	16	0	40	1
0	1	17	1044	1045	27	1	9	17	35	13	7
1	1	19	530	553	14	2	6	15	167	172	9
1	3	16	81	84	5	1	1	17	0	8	1
0	0	18	428	357	12	2	1	19	137	141	6
3	6	15	60	63	6	2	3	16	24	47	24
2	1	17	329	337	10	2	0	18	940	910	24
3	1	19	172	165	7	4	6	15	148	148	7
3	3	16	61	61	6	3	1	17	134	125	6
4	0	18	23	2	23	1	2	19	423	434	12
0	7	15	245	249	9	4	3	16	117	122	6
4	1	17	504	501	14	1	1	18	85	92	6

Table A4. Observed and calculated structure factors for **1b**.

h	k	l	10Fo	10Fc	10s	h	k	l	10Fo	10Fc	10s
2	2	19	163	168	8	1	7	15	91	94	5
5	3	16	73	73	4	1	2	17	148	121	8
2	1	18	95	89	5	3	2	19	720	734	19
2	7	15	25	39	25	0	4	16	324	317	10
2	2	17	4	44	4	3	1	18	214	227	8
0	3	19	436	457	12	3	7	15	80	70	6
1	4	16	383	365	12	3	2	17	312	283	10
4	1	18	259	266	9	1	3	19	295	314	9
4	7	15	159	169	7	2	4	16	174	149	8
4	2	17	81	80	5	0	2	18	218	227	9
2	3	19	452	453	13	1	8	15	236	227	9
3	4	16	191	185	8	0	3	17	261	235	9
1	2	18	344	335	11	3	3	19	63	71	5
2	8	15	66	58	5	4	4	16	354	358	11
1	3	17	123	109	6	2	2	18	259	265	9
1	4	19	23	4	23	3	8	15	433	413	12
1	5	16	297	302	10	2	3	17	147	147	6
3	2	18	309	311	10	2	4	19	248	244	8
4	8	15	49	51	6	2	5	16	91	88	5
3	3	17	39	36	8	4	2	18	269	285	9
0	5	19	18	19	18	0	9	15	620	617	17
3	5	16	903	898	23	4	3	17	211	217	8
1	3	18	190	185	9	1	5	19	99	104	5
1	9	15	159	163	8	4	5	16	29	39	15
1	4	17	235	223	9	2	3	18	67	69	6
2	5	19	438	439	12	2	9	15	463	457	13
0	6	16	683	700	18	2	4	17	131	133	6
3	3	18	754	752	20	1	6	19	0	13	1
3	9	15	212	210	8	1	6	16	358	351	11
3	4	17	249	262	9	4	3	18	124	111	6
0	0	20	595	615	16	1	10	15	0	19	1
2	6	16	326	341	10	4	4	17	152	144	8
0	4	18	172	178	8	2	0	20	946	965	24
2	10	15	0	16	1	3	6	16	185	181	8
0	5	17	1317	1299	34	1	4	18	318	311	10
1	1	20	249	250	8	0	11	15	222	232	8
4	6	16	338	367	10	1	5	17	13	24	12
2	4	18	463	456	13	2	1	20	94	103	5
0	0	16	250	215	9	1	7	16	40	44	10
2	5	17	181	179	8	3	4	18	215	222	8
0	2	20	406	416	11	2	0	16	782	779	20
2	7	16	219	219	8	3	5	17	41	59	10
1	5	18	406	411	12	1	2	20	60	64	5
4	0	16	462	443	13	3	7	16	124	124	6
4	5	17	563	590	15	2	5	18	28	47	27
2	2	20	222	224	8	1	1	16	359	342	11
0	8	16	198	177	8	1	6	17	360	382	11
3	5	18	264	271	9	1	3	20	427	448	12
2	1	16	134	124	6	1	8	16	347	340	11
2	6	17	118	112	6	0	6	18	108	104	6

Table A4. Observed and calculated structure factors for **1b**.

h	k	l	10Fo	10Fc	10s	h	k	l	10Fo	10Fc	10s
2	3	20	89	100	5	3	1	16	712	698	19
2	8	16	191	178	8	3	6	17	149	153	8
1	6	18	301	300	10	0	4	20	125	129	5
4	1	16	287	279	9	3	8	16	208	222	8
0	7	17	379	365	11	2	6	18	542	559	15
1	4	20	22	38	15	5	1	16	20	16	19
1	9	16	179	186	8	1	7	17	0	31	1
1	7	18	159	150	7						